Development of SERS substrates for detecting differentiation in mesenchymal stromal cells

Adrianna Milewska

Faculty of Industrial Engineering, Mechanical Engineering and Computer Science
University of Iceland
2021

Development of SERS substrates for detecting differentiation in mesenchymal stromal cells

Adrianna Milewska

Dissertation submitted in partial fulfillment of a
Philosophiae Doctor degree in Bioengineering

PhD Committee
Kristján Leósson
Ólafur E. Sigurjónsson
Unnar B. Arnalds
Sigurður Brynjólfsson

Opponents
Laura Fabris
Mads Bergholt

Faculty of Industrial Engineering, Mechanical Engineering and Computer Science
School of Engineering and Natural Sciences
University of Iceland
Reykjavik, August 2021

Development of SERS substrates for detecting differentiation in mesenchymal stromal cells

Dissertation submitted in partial fulfillment of a *Philosophiae Doctor* degree in Bioengineering

Faculty of Industrial Engineering, Mechanical Engineering and Computer Science
School of Engineering and Natural Sciences
University of Iceland
Dunhagi 5
107, Reykjavik
Iceland

Telephone: +354 525 4000

ISBN 978-9935-9614-0-2

Bibliographic information:
Adrianna Milewska, 2021, *Development of SERS substrates for detecting differentiation in mesenchymal stromal cells*, PhD dissertation, Faculty of Industrial Engineering, Mechanical Engineering and Computer Science, University of Iceland

Printing: Háskólaprent ehf.
Reykjavik, Iceland, August 2021

Abstract

Identification of primary cells, such as mesenchymal stromal cells, at the molecular level is vital for better understanding of their differentiation pathways. Surface-enhanced Raman scattering has a potential to become a non-invasive screening method for characterization of biomolecules, including their dynamic changes in conformation, distribution, and interactions. However, the lack of appropriate SERS substrates, cell monitoring protocols and difficulties in translation of the SERS spectral information into widely understandable data are a reason why SERS is not yet extensively used. This thesis focuses on the development of a surface-enhanced Raman scattering platform for continuous screening of cells and their processes. This platform was used specifically for studying osteogenic differentiation of mesenchymal stromal cells (MSCs) determined from changes occurring on the cell membranes during differentiation. SERS substrates were fabricated on glass supports by repeated thin gold films deposition and thermal annealing, which resulted in wide diversity of gold nanoisland sizes and homogeneous distribution of “hot spots”. In order to ensure high and uniform signal enhancement across large areas, numerical simulations and experimental assessments of enhancement factors were performed, indicating the enhancement factors of the order of 10^6 are uniformly distributed across the substrate’s area. Moreover, the SERS substrate’s biocompatibility was confirmed by viability assays and immunofluorescence staining, which clearly verified that the presence of the SERS substrates does not hamper cell propagation. The applicability for long-term cell proliferation and SERS screening was demonstrated by culturing MSCs and recording spectra of cellular membrane at different timepoints during differentiation, simultaneously confirming the osteogenic phenotype with standard methods. The results indicate that SERS culturing platform can be used to investigate the composition of cell membranes during osteogenic differentiation, combining imaging of cells with spectroscopic detection of molecular species and chemical events occurring on the cellular membrane adjacent to the surface of the SERS substrate, without disturbing the cells. In addition, SERS substrates were used for live-cell imaging of a fibroblast cell line, further indicating that the SERS substrates and optical excitation conditions do not adversely affect live cells, paving a way towards continuous label-free screening of osteogenic differentiation of live mesenchymal stromal cells.

Útdráttur

Til að skilja betur þá sameindafræðilegu ferla sem stýra sérhæfingu mannafruma, eins og t.d. mesenkímal bandvefsfruma, er mikilvægt að búa yfir viðeigandi greiningartækni. Meðal mögulegra leiða til að rannsaka slíkar frumur án inngrips er yfirborðsmögnuð Raman ljósdreifing (SERS) en með henni má greina lífrænar sameindir, staðsetningu þeirra, uppbyggingu og víxlverkun þeirra á milli. Þessi aðferð hefur þó náð takmarkaðri útbreiðslu þar sem skortur er á viðeigandi yfirborðum og samhæfðum mæliaðferðum, auk þess hve erfitt er að þýða litrófsupplýsingarnar yfir í nýtanleg gögn. Þessi ritgerð fjallar um þróun yfirborða sem gefa möguleika á að framkvæma samfelldar mælingar á frumum og þeim sameindalífræðilegu ferlum sem eiga sér stað innan þeirra. Aðferðafræðin var nýtt sérstaklega til að rannsaka beinsérhæfingu mesenkímal bandvefsfruma með því að fylgjast með breytingum sem áttu sér stað í frumuhimnu við sérhæfinguna. SERS-virk yfirborð voru útbúin á glerþynnum með endurtekinni húðun og hitameðhöndlun örþunnra laga af gulli. Sýnt var fram á framleiðsluaðferðin skilaði yfirborðum með breiða stærðardreifingu gullagna í nanóstærð og jafna dreifingu sterkrar yfirborðsmögnunar innfallandi rafsegulgeislunar. Tölulegir útreikningar á mögnunarstuðlum voru framkvæmdir til að tryggja háa og jafndreifða mögnun litrófsmerkis yfir stærri svæði. Niðurstöður útreikninga voru staðfestar með tilraunum sem sýndu fram á allt að milljónfalda mögnun Raman ljósdreifingar við yfirborðin. Lífsamhæfni yfirborðanna var sannreynd með lífvirkniprófum og flúrljómunarlitun sem staðfestu að yfirborðin sýndu eðlilegan frumuvöxt og fjölgun. Gagnsemi yfirborðanna við rannsóknir á frumum yfir lengra tímabil var staðfest með því að fylgja eftir breytingum í Raman-rófum frá frumuhimnum mesenkímal bandvefsfruma við beinsérhæfingu. Svipgerð frumanna var staðfest samhliða með stöðluðum aðferðum. Niðurstöður rannsóknana staðfestu að yfirborðin sem þróuð voru nýtast vel til að fylgja eftir breytingum í samsetningu frumuhimna við beinsérhæfingu þar sem þau sameina smásjármyndatöku og litrófsgreiningu sem birtir efnasamsetningu og efnabreytingar við frumuhimnu, án inngrips. Yfirborðin voru einnig nýtt til rannsókna á lifandi trefjakímfrumum sem gáfu frekari staðfestingu á því að hvorki yfirborðin sjálf né ljósörvunin hefðu neikvæð áhrif á frumurnar. Aðferðir þær sem kynntar eru hér gefa því fyrirheit um að þær megi nýta til að fylgjast með ýmsum frumubreytingum, svo sem beinsérhæfingu lífandi mesenkímal bandvefsfruma, í rauntíma og án inngrips.

Graphical Abstract

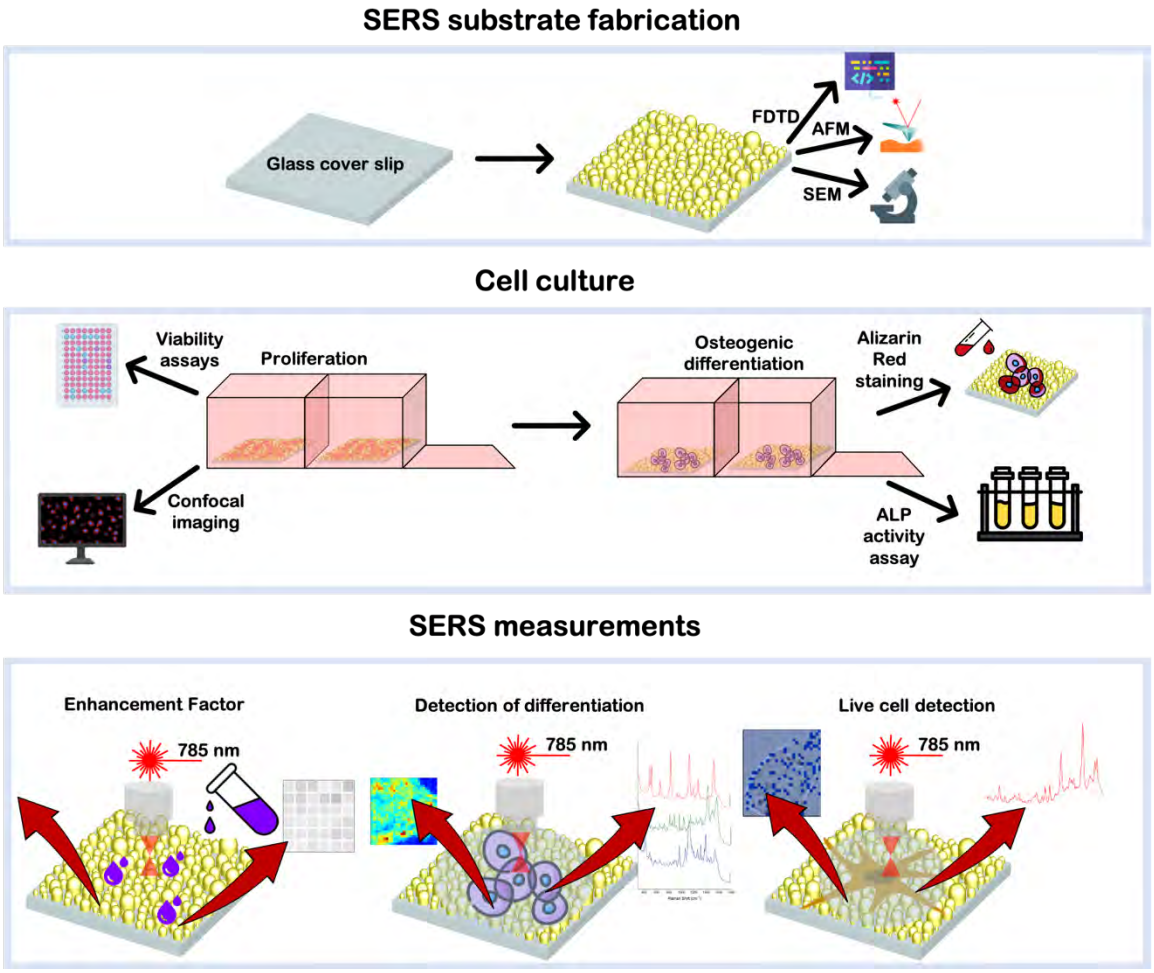

The aim of the present project was to develop a method that will enable highly sensitive characterization of molecular composition of cells without using any destructive nor invasive steps in the analysis process. The graphical abstract illustrates the three main experimental parts composing this thesis. First, fabrication of gold nanoparticle arrays on glass supports as SERS substrates characterized by various techniques, such as AFM, SEM, and numerical simulations. Second, evaluation of biocompatibility of the aforementioned substrates for mesenchymal stromal cell culturing and long-term osteogenic differentiation, assessed by viability assays, immunofluorescence staining techniques and colorimetric assays. Third, Raman and SERS measurements for SERS enhancement factor estimation and detection of molecular fingerprints of the studied cells, as well as signs of osteogenic differentiation. At last, the applicability of the SERS substrates for live-cell measurements was evaluated using cells of fibroblast cell line.

To my beloved grandfather

Acknowledgements

During the past years a lot of people have contributed, directly or indirectly, to making my research work and writing of this thesis possible, and to them – I owe a debt of gratitude.

First and foremost, I would like to thank my doctoral committee Kristján Leósson, Ólafur E. Sigurjónsson, Unnar B. Arnalds and Sigurður Brynjólfsson for their work and supervision. Most of all, I want to express my deepest appreciation to Kristján, my mentor, for the opportunity he gave me years ago when he first hired me for the project and then encouraged me to pursue the Ph.D. Thank you for all you've done for me, for the faith in me, especially at times when I doubted myself, and for all the things I've learned from you – not only about science, but also life, for helping me develop ideas, solve problems on my own, for giving me independence, but not leaving without guidance at the same time. I will be forever grateful that you involved me in various projects and tasks, from supervising students, through conducting multidisciplinary research, writing grants and tender applications, to meetings with industry leaders. You helped me develop as a scientist, but also grow a better person. I could not have imagined a better and more understanding supervisor. Óli, for believing in me and giving me freedom in designing and performing my own experiments, but always being there for me if I needed help or scientific and non-scientific discussions. Unnar, for constant support in the cleanroom work, but also for always having time to talk to me and making sure everything was going according to the plan, as well as for the help in writing the Matlab codes. Sigurður, for ensuring all the administrative matters were in order.

I would like to thank Prof. Janina Kneipp from Humboldt University in Berlin for fruitful collaboration and for welcoming me in her research group. Because of her I finally understood the beauty of SERS and learned how to analyze the spectral data. It was a short visit, but essential to my Ph.D. project and I'm beyond grateful for everything I've learned during my stay - not only scientific, but also what great teamwork looks like. Moreover, I would like to thank Dr. Virginia Merk for performing with me the experimental determination of enhancement factors and for being kind to help me with the data analysis. I am especially grateful to Dr. Vesna Živanović, who spent days with me in the dark lab room recording the first SERS spectra of live cells on my SERS substrates and was equally enthusiastic for each and every strong and beautiful signal. She helped me with the initial analysis of my SERS data and taught me how to process and interpret spectra to obtain valuable information. My stay in Prof. Janina's lab was crucial for interpreting the large amounts of data generated throughout the project and I'm extremely grateful for that.

I would also like to extend the appreciation to all the people from the Innovation Center Iceland and from the Blood Bank, Landspitali University Hospital Iceland, that I have been fortunate to work with. I was honored to use their facilities and resources for the duration of my project and beyond. Thank you for creating a stimulating work environment and for your willingness to help me on various levels. I want to especially thank Gissur Örlygsson, Birgir Jóhannesson, Steinunn Thorlacius and Sævar Ingþórsson for their invaluable technical assistance. A big thank you to goes to all the students at both NMI and the Blood Bank for great time spent together in the offices and the labs.

I want to acknowledge here the funding from the University of Iceland, the Icelandic Research Fund, the Infrastructure Fund and the Landspitali University Hospital Research Fund for providing the financial means essential for conducting this project and for covering travel expenses.

Last but not least, I would like to thank my family for their enormous support and understanding, without them I wouldn’t be in the place I am now. Finally, I would like to conclude by expressing my deepest gratitude to Christian, who has been by my side through all ups and downs and always encouraged me to do better and never give up, no matter what. His care and support over the last years ensured my mental well-being and gave me the confidence needed to achieve this.

Table of Contents

List of figures

List of tables

List of papers

This thesis is based on the following original publications, which are referred to in the text by their Roman numerals (I-IV):

I. **Adrianna Milewska**, Arni S. Ingason, Olafur E. Sigurjonsson, and Kristjan Leosson, "Herding cats: managing gold atoms on common transparent dielectrics", Opt. Mater. Express 9, 112-119 (2019) © The Optical Society

II. **Adrianna Milewska**, Vesna Zivanovic, Virginia Merk, Unnar B. Arnalds, Ólafur E. Sigurjónsson, Janina Kneipp, and Kristjan Leosson, "Gold nanoisland substrates for SERS characterization of cultured cells", Biomed. Opt. Express 10, 6172-6188 (2019) © The Optical Society

III. **Adrianna Milewska**, Olafur E. Sigurjonsson, Kristjan Leosson, "SERS imaging of mesenchymal stromal cells differentiation", ACS Applied Bio Materials 4 (6), 4999-5007 (2021) Copyright © American Chemical Society

IV. Vesna Zivanovic, **Adrianna Milewska**, Kristjan Leosson, Janina Kneipp, "Molecular structure and interactions of lipids in the outer membrane of living cells based on SERS and liposome models", ACS Analytical Chemistry 93 (29), 10106-10113 (2021) Copyright © American Chemical Society

In addition, some unpublished data may be presented. All papers are reprinted with the kind permission of the publishers.

Conference contributions

i. A Milewska, M Miljkovic, I Sokolov, OE Sigurjonsson, K Leosson. Substrates for identification of the bone marrow-derived mesenchymal stem cells by Surface-Enhanced Raman Spectroscopy. Poster presentation. International Workshop on Advanced Materials for Healthcare Application, Reykjavik, Iceland, May 22-23 (2018)

ii. A Milewska, M Miljkovic, I Sokolov, OE Sigurjonsson, K Leosson. Identification of Bone Marrow-Derived Mesenchymal Stem Cells by Surface-Enhanced Raman Spectroscopy. Poster presentation. 4th Annual Meeting of the Scandinavian Society for Biomaterials, Fiskebäckskil, Sweden, April 25-27 (2018)

iii. A Milewska, M Miljkovic, I Sokolov, OE Sigurjonsson, K Leosson. Identification of Bone Marrow-Derived Mesenchymal Stem Cells by Surface-Enhanced Raman Spectroscopy. Poster presentation. SCANDEM Annual Meeting, Kongens Lyngby, Denmark, June 25-28 (2018)

iv. A Milewska, OE Sigurjonsson, K Leosson, SERS investigation of bone marrow mesenchymal stem cells grown on gold nanoisland substrates. Poster presentation. The 19th Biomedical and Health Sciences Conference, Reykjavik, Iceland, January 03 (2019)

v. A Milewska, V Zivanovic, V Merk, OE Sigurjonsson, J Kneipp, K Leosson, SERS investigation of mesenchymal stromal cells grown on gold nanoisland substrates. Poster presentation. Raman Fest, Oxford, England, June 24-25 (2019)

vi. A Milewska, V Zivanovic, V Merk, UB Arnalds, OE Sigurjonsson, J Kneipp, K Leosson, Gold nanoisland arrays as SERS substrates for non-invasive detection of characteristic cellular fingerprints. Oral presentation. Icelandic Biological Conference, Reykjavik, Iceland, October 19 (2019)

vii. A Milewska, V Zivanovic, V Merk, OE Sigurjonsson, J Kneipp, K Leosson, Gold Nanoisland Substrates as Uniform SERS Substrates for Sensitive Detection of Bone Marrow-derived Mesenchymal Stromal Cells Fingerprints. Oral presentation. Biophysical Society 2020 Annual Meeting, San Diego, USA, February 16 (2020)

viii. A Milewska, OE Sigurjonsson, K Leosson, SERS platforms for non-invasive identification of cell differentiation. Online rapid-fire poster presentation. Scandinavian Society for Biomaterials, June 11 (2020) – **1st prize winner**

ix. A Milewska, OE Sigurjonsson, K Leosson, SERS-detection of osteogenic differentiation in stem cells cultured on simple gold nanoisland substrates. Oral presentation (online). Nordic Baltic Conference on Biomedical Engineering and Medical Physics (NBC 2020), Reykjavik, Iceland, September 18 (2020)

x. A Milewska, OE Sigurjonsson, K Leosson, Raman spectroscopy for studying cells and beyond. Oral presentation (online). Current topics in Chemistry and Biochemistry – seminars at the University of Iceland, Reykjavik, Iceland, October 30 (2020)

xi. A Milewska, OE Sigurjonsson, K Leosson, SERS imaging of mesenchymal stromal cells on gold nanoisland substrates. Oral presentation (online). Virtual Early Career European Microscopy Congress (EMC 2020), Copenhagen, Denmark, November 24 (2020)

Declaration of contribution

The doctoral candidate, Adrianna Milewska, is responsible for experimental design, experimental work, data acquisition and analysis, data interpretation and writing of some papers and manuscripts presented in this thesis.

Paper I: Herding cats: managing gold atoms on common transparent dielectrics

The author fabricated SERS substrates by repeated deposition and thermal annealing, performed structural characterization, numerical simulations, cell culturing and SERS measurements.

Paper II: Gold nanoisland substrates for SERS characterization of cultured cells

The author performed all experimental work, including SERS substrates fabrication and characterization, numerical simulations, cell culturing, viability assays and staining procedures, SERS measurements, data analysis, interpretation of the results, and writing of the manuscript.

Paper III: SERS imaging of mesenchymal stromal cells differentiation

The author performed all experimental work, including SERS substrates fabrication, cell culturing and osteogenic differentiation, evaluation of osteogenic differentiation with colorimetric assays and staining procedures, SERS measurements, data analysis, interpretation of the results, and writing of the manuscript.

Paper IV: Molecular structure and interactions of lipids in the outer membrane of living cells based on SERS and liposome models

The author provided SERS substrates for the live cell study and participated in cell culturing on substrates and SERS measurements of live cells.

Abbreviations

AFM – Atomic force microscopy

ALP – Alkaline phosphatase

AuNP – Gold nanoparticle

BMP – Bone morphogenetic protein

BM-MSC – Bone marrow-derived mesenchymal stromal cell

BSA – Bovine serum albumin

CV – Crystal violet

DAPI - 4’6-Diamidino-2-phenylindole

DMSO – Dimethyl sulfoxide

EBL – Electron beam lithography

ECM – Extracellular matrix

EF – Enhancement Factor

FBS – Fetal bovine serum

FDTD – Finite-difference time-domain

HOMO – highest occupied molecular orbital

hPL – Human platelet lysate

IR – Infra-red

ISCT – International Society for Cellular Therapy

LDH - Lactate dehydrogenase

LSP – Localized surface plasmon

LSPR – Localized surface plasmon resonance

LUMO – lowest unoccupied molecular orbital

MSC – Mesenchymal stromal cell

NP – Nanoparticle

OCN – Osteocalcin

OCP - Osteopontin

OSX - Osterix

PB - PrestoBlue

PBS – Phosphate-buffered saline

PCA – Principal component analysis

pNPP – p-nitrophenyl phosphate

qPCR – quantitative polymerase chain reaction

RRS – Resonance Raman scattering

RS – Raman scattering

RUNX2 - Runt-related transcription factor 2

R6G – Rhodamine 6 G

SEM – Scanning electron microscopy

SERS – Surface-enhanced Raman scattering

SOX9 - SRY-Box Transcription Factor 9

SPR – Surface plasmon resonance

TEM – Transmission electron microscopy

UV - Ultraviolet

Chapter 1

Introduction

Since the discovery of the surface-enhanced Raman scattering (SERS) phenomenon by Fleischmann in 1974 [1], research activity in this field has grown rapidly due to a number of parallel developments. These include the detection of single molecules by SERS [2, 3], intracellular studies of cells with SERS probes [4, 5], improvements in nanofabrication techniques of plasmonic surfaces with large field enhancements [6-9], well-controlled chemical synthesis of SERS nanoprobes of different sizes and shapes [9-11], allowing for tunability of their localized surface plasmon resonance (LSPR), as well as increasingly powerful numerical simulation tools able to predict the magnitude of SERS enhancement of the developed nanoparticles and nanostructured surfaces [12, 13].

Vibrational spectroscopy, in particular Raman spectroscopy, uses light to induce vibrational transitions in the system under investigation, e.g., molecules in cells, without the necessity of labeling [14, 15]. The inelastically scattered light from the studied molecules thus carries an information of the response of the system to the incident illumination. This vibrational signature, i.e., "molecular fingerprint" is unique for each molecule and can deliver information about the chemical structure of the system under investigation, as well as the nature of bonding of molecules to the surfaces. This inelastic scattering, however, is an inherently weak process. To increase the sensitivity of Raman spectroscopy, SERS makes use of rough metal surfaces (predominantly gold or silver), but also accurately engineered metallic nanostructures, particularly the small gaps (preferably less than 10 nm) between adjacent metal nanoislands [16, 17], that can enhance the intensity of the Raman bands by many orders of magnitude (typically by a factor of 10^6-10^{12}) [18, 19], due to an increase of the local electric field intensities at the surface, and in the gaps, of the nanostructures.

Detection of biological species ranging from single molecules to whole cells and tissues continues to challenge scientists [20-22]. Current cell analyzing tools consist of a combination of colorimetric assays, quantitative polymerase chain reaction (qPCR) techniques, flow cytometry, chromatography, Western blot analysis and immunofluorescence staining techniques [22, 23]. These conventional methods are vastly effective and relevant for analysis of cells, e.g., in the context of the present study, for the evaluation of the degree of cell differentiation [24]. Nevertheless, most of them have major limitations, i.e., complicated and time-consuming protocols, need for labeling, fixation, and thus, in principle, termination of the cell culture in order to perform the analysis. This can be problematic in case of long-term cell culturing studies, where cells that have to be differentiated for 2-3 weeks undergo destructive steps for their lineage confirmation, which prevents them from reuse after the analysis. Furthermore, some of the abovementioned screening techniques have limitations in resolution and thus cannot be performed at the single-cell level. For example, Western Blot assays and qPCR require a significant number

of cells to perform the analysis, and therefore are unable to reveal their heterogeneity [25, 26]. Immunofluorescence staining techniques, on the other hand, are prone to cross-reactivity when using several antibodies and the irreversible photobleaching of the fluorescent dyes also restricts the temporal resolution [23, 27]. Contrary to fluorescence microscopy, Raman spectroscopy does not require any dyes or labels, and furthermore, Raman bands are spectrally narrow, as compared to spectrally wide fluorescence bands, which allows for demultiplexing of the detected signal from multiple species [14, 27]. However, as the Raman scattering cross-section of biological samples is pretty low, it has to be increased either by using high-intensity lasers and long acquisition times, or by implementing SERS. High laser powers, especially in the visible range, lead to photodegradation [28]. Cell damage, however, decreases with the increase of the laser wavelength [23]. Unfortunately, along with the laser wavelength increase, the Raman scattering probability decreases, therefore requiring significantly higher laser power to maintain the same signal intensity. SERS overcomes this obstacle, as it allows rapid, label-free detection of multiple molecular species without the necessity of using high laser powers.

The most common way of implementing SERS in cell studies involves using colloidal particles of gold [11, 29] that are introduced to the cell interior via endocytosis. Technically, this is an invasive method and, moreover, the SERS signal is obtained only from molecules that are in nm-proximity contact to the metallic particles. In the case of colloidal particles, it is difficult to control where in the cells they will end up, limiting the control over what is actually being measured [30]. Another option for implementing SERS is in form of *in vitro* sensing platforms or substrates, on which cells are cultured. This limits the probing volume to that adjacent to the nanostructured surface. However, this approach can be considered truly non-invasive, if the nanosurfaces are relatively flat, so they do not affect cell growth.

The chemical specificity and high sensitivity of SERS can yield a vast abundance of information, which is its greatest advantage, but also, in some cases, can make the analysis of data overly difficult. In studies of differentiation of mesenchymal stromal cells presented in this thesis, limiting the probing area to the outer cell membrane adjacent to the underlying substrate allows for rejection of signals coming from the cell interior, which are, in this case, irrelevant for analysis. The signs of osteogenic differentiation can be detected at the interface between the SERS substrate and outer cell membrane, where extracellular matrix is produced and subsequently mineralized through calcium phosphate deposition [31, 32]. As visualized by different staining procedures, osteogenesis occurs in discrete clusters in the cell culture, forming dense mineralized clusters, denoted as “bone nodules”, indicating that this process is not homogeneous [33, 34]. Moreover, the populations of mesenchymal stromal cells themselves are not uniform, thus making quantification of lineage potential in such cultures particularly difficult [35, 36]. The lack of repeatable and robust analysis diminishes the therapeutic potential of MSCs in regenerative medicine [37]. Working with mesenchymal stromal cells is a challenge and as there is increasing need for use of MSCs in clinics, there is a critical need to develop methods for non-invasive cell screening. As pervasive heterogeneity of mesenchymal stromal cells manifests itself between different tissue sources, donors, culture methods, and in principle, individual cells, it is also important to take a step back and try to understand these diverse populations throughout their lifespan using the least invasive screening tools [25, 36].

This thesis aims to address aforementioned problems through development and fabrication of *in vitro* SERS sensing platforms for long-term culturing of mesenchymal stromal cells and subsequent detection of their molecular composition. This allows for increased scientific

knowledge to be gained about the process of osteogenic differentiation, including potentially non-invasive detection at the single-cell level. The specific goal of the present project was to fabricate uniform, sensitive and biocompatible semi-transparent (allowing for inverted microscope investigation) substrates for performing SERS measurements of molecular changes in cells, such as chemical events happening on the outer cellular membrane during osteogenic differentiation of mesenchymal stromal cells. In order to validate the technology, its usability, and to prove the biocompatibility of the SERS substrates, multiple viability assays were performed and the interaction of the attaching cells to the substrates was examined. In particular, cytotoxicity of the substrates was evaluated, along with immunofluorescence staining of the cell body anchoring to the underlying surface of the SERS substrates and compared with conventional cell culturing slides. Furthermore, long-term proliferation and differentiation on the SERS substrates was assessed. The results suggest that the cellular processes are not compromised by the presence of the nanostructured surface. In addition, live-cell measurements of fibroblast cell line were performed, indicating usability of such substrates in live-cell studies.

Chapter 2

Background and Literature Review

2.1 Raman scattering

Raman scattering is a phenomenon in which photons incident on a sample are inelastically scattered after exchanging energy with the vibrational states of the studied sample. This effect was discovered independently in 1928 by Raman and Krishnan [38, 39] in solutions and Landsberg and Mandelstam [40, 41] in crystals, after first being assumed by Smekal in 1923, who showed that monochromatic light after scattering has not only the original frequency, but also frequencies of higher and lower wavelength [42]. In 1930, C. Raman received the Nobel prize for his discovery, and the effect was subsequently named after him.

When photons interact with molecules, a temporary transition between energy states occurs. In the quantum-mechanical picture, this increase in energy of the molecule can be viewed as taking place through a virtual electronic state (Figure 2.1). The excited molecule can return to the same energy state by emitting the same amount of energy, as was absorbed from the incident photon. In this case, since there is no overall change in energy, the scattered photon has the same frequency as the incident photon. This process is called elastic Rayleigh scattering. However, inelastic scattering is also possible, where the molecule emits a different quantity of energy, as compared to the energy of the incident photon. This phenomenon is known as Raman scattering and it occurs rarely. Only 1 in 10^8 scattering events will be inelastically scattered [43, 44]. We can distinguish two types of Raman scattering, shown on Figure 2.1:

i) the emitted photon has lower energy than the incident photon, known as Stokes scattering, or
ii) the emitted photon has higher energy than the incident photon, known as anti-Stokes scattering.

In Stokes scattering, the scattered photon loses energy equal to that of the energy difference between particular vibrational states and decreases in frequency (increases in wavelength). In anti-Stokes scattering, the photon is scattered by a molecule initially in an excited vibrational state. Therefore, the emitted photon gains energy and increases in frequency (decreases in wavelength) as the molecule drops to a lower vibrational state. The frequency changes of the scattered photons therefore provide structural information of the studied molecules by revealing the energies of their vibrational transitions. A special mode of Raman scattering occurs when the Raman emission can be significantly enhanced, if the molecule

is irradiated with exciting radiation in resonance with one of its electronic transitions, called resonance Raman scattering (RRS) (Figure 2.1 D). The smaller the frequency difference between laser and electronic transition, the stronger the RRS intensity. In resonance Raman scattering only the vibrations coupled to the chromophore group are intensified in the spectrum, which allows both for selectivity and sensitivity [45]. In case of resonance excitation, however, the photoinduced changes of molecular structure and fluorescence background can complicate the resonance measurements.

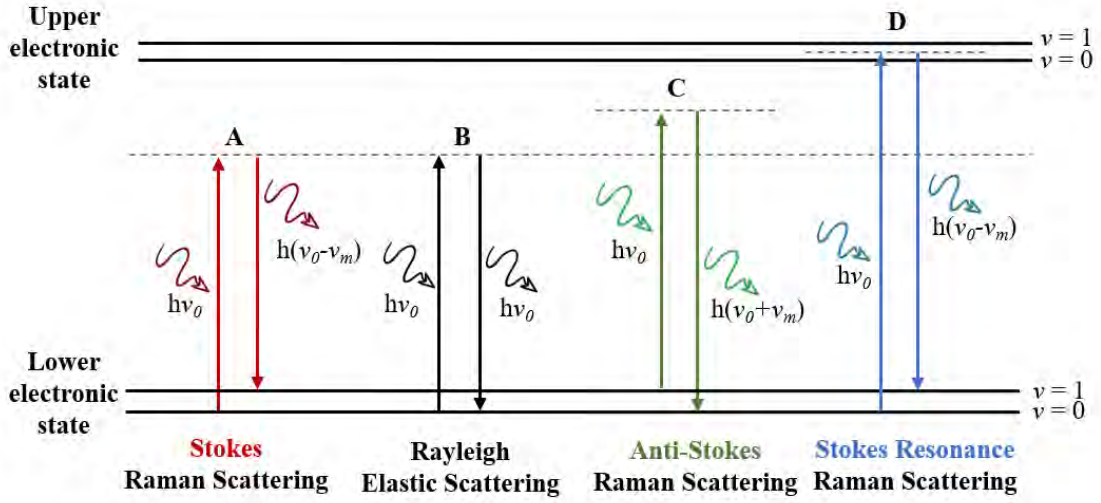

Figure 2.1 Jabłoński energy level diagram describing energetic transitions involved in Raman scattering. A) Stokes Raman Scattering, B) Rayleigh Elastic Scattering, C) Anti-Stokes Raman Scattering, D) Stokes Resonance Raman Scattering. Dashed lines represent virtual excited electronic state, υ_0 and υ_m denote the frequencies of the incident photon and the molecular vibration, respectively.

Not all molecular vibrations are Raman active. Raman scattering is related to the molecular polarizability, in other words, the deformation of the bond between the atoms induced by the light [14]. For example, if both bonds of carbon dioxide are stretched (Figure 2.2), the overall polarizability changes and the symmetric stretch is Raman active. However, there is no change in the molecular dipole moment, so the stretch is not observed in infrared spectroscopy, a vibrational spectroscopy based on absorption of light corresponding to the energy difference between the vibrational states (typically corresponding to wavelengths of 2.5-25 μm). In the asymmetric stretch, one bond is more polarizable than the other, and the change in polarizability of the longer bond is exactly offset by the change in the shorter bond, therefore the overall polarizability does not change, and this vibrational state is therefore not Raman active. Infrared spectroscopy, on the other hand, can detect the asymmetric stretch of carbon dioxide.

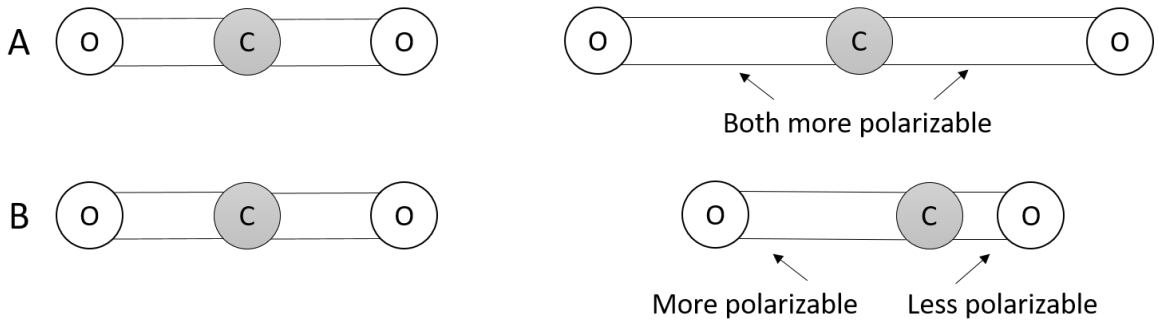

Figure 2.2 Schematic representation of A) symmetric stretching in carbon dioxide molecule, which is Raman active due to change in polarizability and B) asymmetric stretching in carbon dioxide molecule, which is not Raman, but IR active due to lack of change in polarizability but change in the dipole moment.

Since Raman scattering involves excitation by light, it can be conveniently implemented as a microscopic imaging technique. Raman imaging has several advantages over other imaging techniques. In principle, it is non-invasive, non-destructive and does not require labeling, unlike fluorescence microscopy. These advantages are also shared by IR spectroscopic imaging, which can also reveal detailed molecular information. These are complementary techniques, however, they are based on different interactions of the studied molecules with the light photons, as explained above. An advantage of the Raman spectroscopy over IR is that it requires little or no sample preparation while in IR sample preparation is important. The IR technique suffers from other shortcomings - mainly the strong absorption of water, which makes analysis of samples in aqueous environments complicated, severely limiting its application to biological samples [27]. Conversely, in Raman spectroscopy, the water signal is weak and is usually neglected, making it preferred method for biological applications, as cells can be maintained in their natural physiological conditions. On the other hand, absorption infrared signals are generally strong and the IR technique is well-established, and interpretation of results can therefore be more reliable, contrary to the Raman scattering which suffers from extremely low efficiency, making it difficult to detect low level species and to track biological events over time.

Conventional Raman instruments are composed of a stabilized and spectrally pure laser source, a spectrometer and a detector, including notch or edge filters for effectively blocking the light from the excitation laser in the detection path. Notch filters reject the light at the laser wavelength and transmit both Stokes and anti-Stokes Raman scattering, whereas edge filters transmit either Stokes (long-pass edge filter) or anti-Stokes (short-pass edge filter). A Raman imaging system furthermore consists of a microscope configured for excitation and detection. Monochromatic excitation laser wavelengths used in Raman analysis range from deep-UV to near-IR, thus covering a wide spectral range. The choice of excitation wavelength depends on the application. For example, in bioanalysis, the red HeNe laser line at 632.8 nm is often preferred, as well as near-IR 785 nm and infra-red 830 nm diode lasers or 1064 nm Nd:YAG, since they significantly lower the autofluorescence background, which is unavoidable in biological samples. Moreover, due to use of low energy photons, the sample is less prone to photodegradation [28].

Raman spectrometers can be coupled to a cell incubator, that can maintain normal physiological conditions for cells, i.e., 37°C, 95% humidity and 5% carbon dioxide level environment. This solution is an answer for increased need for a model accurately

representing the cell or tissue behavior in their natural physiological conditions. The main drawback of conventional Raman spectroscopy, however, is the inherently low intensity of the signal, as discussed above. In order to increase it, high laser powers must be used, which can easily lead to overheating and subsequent destruction of the studied sample. This is a particular downside in the studies of biological systems.

2.1.1 Raman scattering in bioanalysis

Since one of the fundamental benefits of Raman spectroscopy is the ability to define the chemical structure of studied molecules in a non-invasive way, its potential in bioanalysis is substantial. To date, Raman spectroscopy has been used in discrimination between healthy and unhealthy tissues and in cancer diagnosis [46, 47], in cell differentiation studies [48-52], apoptosis [53-55], interaction of drug molecules with cells [23, 56], and others, both at the single-cell level and tissue level [57-59].

Vibrational spectroscopy methods, such as Raman and IR, are preferable techniques in studies of complex biological samples, particularly because they show high molecular specificity, allowing simultaneous identification of many molecules, due to the narrow bands present in the vibrational spectrum. This is what is often referred to as the "molecular fingerprint" that is unique for each molecule. Moreover, unlike fluorescence, to obtain valuable molecular information external markers and labels are not required. Such labeling is prone to photobleaching of the induced fluorophores upon optical excitation, directly affecting cell physiology, and therefore, fluorescence imaging might not reflect the normal cellular environment [15]. In contrast, Raman and IR spectroscopies are label-free and non-destructive. Moreover, Raman spectroscopy can achieve better spectral and spatial resolution, due to narrower linewidths, as compared to infra-red spectra composed of broader, less-resolved bands that make identification of specific molecules in complex systems more difficult [60].

The ability to monitor chemical events in complex cellular environments by Raman spectroscopy has gained enormous interest over the last decades. For example, D'Acunto et al. [61] used Raman imaging to distinguish between normal and cancer cells at the tissue level, to discriminate the level of malignancy of the tumors under investigation. By comparing changes in intensities of several bands assigned to key molecular species, such as proteins, DNA, or lipids, they were able to determine the degree of tissue degradation. A similar method of Raman imaging was applied by Abramczyk et al. in the extensive studies on breast cancer diagnosis, highlighting the differences in lipid profiles between cancer and normal cells, suggesting that lipids play important role in the molecular mechanisms of carcinogenesis [46, 47, 62]. Raman spectroscopy was used to distinguish between undifferentiated and differentiated stem cells during osteogenesis, by following the changes of hydroxyapatite band intensity at 960 cm^{-1}, as reported by McManus et al. [49], Hung et al. [50] and Gao et al. [51]. Furthermore, the changes in cellular fingerprints induced by drug uptake have been monitored [23, 56]. Such alterations in spectral fingerprints are, however, usually difficult to discriminate, as Raman spectroscopy is not sensitive enough to spot the small changes in the cellular environment induced by drugs, especially if they are of low concentration.

Despite its advantages, Raman spectroscopy has some major limitations. First, it suffers from extremely low signal level, making it difficult to image and track chemical events in

biological samples over time. Second, Raman spectra of chemically heterogeneous samples are particularly complicated, where peaks from different molecules overlap, making it difficult to directly extract meaningful information. However, several developments have been made to improve the weak Raman scattering and to increase chemical specificity of Raman spectra by employing different methods, such as surface-enhanced Raman spectroscopy (SERS).

2.2 Surface-enhanced Raman scattering

A surface-enhanced Raman scattering (SERS) spectrum was first observed and recorded by Fleischmann et al. in 1974 for pyridine adsorbed on electrochemically roughened silver electrode [1]. Initially, the authors attributed the unusual intensity of the Raman scattering to the increased surface area of the rough substrate. It was not until 1977 that the SERS effect was independently described by Jeanmaire and Van Duyne [63] and Albrecht and Creighton [64]. Jeanmaire and Van Duyne measured the dependence of the Raman scattering of all the surface pyridine bands on the applied electrode potential [63]. They proposed that the enhanced intensities of Raman signal of pyridine were related to an electric field modulation of the Raman scattering tensor of the adsorbed molecule, in analogy to previously observed electric-field-enhanced Raman scattering in semiconductors [65]. They pointed out that the effective Raman cross-section was magnified by a factor of approximately 10^6. Albrecht and Creighton studied the change in the intensity of the Raman signal of pyridine during a single redox reaction [64]. The recorded Raman spectra of pyridine during and immediately after the redox cycle were remarkably intense. They calculated that the enhancement of Raman scattering was roughly 10^5 as compared to corresponding signals from liquid pyridine. As a possible explanation of the enhanced Raman signals, they proposed that broadening of the electronic energy levels of pyridine molecules at roughened metal surfaces might induce resonant Raman scattering from molecules adsorbed on metals through interaction with surface plasmons, as had been previously suggested by Philipott et al. [66].

Later that year, Moskovits, after hearing the talk of Van Duyne about the SERS effect during an ACS conference in Chicago, realized there is a connection between the SERS effect and the localized surface plasmon resonance (LSPR) that he was working on [17, 67]. Since then, LSPRs have been recognized as a main cause of the striking enhancement of the Raman signals in proximity to metallic nanostructures. This effect is now called the electromagnetic mechanism of SERS. In addition, the modification of the polarizability of a molecule due to the interaction with the surface of the metal through a charge-transfer resonance process is referred to as the chemical enhancement, which also contributes to the overall SERS effect. However, this contribution is generally much smaller and depends on the type of molecule [18, 68].

Therefore, SERS combines high sensitivity with the advantages of Raman spectroscopy, which include a) molecular identification due to vibrational fingerprints of the molecules in complex environments, i.e., simultaneous detection of various analytes, b) non-invasive analysis, c) minimal or even no sample preparation, d) ability to study samples in water-based media due to weak Raman scattering of water.

2.2.1 Origins of the SERS enhancement

Electromagnetic enhancement

When incident laser light interacts with a metal-dielectric interface, it leads to a collective oscillation of the delocalized (conduction) electrons of the metal nanostructures. Once the frequency of the incident light matches the resonant frequency of the free electrons in the metal, a surface plasmon resonance (SPR) occurs [69]. The collective oscillating mode of the electrons and the nanostructures supporting them are referred to as surface plasmons and plasmonic substrates, respectively. In metallic nanostructures, when surface plasmons are confined to a space of a size smaller or comparable to the wavelength of the incident electromagnetic radiation, the collective oscillations do not propagate, but become highly localized to a specific position in an optical phenomenon called localized surface plasmon resonance (LSPR) [16, 70-72] (Figure 2.3). Therefore, the main difference between SPR and LSPR resides in the length scale of the structure supporting the plasmon oscillation [73]. As a result of LSPR, the high local field of the induced dipole enhances the electromagnetic field of the incident light. If a molecule is present in this field, its Raman scattering will be accordingly enhanced.

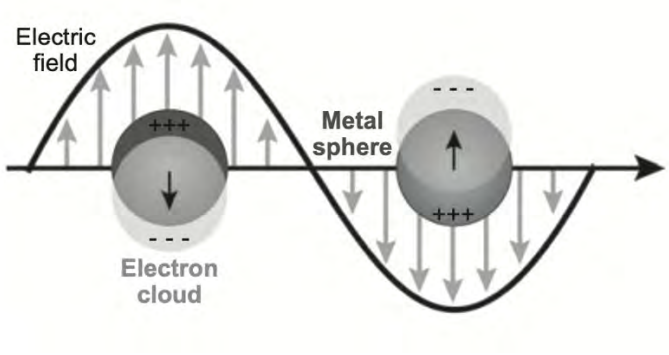

Figure 2.3 Schematic illustration of the localized surface plasmon effect in a metal sphere induced by the electromagnetic wave. Adapted from [72].

In principle, the electromagnetic field enhancement in SERS is a two-step mechanism. First, the local electromagnetic field enhancement occurs on the metallic nanostructure at the incident frequency (ω_0). In this step, the plasmon resonance excited by the electromagnetic field generates large local fields (E_{loc}), that excite the target molecules of the analyte. Second, the emitted field from a molecule again interacts with the metal nanostructure, enhancing the Raman scattered light that is re-emitted at the frequency ω_R, as shown schematically in Figure 2.4. Therefore, the enhancement factor in each step is proportional to the square of the local electric field (E_{loc}) at the incident and Raman Stokes- or anti-Stokes-shifted frequency (ω_0 or ω_R, respectively), together yielding an overall SERS enhancement factor proportional to the fourth power of the enhancement of the local electric field [4, 16, 18, 72, 74, 75], as given by Eq. (1):

$$EF = EF(\omega_0)EF(\omega_R) = \frac{|E_{loc}(\omega_0)|^2|E_{loc}(\omega_R)|^2}{|E_0(\omega_0)|^2|E_0(\omega_R)|^2} \approx \frac{|E_{loc}(\omega_0)|^4}{|E_0(\omega_0)|^4} \quad (1)$$

where E_{loc} and E_0 are local electric fields in the presence or absence of the metallic nanostructure.

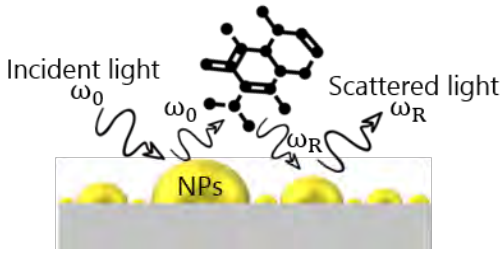

Figure 2.4 Schematic outline of the electromagnetic enhancement. Two-step enhancement. 1. Enhancement of the local incident field on the analyte. 2. Enhancement of the re-emitted Raman scattering from the analyte

The nature of the electromagnetic enhancement is strictly related to the properties of the plasmonic nanostructure (material, size, shape) and the surrounding dielectric, which is usually air or water. It is independent of the type of molecule and does not require direct contact between molecule and metallic surface [4, 30]. However, it rapidly decreases with growing distance *d* from the surface, for example with a decay ~$1/(r+d)^{12}$, in the case of a sphere of radius *r* [4]. Materials that support a strong LSPR effect are mainly coinage metals like gold, silver, or copper [72]. The magnitude of enhancement factor is frequency-dependent, and the enhancement is particularly strong when the frequencies of both incident and scattered fields are in resonance with the surface plasmons [76].

In order for the nanoparticles to induce the SERS phenomenon, their sizes have to be small compared to the wavelength of the incident light. Ideally, their size should be ranging from 5 to 100 nm [71]. For smaller structures, the effective conductivity and light scattering properties, essential for SERS enhancement, diminish. As particles grow in size, the SERS enhancement increases, although for particles, whose sizes approach the scale of the excitation wavelength, non-radiative multipoles are preferably excited, and the SERS effect no longer applies.

Shape also plays an important role in determination of the enhancement factors. For single, colloidal spheroids of gold or silver, the maximum values of electromagnetic enhancement are of the order of 10^6-10^7 [4, 77, 78]. It has been reported that higher enhancement can be achieved for particles with sharper tips, such as triangular prisms [79]. However, when two or more particles (nanoaggregates) are brought closely together, the enhancement in the junctions between them can be greatly amplified, so if a molecule finds itself in close proximity to such junction, a SERS enhancement of 10^{11} can be obtained, assuming that the distance between the particles is close to 1 nm [71]. This small nanogaps result in so-called electromagnetic “hot spots” and in the strong local fields of such nanoaggregates even single molecules can be detected [2, 3].

Chemical enhancement

Although the electromagnetic enhancement is the main contributor to the SERS enhancement, there are some properties of SERS that cannot be explained exclusively by the electromagnetic mechanism and are dependent on the type of molecule, its orientation and therefore its interaction with the plasmonic surface. This effect is referred to as the chemical enhancement. When a molecule adsorbs on the surface of the metal nanostructure, it results in a metal-molecule complex formation, which relies on changes in the polarizability [80]. The chemical enhancement is considered a short-range effect, and unlike the electromagnetic

enhancement, it requires direct contact of the molecule with the substrate [81]. Several theories have been proposed to explain the chemical enhancement of a molecule chemisorbed on a metal [82], such as non-resonant chemical effect or resonant charge transfer chemical effect, the latter being schematically shown in Figure 2.5.

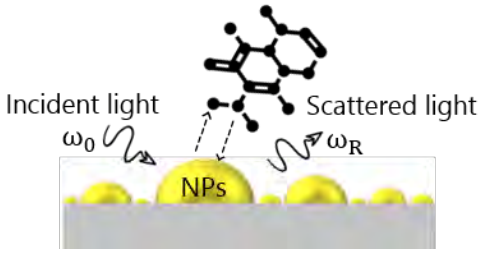

Figure 2.5 Schematic outline of the chemical enhancement. Formation of a new molecule-metal surface complex (modification of the adsorbate polarizability). Charge transfer between the molecule and nanoparticle

The charge transfer chemical enhancement can be described by the molecular transitions between highest occupied molecular orbital (HOMO) and the lowest unoccupied molecular orbital (LUMO), which are symmetrically distributed in energy with respect to the Fermi level of the metal [4, 81] (Figure 2.6). Upon excitation with incident light, an electron-hole pair of the metal is created and the excited electron tunnels into the LUMO orbital of the adsorbate, consequently forming the new equilibrium state. Next, the excited electron travels back to the metal and initiates the emission of the Raman-shifted photon. The contribution of the chemical enhancement is considerably smaller than the electromagnetic one and is estimated to reach the magnitude of $10\text{-}10^2$ [81]. The electromagnetic and chemical enhancements are usually treated as separate phenomena. Although there is no consensus on complete SERS enhancement understanding, the contributions of both mechanisms cannot be neglected in the overall SERS effect.

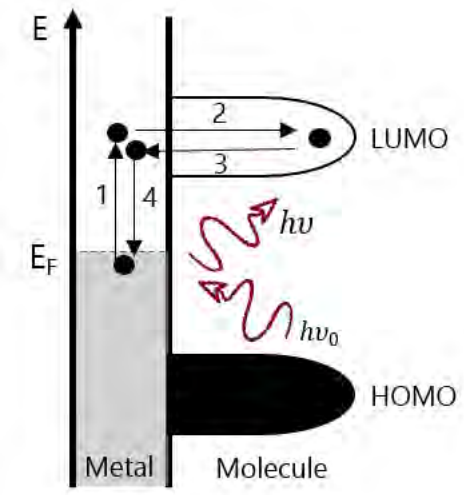

Figure 2.6 Energy level diagram for a metal-molecule complex displaying the band structure of the metal and the HOMO and LUMO levels of the adsorbed molecule upon excitation with the light

2.2.2 SERS substrates: an overview

The first substrates for SERS were electrochemically roughened silver electrodes [1]. Since then, a vast number of different kinds of SERS substrates have been fabricated. In principle, SERS substrates can be divided into three categories: i) nanoparticles in colloidal suspensions; ii) nanoparticles immobilized on solid substrates (bottom-up approach); and iii) nanostructures fabricated directly on solid substrates (top-down approach) [83]. In recent years, fabrication techniques have become more precise and controllable. As a result, SERS has become an attractive tool in quantitative analysis, trace analysis and biological systems analysis [30, 84-87]. However, for the SERS substrate to be applicable, it must meet several criteria, apart from providing high enhancement of Raman scattering. These were outlined before by Natan [88], Lin [9] and summarized by Pilot [30] as follows:

1. High (or sufficient) average enhancement, which can allow for more sensitive and faster analysis.
2. Uniformity, so there are no major differences in enhancement factors over the whole surface, preferably with deviation in enhancement <20%.
3. Reproducibility, the enhancement variations between substrates fabricated in different batches by the same method should be <20%.
4. Stability, so the high enhancement effect can still be maintained after a long shelf life.
5. Large area, specifically important for studies of larger biological systems, such as growing cells or for portable Raman measurements, preferably in mm^2.
6. Cleanliness of the surface, especially important in studies of biological samples or trace analysis, where the residual contaminants from the production process could affect the analysis.
7. Ease of fabrication and low costs of production, both important for widespread of the SERS technique.

At present, SERS substrates that can meet all the above-mentioned requirements are still difficult to obtain. However, a good substrate will be a compromise among these features and will depend strictly on the application. For example, for quantitative analysis, a uniform and reproducible substrate will be favored, for trace analysis the high enhancement will be essential, and for bioanalysis cleanliness, large area, and uniformity along with sufficient enhancement will be relevant.

Colloidal nanoparticle substrates

To date, colloidal suspensions of spherical silver or gold nanoparticles are the most widely used in SERS experiments. Colloidal nanoparticles can be obtained by physical or chemical methods. The chemical reduction of a precursor metal salt with citrate, sodium borohydride or alcohols are the most commonly chosen protocols for nanoparticle synthesis [89, 90]. Nanoparticles of different sizes, shapes and compositions can be achieved by adjusting the preparation protocols, e.g., the type of metal salt used and its concentration, reaction temperature, pH, etc. [9-11]. Therefore, the properties of the nanoparticle substrates can be easily modified by changing the particle size, shape, and material, allowing to move the plasmon resonance over a wide range of frequencies. Most of the spherical particles have their LSPR in the visible range, however, for biological applications it can be favorable to tune the excitation to the near-infrared range to avoid fluorescence. For example, Au nanorods exhibit an absorption band around 800 nm and are therefore ideal for the

commonly used 785 nm laser excitation. Other colloidal structures offering greater field enhancements include nanocubes [91, 92], nanotriangles [93, 94], nanoblocks [95, 96], nanorods [97, 98], nanostars [99-102] and nanoflowers [103, 104]. Moreover, adding salts to such colloids can induce aggregation of the particles, which can boost the enhancement of the local fields by several orders of magnitude as compared to their single-particle counterparts. The main drawback of this method, however, is that the aggregation process is difficult to control and often leads to non-reproducible results, making colloidal SERS substrates unsuitable for e.g., quantitative analysis.

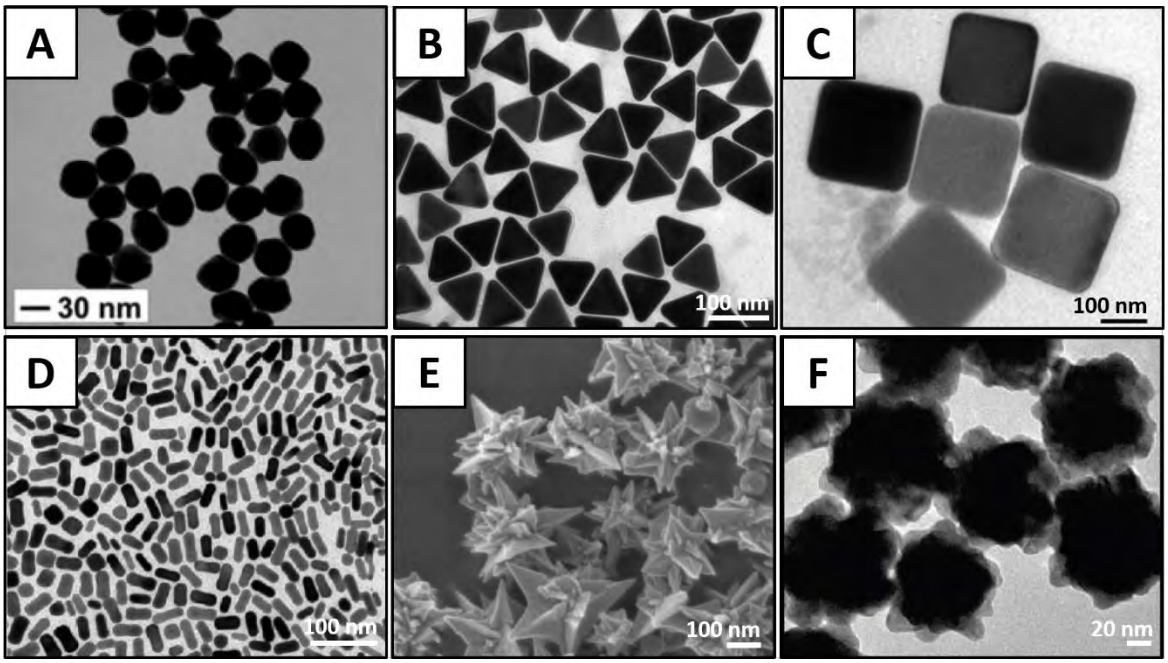

Figure 2.7 TEM images (E – SEM image) of different types of colloidal SERS substrates. A) spherical gold nanoparticles [105], B) gold nanotriangles [94], C) silver nanocubes [91], D) gold nanorods [98], E) gold nanostars [100], F) gold nanoflowers [103]

Immobilized nanoparticles

In order to improve SERS substrate reproducibility, Natan's group developed a method to deposit metallic nanoparticles on solid substrates in a more controlled fashion [106, 107]. They immersed chemically modified polymer surfaces with exposed groups of amines in solutions containing gold or silver nanoparticles, which self-assembled in monolayers on the surfaces, yielding good uniformity among substrates. This method is rather flexible, allowing for self-assembly of various nanoparticles with different size, shape, or composition, as well as different supports to be used, e.g., silicon, quartz, or glass. The controlled immobilization of nanoparticles improves reproducibility and distribution of "hot spots" over the large areas of the substrates, as compared to the simple drop cast procedure, in which colloidal nanoparticles are immobilized on glass by deposition and subsequent drying of a droplet of nanoparticle colloids [108, 109]. During evaporation, the nanoparticles aggregate and create the so-called "coffee ring effect", which leads to random, and therefore highly inhomogeneous, formation of SERS active sites exclusively at the contact line of the drop. Advantages of controlled immobilization of nanoparticles are simplicity and low costs of production without specialized equipment needed, along with substrate uniformity and significant enhancement. Nevertheless, these substrates require additional surface cleaning

due to possible remaining reductants or surfactants that upon interaction with the nanoparticles can reduce the number of SERS active sites and hinder the adsorption of the molecules of interest at the SERS surface. Moreover, cleaning methods have to be chosen carefully, because they can cause uncontrollable aggregation or even precipitation of nanoparticles, resulting in decrease of the SERS signal [9, 30].

Highly ordered arrays of nanoparticles

Although bottom-up methods of nanoparticle immobilization can produce uniform and reproducible SERS substrates, it is still difficult to control the size of the gaps between the particle aggregates. Modern nanolithography and related template methods benefit from generating highly organized particle arrays with great control over particle size and interparticle spacing, at least down to the 10-nm range. Among various reported lithographic techniques for fabrication of high-quality SERS substrates are nanosphere lithography and electron beam lithography. Van Duyne and his group were pioneers of nanosphere lithography, where they spin-coated silica or polystyrene spheres over a clean glass substrate and subsequently deposited a silver film over the array of nanoparticles [8, 110]. This type of substrate is called a "film over nanospheres" (FON) surface. Alternatively, the spheres can be also chemically etched, leaving an array of periodic silver triangles [111]. Tuning of the SERS enhancement and LSPR position in this technique can be achieved by controlling the size and shape of the spheres used for the template and the thickness of the metallic film evaporated on the surface. These surfaces can yield an enhancement factor of the order of 10^8 [8, 110]. Nanosphere lithography is an inexpensive and highly reproducible nanofabrication technique, however, it might be challenging if the size of the spheres is smaller than 200 nm and highly ordered arrangements of such structures across large areas is still difficult to achieve [9].

The ultimate method for creating sophisticated patterns of particles with arbitrary shapes and precise tuning of the interparticle gaps is electron beam lithography (EBL) [112, 113]. This technique seems ideal for fabrication of highly uniform and reproducible SERS substrates, as it allows for fine control over the size, shape and nanogaps between the ordered structures, having considerably high resolution (around 10-20 nm) [30], however, bottom-up self-assembly methods are able to provide smaller gaps, and therefore stronger "hot spots", but the reproducibility is much lower than EBL. Among the recently engineered structures with EBL are arrays of nanoholes [114], nanodiscs [115, 116], nanowells [117], nanocrescents [118], bowtie nanoantennas [119], as well as aperiodic arrays [120]. The process of electron beam lithography consists of few steps: coating the glass or silica substrate with a layer of negative or positive e-beam resist, followed by patterning with electron beam that alters the solubility of the resist. In principle, positive resists become soluble after exposure to electron beam, whereas negative resists become insoluble after electron exposure. Next, the resist is developed by immersion in a solvent that removes the soluble part of the resist. This is followed by evaporation of metal over the patterned structure and dissolution of the remaining resist, resulting in the formation of a metallic pattern engineered before by the electron beam (lift-off method). Alternatively, reactive ion etching (RIE) can be used to write the pattern into the substrate, where the substrate is etched and not the resist polymer. Subsequently, the resist is removed and metal can be evaporated on the pre-patterned substrate, thereby covering the whole surface with metal [121, 122]. Precisely patterned nanostructures can be obtained also with focused ion beam (FIB) technique, which uses high-energy gallium ions to fine etch nanoengineered patterns without masks in a controlled fashion [123, 124]. Although EBL, RIE and FIB allow for high control of the geometry of

the substrates that yield high enhancement factors, they are not suitable for fabricating large-area substrates or for commercialization, as they have rather low throughput and require expensive equipment.

Vapor deposition

A well-known phenomenon utilized for the fabrication of SERS substrates with evaporation or sputtering of thin silver or gold films on common dielectric substrates, e.g., glass, is formation of nanoislands [19, 125-127]. Initially, evaporated gold follows a predictable pattern of island nucleation, which further extend their size and coalesce, and eventually form, around the percolation threshold, a semi-continuous film that gradually evolves into a continuous thin film [128]. Considerable interest in semi-continuous metal films near the percolation threshold is motivated by their remarkable ability of generating local electric field enhancements under illumination, in small gaps, so-called “hot spots”. Gold atoms exhibit high mobility on the dielectric substrates and the deposited metal self-organizes into an energetically favorable state, i.e., continuous, or discontinuous films, depending on the temperature, substrate material, metal involved and its evaporated amount [129]. Therefore, when the thickness of evaporated metal is sufficiently small, the metal tends to merge into small islands, instead of forming homogeneous films. The evaporation techniques have proved to result in small gaps between isolated islands (sub-10 nm) over large areas. They are fabricated in a vacuum environment, resulting in clean substrates that can generate high SERS enhancement, which can by tuned by varying the initial film thickness/deposition time [130]. Upon increase of the evaporated metal thickness, the islands start to merge, forming more continuous films [19], subsequently losing their SERS properties. By applying high-temperature annealing, self-organized aggregation of the metallic nanoislands into larger particles can be prompted. Recently, plasma etching has been applied to generate a similar effect [131]. Various types of SERS substrates have been fabricated with the combination of vapor deposition techniques and thermal annealing [132-136]. In fact, many of them proved to be highly reproducible, even though the process of island formation in these methods is somehow random. It has been reported that the highest SERS enhancement can be generated in the gaps smaller than 10 nm between the islands of bigger sizes [75, 137]. However, if the size of the islands is being increased by annealing, consequently the size of the nanogaps also increases [133]. Repeating the evaporation and annealing processes can provide enlarged metallic nanoislands with small gaps spacing and smaller secondary nanoislands embedded in the gaps, which increase the number of plasmonic hot spots, and thus enhance the local fields in the gaps [130, 136, 137]. The evaporation technique has several advantages such as high cleanliness, simple fabrication over large areas, relatively low cost, along with sufficient SERS enhancement (reported enhancement factor of the order of 10^7) and high reproducibility, despite the fact that the size and shape of the nanoislands cannot be controlled in precise manner. Although fine tuning of the particle sizes by repeated metal deposition and annealing processes seems challenging, recent developments, including the present work, indicate that reproducibility of high and uniform enhancements can be obtained and such substrates, consequently, meet the majority of “ideal” SERS substrate’s criteria.

Multiple other methodologies have been explored to fabricate SERS substrates of high enhancement and high reproducibility, including 3D and flexible structures (e.g. leaning nanopillars [138], nanofingers on nanowires [139], SERS substrate on paper [140, 141]), as well as so-called SERS nanotags coupled with specific labels for selective detection of

molecules, compounds of interest and they are extensively described elsewhere [30, 84-86, 142-144].

2.3 SERS analysis of cells

When studying cells with label-free SERS, several factors must be taken into account. First and foremost, the potential nanotoxicity of the used SERS probes, tags or substrates has to be considered, as they will directly interact with the cells under study [84]. Gold is known to be a biocompatible material [5], however, the nanotoxicity issue is still controversial and there are reports showing that gold nanoparticles might disrupt gene expression after continuous exposure [145], as well as causing DNA damage that consequently leads to cell apoptosis [146]. At the same time, gold can be excited at the near-IR wavelengths, reducing the fluorescence background and thermal damage through the use of lower energy photons, as compared to the visible laser wavelengths [28]. In contrast, silver is considered significantly more toxic than gold, and it can easily induce oxidative stress, increased production of reactive oxygen species (ROS) and DNA damage [144, 147, 148]. Therefore, even though silver is able to generate stronger SERS enhancement and covers a wider excitation wavelength range, gold is the preferred material in biological studies [144].

SERS detection of cells can be achieved in two different ways – either directly (label-free) with the use of SERS probes or substrates, or indirectly with the use of SERS tags (labels). SERS tags consist of a plasmonic core (e.g., gold nanoparticle) to which strong Raman scattering molecules are attached, called Raman reporters. To this basic structure, usually a protective shell is added, which can be functionalized with targeting moieties, e.g., antibodies, to enable a specific analyte binding feature, providing enough sensitivity for trace analysis [30, 149, 150]. Owing to the nature of the SERS mechanism, SERS substrates have to be located in a close vicinity to the target molecules, preferably within 10 nm distance [75]. For direct protocol, to date, the most widely used SERS nanoprobes are aggregates of gold nanoparticles, which are internalized into the cells by endocytosis [4, 76, 151]. As soon as the particles come into contact with cells, complex interactions on newly formed nano-bio interfaces occur [144, 152, 153]. Specifically, nanoparticles are surrounded by biomolecules, mainly proteins, and so-called protein corona is formed [154]. This widely known phenomenon of protein corona formation around nanoparticles poses some limitations in effective SERS detection [155, 156]. In intracellular measurements, SERS nanoprobes need to form aggregates in order to generate sufficient enhancement and be located in exact position to the specific subcellular compartments of interest, which in principle is difficult to control. Surrounding molecules of the protein corona compete with the target molecules for adsorption on the SERS substrates and, furthermore, they prevent nanoparticle aggregation, significantly decreasing or even suppressing the formation of hot spots [156]. Thus, it has to be kept in mind that the protein corona may contribute to the SERS signal of the studied cells. Nevertheless, intracellular SERS measurements are being used in a broad variety of applications, including cell-nanoparticle interactions and detection of small time-dependent changes in cells prompted by external stimuli or as a consequence of drug uptake [84, 144, 157, 158].

To minimize the consequences of protein corona formation, specifically hindering active SERS sites, solid SERS substrates can be used, since they already include pre-formed hot spots, unlike colloidal nanoparticles that need to aggregate [159]. Technically, introducing

nanoparticles into the cell interior is invasive, as opposed to solid substrates used as *in vitro* sensing platforms on which cells are deposited. Naturally, SERS signals obtained from such substrates will only be observed for molecules at the outer cell membrane attached directly to the SERS substrate surface. Such substrates should therefore be relatively flat to ensure proper cell attachment in the close vicinity to the hot spots, which are usually located close to the surface of the dielectric SERS substrate support (e.g., glass, silicon). Moreover, to improve the affinity of the cellular molecules to the metal surface, cells should be exposed to the SERS substrate for a prolonged time, ideally for the whole duration of the cellular process monitoring, e.g., cell apoptosis or differentiation, but such an approach is still not widely used. Nanostructured surfaces have been used previously in cell membrane studies [160, 161]. Moreover, Caprettini et al. [161] reported on intracellular measurements and cell membrane dynamics with the use of 3D plasmonic nanoelectrode arrays. The intracellular measurements, however, were obtained with the use of electroporation, which in fact can drastically influence the cell behavior and consequently affect the SERS measurements, which is then far from being reflective of the cell behavior in its natural environment. In a sense, these elongated plasmonic nanostructures are also intrusive, although to a lesser extent than internalized colloidal particles.

Direct SERS analysis presents unique advantages, by providing molecular fingerprint information for both identification and detection without further labeling [30, 144, 159]. Moreover, the observed spectrum can reveal information on conformation and orientation on molecules adsorbed on nanoparticle substrate. Therefore, the SERS spectrum may differ from its Raman counterpart. Consequently, it is challenging to obtain reproducible and reliable results to build a database of SERS spectra, especially considering that many biomolecules have similar spectral fingerprints, causing multiple scattered signals to overlap. In addition, the effect of “blinking” is often observed, i.e., the fluctuation in intensity or even disappearance of Raman bands, as the molecules can diffuse in and out of the hot spots [44]. Despite the advantage of SERS being able to obtain a great wealth of information, even on a single-molecule level, the resulting spectra are extremely complex and the process of extracting meaningful data from the abundant spectral information often presents a Sisyphean task.

Several ways to tackle the wealth of SERS spectral information in biological studies have been developed. One example is the case of the “indirect SERS” method, where nanoparticles or nanostructured surfaces are labeled by SERS tags with ligands, as described above [4, 85, 144, 162]. SERS signals are therefore generated when the ligands bind to target molecules. Consequently, SERS tags can be compared to the labels used in fluorescence-based detection methods [84] and the approach can therefore no longer be considered label-free. Another way is to synergize multivariate analysis with SERS data. Principal component analysis (PCA) is frequently used for purposes of identification and classification of cells, e.g., for discrimination between viable and dead cancer cells after drug treatment [84, 163]. Often the combination of PCA with the linear discriminant analysis (LDA) is used for improved differentiation between different cellular species [164, 165]. In addition, machine learning approaches such as random forest analysis have proven to be useful in analysis of SERS data that exhibit higher complexity [166]. One way to mitigate the wealth of SERS data is to limit the area of analysis to the parts of the cell adjacent to the SERS substrate, instead of introducing metallic nanoparticles to the cell interior. In that way, the SERS signal will be obtained specifically from the part of the cell that is in nm-proximity to the substrate. This allows, for example, for discrimination between healthy and unhealthy cells, as well as

for monitoring cellular differentiation by detecting changes at the cell membrane and the surrounding environment, i.e., cell niche.

Ultimately, the choice of the appropriate method and suitable SERS substrate will depend on the application. In this thesis, the aim was to develop and characterize SERS substrates suitable for following the cellular differentiation process by monitoring changes occurring on the outer membrane of mesenchymal stromal cells undergoing osteogenesis. In such a process, the mineralization of freshly deposited extracellular matrix takes place at the interface between the metallic surface of the SERS substrate and the cell membrane, in the so-called "cell-niche". Hence, a relatively flat surface had to be developed to allow for proper attachment of the cells. Mesenchymal stromal cells, as will be described below, are primary cells that can be difficult to maintain in the environment previously unknown to them, therefore it is important to provide them with as non-disruptive conditions as possible. The osteogenic differentiation process has been studied previously by SERS [167-169] and even more extensively by Raman [49, 50, 170-172], yet the process of osteogenesis of heterogeneous populations of mesenchymal stromal cells is far from being completely understood. This project, specifically, aims to yield increased knowledge in the matter.

2.4 Mesenchymal stromal cells

2.4.1 Definition

The concept of mesenchymal stem cells, initially discovered by Friedenstein et al. [173, 174], followed by work of Owen and others [175], dates back to 1991 when Caplan described the isolation of such cells from bone marrow niche [176]. Friedenstein et al. demonstrated that mouse bone marrow contains colonogenic progenitor cells (colony forming unit-fibroblast – CFU-F) that can give rise in culture to fibroblasts, as well as other mesodermal cells. He observed that these cells do not have the hematopoietic origin, but instead can give rise to bone and cartilage-precursor cells. Together, these and further investigations showed that cells found in the stroma of bone marrow could differentiate into bone, cartilage, and adipose tissue types. Since then, stem cells were isolated from various sources (umbilical cord, placenta, dental pulps, adipose tissue etc.) and there were numerous reports on diverse types of tissues that these cells can differentiate into (bone cells, epithelial cells, nervous cells, blood cells, cardiac cells, fat cells, muscle cells, etc.) [177-180]. The terms used to describe these cells were ranging from, initially, precursors for fibroblasts and osteogenic stem cells, through marrow stromal stem cells, multipotent mesenchymal stromal cells to the most widely used term mesenchymal stem cells [181]. Inconsistencies had arisen as separate lab groups were using different cell-surface markers to characterize MSCs. Moreover, it has become clear that reported MSCs are not homogenous cell populations, they lack the "stemness" activity and vary in their potential to give rise to other cells from different tissue sources [36, 180]. Proper stem cells must have unlimited self-renewal abilities to produce the same progeny as mother cell and must be able to give rise to a specialized cell type of the body what is often referred to as an asymmetric cell division [182]. Therefore, the International Society for Cellular Therapy (ISCT) [183, 184] proposed a new term for cells located in the stroma of resident tissue to be "multipotent mesenchymal stromal cells" or simply "mesenchymal stromal cells". In this thesis, the "mesenchymal stromal cells" term was accordingly adopted.

2.4.2 Characterization

In 2006, the ISCT published a set of minimal criteria for defining MSC [183]. The cells should be plastic adherent, when cultured *in vitro*, be able to differentiate into osteoblasts, chondrocytes, and adipocytes *in vitro* and express certain surface antigens CD73, CD90, and CD105, while lacking expression of CD45, CD34, CD14 or CD11b, CD79α or CD19 and HLA-DR. However, the list of surface antigens is being periodically updated. MSCs have been isolated not only from bone marrow, but also adipose tissue, umbilical cord, amniotic fluid, placenta, skin, dental pulps, etc., as reviewed in more detail along with isolation methods, clinical potential, and proliferation capacity by Berebichez-Fridman et al. [185]. MSCs have been identified as heterogenous populations of cells that differ in their morphology from spindle-shaped cells, through large cuboidal cells to small round cells, as described by Pevsner-Fischer et al. [186]. This is due to the fact that single-cell-derived colonies contain at least two kinds of cells, in which we can find the rightful stem cells as well as cells originating from stroma, that vary greatly in their differentiation potential. Thus, the minimal definition imposed by ISCT is far from being definitive. Unfortunately, heterogeneity of cells is usually neglected in individual research studies and lack of consensus on characterization parameters makes comparing studies between different laboratories essentially difficult.

2.4.3 Heterogeneity

MSC heterogeneity certainly has a huge impact on the quality of research. In order to demonstrate the applicability of a particular study using MSCs, researchers usually need to provide evidence of “comparability”, i.e., use several donors and replicates within the same cell passage.

The origins of heterogeneity are broad and arise on multiple levels (Figure 2.8). Different tissue sources are the main reason for multiplicity of MSC cells. Multiple studies showed disparities in proliferation and differentiation potential, especially in terms of lineage preference and full tri-lineage differentiation capacities into connective tissue subtypes [187-190]. For example, it has been demonstrated that umbilical-cord-derived MSCs can be expanded in culture and are able to differentiate into multiple lineages, however, they appear to be slower to establish in cell culture and express lower level of bone antigens, as compared to bone marrow-derived MSCs [188]. Dissimilarities in MSCs originate also from different donor sources. Donor-to-donor variations have different roots, including donor age, donor health or environment, which all influence the self-renewal capacity and differentiation potential of the cells [191]. Diversities in MSCs population are also arising from differences in non-standardized isolation and cryopreservation methods, as well as cell culturing techniques and media components. Consequently, inter-clonal variations are observed, and many studies reported reduced proliferation and differentiation abilities of MSCs with increasing number of passages and time in culture [36].

Moreover, cell variations have been identified within individual MSC clones. The majority of research is conducted in conventional cell culture flasks and plastic wells, however, even a slight change in the microenvironment of the cultured cells, which are usually maintained at 95% humidity and controlled 5% CO_2 flow at the temperature of 37°C, can alter the homeostasis and determine a different cell fate. Furthermore, these *in vitro* cell culturing conditions are far from *in vivo* MSC environment, lacking the complexity of the stem cell

niche composition, influence of mechanical forces and interaction with other tissue types. All these intrinsic and extrinsic factors have a major effect on the cellular behavior and the heterogeneity of MSC populations. Together, it shows that our knowledge about MSCs and the impact of different environmental signals on them, is still in its infancy.

In evaluation of proliferation and differentiation potential of mesenchymal stromal cells, researchers mostly rely on assays and procedures that treat the cell population as a whole, whereas it is also hugely important to examine heterogeneous populations at the single-cell level and such methods are still in short supply.

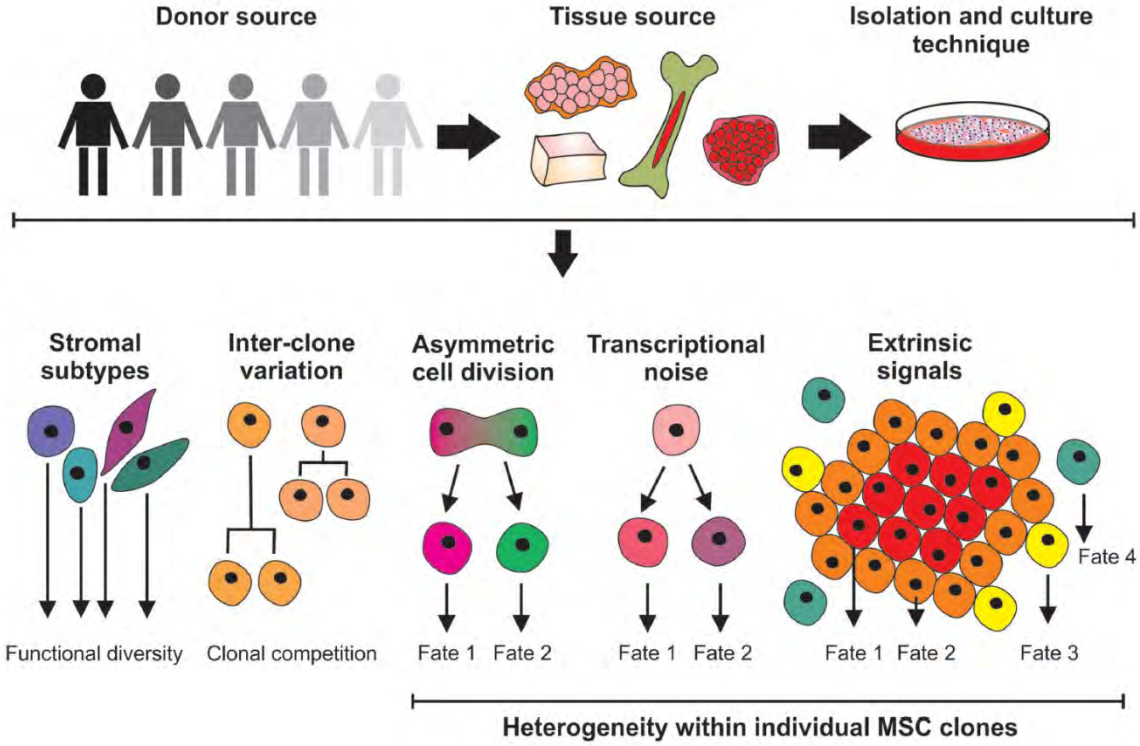

Figure 2.8 Sources of mesenchymal stromal cell heterogeneity. MSCs can vary significantly between donors, different tissue sources and isolation/culturing techniques. Differences within MSCs can also arise from different stromal subtypes and inter-clonal variations, resulting in heterogeneity within individual MSC clones. Adapted from [36].

2.4.4 MSC niche and cell adhesion

Stem cells reside in a specific microenvironment, denoted as “niche”, which dynamically regulates stem cell behavior, where they live in a quiescent stage, but can also self-renew and differentiate in controlled manner [192]. Niches are highly specialized for each specific type of stem cell, depending on location in the body. They are comprised of the stem cells themselves and by supportive stromal cells, together with extracellular matrix (ECM), in which they reside [193]. Stem cells have the ability to seed themselves in the niche, which is essential to maintain the stem cell pool for long-term self-renewal. The concept of the niche in bone marrow was first described by Schofield in 1978 and to this date it serves as the most well-understood example of such physiologically limited microenvironment in which stem cells live in [194, 195].

The ECM plays a key role in the stem cell niche providing controlled mechanical, biochemical, physical, structural properties and therefore regulating cell behavior [193]. ECM is a complex, three-dimensional network of various macromolecules and biochemical components, such as fibrillar proteins (collagen), proteoglycans (fibronectin), polysaccharides and growth factors, however, its composition is tissue-specific (reviewed in more detail by Gattazzo et al. [193]). ECM-stem cell communication is mediated by integrins, as demonstrated by several studies [193, 196, 197], which are also essential in the cell adhesion, anchorage, and homing of stem cells [195]. These transmembrane receptors are responsible for extra- and intracellular communication, thus mediating cell fate, i.e., migration, proliferation, or differentiation. In turn, stromal cells subtypes modulate the surrounding ECM by production of soluble bioactive molecules, extracellular vesicles, and extracellular matrix itself [198].

Cell adhesion is also an important determinant of stem cell behavior. The focal adhesion sites are formed by integrins, adaptors and signaling proteins that anchor cytoskeleton within the matrix. *In vitro*, during cell-ECM attachment to the underlying surface, cells undergo morphological deformation, as compared to the dynamic process of attachment *in vivo*. The process of cell adhesion *in vitro* can be described by three stages: attachment of cell body to the substrate, flattening and spreading of the cell body, and the organization of the actin skeleton with the formation of focal adhesion sites between the cell and the substrate [196]. In the final stage, cells both reach the maximum spreading area, and the adhesion becomes stronger. This is particularly important for SERS studies of cells on SERS substrates, where the probing area is the one adjacent closely to the metallic surface.

2.4.5 Osteogenic differentiation

Osteoblast lineage cells, which form bone tissue, include mesenchymal progenitors, pre-osteoblasts, osteoblasts (mature osteoblasts), bone-lining cells and osteocytes [32]. Osteoblasts and chondrocytes have the same progenitor (Figure 2.9) and their differentiation into different lineages is coordinated by a set of growth factors, cytokines and the expression of lineage-specific transcription factors [199]. Bones that form the skeleton in the body can be generated by either of two processes: intramembranous, which does not include a cartilage intermediate stage and is restricted to skull and clavicle bones, or endochondral ossification, which produces osteoblasts that form the rest of the skeleton [32]. During endochondral ossification, mesenchymal progenitors form chondrocytes, which are later degraded by blood vessels what triggers initial osteoblasts differentiation. After initial commitment, the process of osteogenesis can be divided into three phases: in the first phase, the cells proliferate, express several osteogenic markers, and secrete collagen type I [200]. Next, they exit the cell cycle and start the differentiation process, while maturating the extracellular matrix with alkaline phosphatase (ALP) and collagen [201]. This newly deposited matrix rich in collagen type I, not yet mineralized, is also known as osteoid [31]. In stage three, osteoid undergoes mineralization, a process of accumulation of calcium phosphate in the form of hydroxyapatite. Therefore, the three levels of osteogenesis can be distinguished, from commitment to terminal differentiation, which are: mesenchymal progenitors, osteoblast precursors and mature osteoblasts, that while being embedded within bone matrix, become osteocytes. The cells also change their appearance from spindle-shape morphology to more cuboidal shape in active osteoblasts.

In vitro, osteogenic differentiation can be induced by a cocktail of specific chemical factors, which play a key role in osteogenic differentiation and are vital components of the cell culture media. They include dexamethasone, β-glycerophosphate (BGP), ascorbic acid and bone morphogenetic protein BMP2. Dexamethasone up-regulates expression of an early marker of osteogenesis – alkaline phosphatase (ALP) – and initiates cell shape changes during differentiation [202, 203]. Ascorbic acid 2-phosphate, derived from vitamin C, is responsible for induction of collagen type I biosynthesis, constituting the basis for calcified extracellular matrix deposition, increases proliferation and promotes matrix mineralization [204]. β-glycerophosphate acts as a substrate for ALP, providing essential phosphate ions for the deposition of hydroxyapatite during the mineralization phase of ECM [192]. Moreover, recent studies have shown that BMP2 proteins act as enhancers of osteogenic differentiation, inducing upregulation of transcription factors, such as RUNX2, OCP and OCN, necessary to bone formation [205].

Mature osteoblasts express a unique combination of extracellular proteins, i.e., collagen type I, alkaline phosphatase, osteopontin (OCP), osteocalcin (OCN) and bone sialoprotein, which are dependent on the regulation by transcription factors. Collagen type I is expressed from the initial stage of osteogenic differentiation and until the end remains the abundant component of the bone matrix [206]. Osteopontin is a non-collagenous protein that is expressed by immature osteoblasts and along with ALP helps to stabilize the matrix. In the late stage of differentiation, osteocalcin is expressed and plays important role in the regulation of ECM mineralization [206].

Runt-related transcription factor 2 (RUNX2) is the master regulator of osteogenic differentiation and is expressed in osteochondroprogenitors, that are not fully committed to either osteo- or chondrogenesis. RUNX2 is upregulated early in osteogenic differentiation and is expressed within the chondrogenic mesenchyme, dependent on SOX9. The role of SOX9 in osteogenic differentiation is not well understood, as it is a crucial transcription factor for chondrogenesis. However, SOX9 also marks the mesenchymal progenitors, from which all osteoblasts are derived. Following cartilage formation in endochondral ossification, RUNX2 becomes more restricted to osteoblasts and another transcription factor Osterix (OSX) is upregulated, directing osteochondroprogenitors towards osteogenic lineage (Figure 2.9). OSX plays important role also during osteoblast maturation, presumably taking part in matrix mineralization processes. Finally, activating transcription factor 4 (ATF4) is induced in mature osteoblasts and directly regulates the expression of osteocalcin and promotes efficient amino acid import to ensure proper protein synthesis by osteoblasts [32]. Although only three transcription factors have been described here, osteogenic differentiation process is controlled by several other markers, reviewed by Long, Frith and Graneli in Refs. [32, 207, 208].

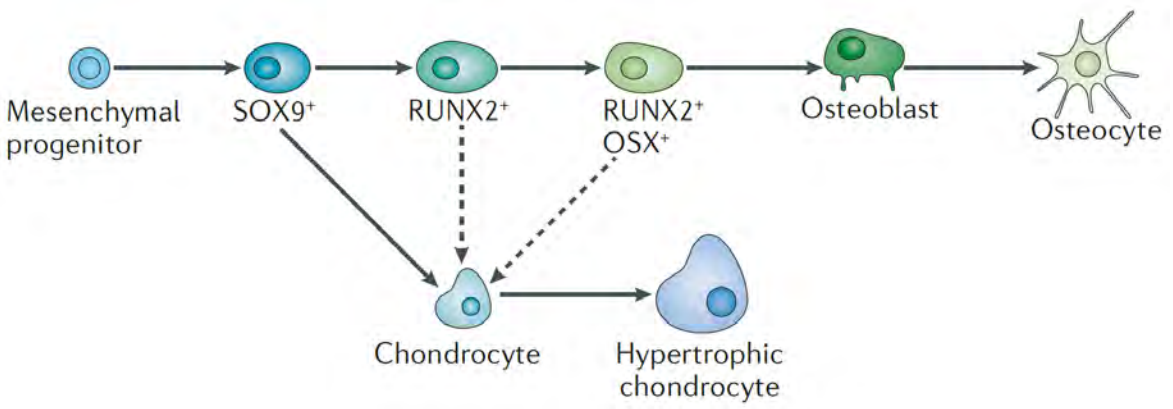

Figure 2.9 Control of mesenchymal progenitor bipotential. Differentiation is initially guided by transcription marker SOX9. Towards osteogenic differentiation RUNX2 is expressed, followed by osterix (OSX) eventually producing mature osteoblasts, that while being embedded in bone matrix, become osteocytes. Dashed arrows indicate deletion of either RUNX2 or RUNX2, OSX transcription factors causing cells to change fate and undergo chondrogenic differentiation. Adapted from [32].

Chapter 3

Aims

The overall objective of this study was to design a biocompatible platform for non-invasive and label-free detection of mesenchymal stromal cell differentiation with surface-enhanced Raman scattering and demonstrating the applicability of this platform for studying live cells.

The specific aims of the study were:

I. Design and fabrication of SERS substrate
    a) Evaluation of enhancement factors (EFs)
II. Biocompatibility studies
    a) Evaluation of proliferation
    b) Quality of differentiation
III. SERS measurements
    a) Detection of signals from parts of the cells adjacent to the substrate during proliferation
    b) SERS detection and imaging of molecular modes important during osteogenic differentiation
IV. Live-cell detection by SERS
    a) Proof-of-concept study on live-cell detection of fibroblast cell line by SERS

Chapter 4

Experimental techniques

The experimental approach used in the present study can be divided into three categories. First, gold nanoisland substrate fabrication of biocompatible platforms for surface-enhanced Raman scattering measurements, denoted as "SERS substrates" in this thesis. This fabrication step included different characterization techniques, as well as numerical simulations. Next, cell culturing of bone marrow-derived mesenchymal stromal cells (BM-MSCs) on such substrates, including evaluation of proliferation and osteogenic differentiation processes by different biological assays. Finally, Raman and SERS measurements were performed for determination of the substrates' enhancement factors and detection of molecular fingerprints of the studied cells during proliferation and osteogenic differentiation, including chemical mapping (SERS imaging) and spectral analysis. Live-cell measurements of a fibroblast cell line on the fabricated SERS substrates were also included.

4.1 SERS substrate fabrication

4.1.1 Cleanroom fabrication

The fabrication of gold nanoisland arrays on 18×18 mm cover glass supports (Marienfeld, Germany) was achieved by repeated metal deposition and post-deposition annealing, performed in a class 100 cleanroom. An electron-beam evaporator (Polyteknik Cryofox Explorer 600 LT) was evacuated to a base pressure of 6.0×10^{-5} mbar. Thin layers of 99.95% gold with thickness below the percolation threshold were deposited (corresponding to a mass-equivalent thickness of approximately 4 nm using a 0.6 Å/s deposition rate), thereby producing self-organized gold nanoparticle (AuNP) islands. The as-coated cover glasses were annealed immediately after deposition on a hot plate at 350°C (in **paper I**) or 500°C (in **paper II**) for 5 minutes, causing aggregation of smaller AuNPs into larger particles through surface diffusion, which corresponds to the phenomenon widely known as Ostwald ripening, first investigated by Wilhelm Ostwald in 1897 [209]. The ripening process occurs, because larger particles are more energetically favored than smaller particles, in certain conditions, like high temperatures, which cause interparticle coalescence, leading to the growth of NPs [210]. Subsequently, similar gold deposition and post-deposition annealing steps were repeated up to a total of three times to eventually obtain a nano-patterned gold film with a wide distribution of particle sizes. The process (both for **paper I** and **II**) is shown schematically in Figure 4.1. The resulting nanoisland film was characterized after every deposition and annealing step, as explained below.

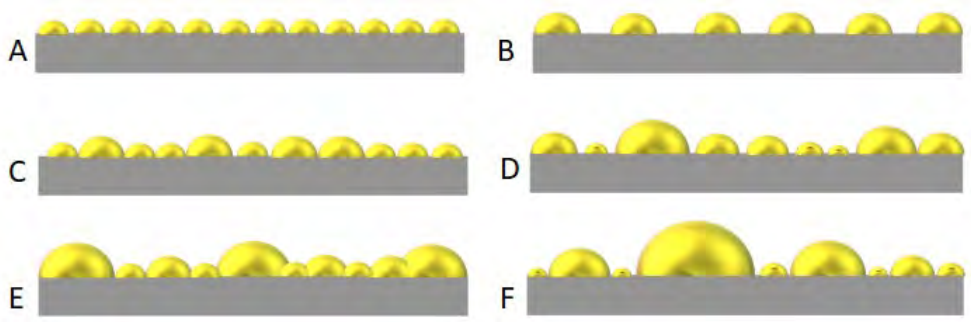

Figure 4.1 Schematic illustrations of the fabrication process involving repeated gold deposition (A, C, E) and subsequent post-deposition thermal annealing (B, D, F) resulting in nanoparticle aggregation. *Reprinted with permission from [211].*

4.1.2 Characterization of SERS substrates

Scanning Electron Microscopy

The gold film structures were characterized by a Zeiss Supra-25 scanning electron microscope (SEM) using an in-lens secondary electron detector, 20 kV acceleration voltage, 1.5 nm spatial resolution and approximately 5 mm working distance. The planar morphology of AuNPs, i.e., the surface coverage, mean diameter of gold nanoparticles and average distance between them, were obtained from the SEM images (**paper I and II**).

Atomic Force Microscopy

In addition, the surface topographies were evaluated using a XE-100 atomic force microscope (Park Systems) with a scan size of 1-2 µm in non-contact mode, using conventional silicon cantilevers (**paper II**).

FDTD (Finite-difference time-domain) simulations

3D finite-difference time-domain (3D-FDTD) simulations of field enhancement of the SERS substrates at different stages of sample fabrication were performed with Lumerical FDTD Solutions software (FDTD Solutions, Lumerical Inc., Vancouver, BC, USA) (**paper II**). For excitation, a "Plane wave" source polarized along the *x* axis was used, propagating along the negative *z* axis direction. In contrast to many published FDTD simulations performed on simplified nanostructure geometries, actual SEM images were used here to build realistic geometrical models for irregular AuNPs. The simulation mesh size was 2 nm and periodic boundary conditions were applied in the plane of the simulated structure. The frequency-dependent dielectric functions of glass and gold were taken from the literature [212], the refractive index of the glass support was set to n=1.55, and the refractive index of the surrounding dielectric was set to n=1.33, corresponding to the aqueous environment in the SERS measurements. Figure 4.2 represents an example of a setup in the FDTD software. The simulated area of the gold nanoparticle island surface deposited on a glass substrate (yellow particles on a grey box) is shown in Figure 4.2 A). The polarization and direction of the (plane wave) electromagnetic field is represented by blue and purple arrows, respectively. To calculate the SERS enhancement, the electric field intensity enhancement

at the laser (785 nm) and Stokes Raman scattering wavelengths at each point in the simulation were multiplied, that is, $\frac{|E_{loc}(\upsilon_L)|^2|E_{loc}(\upsilon_{Stokes})|^2}{|E_0(\upsilon_L)|^2|E_0(\upsilon_{Stokes})|^2}$ and for short $|E_{exc}|^2|E_{Stokes}|^2$.

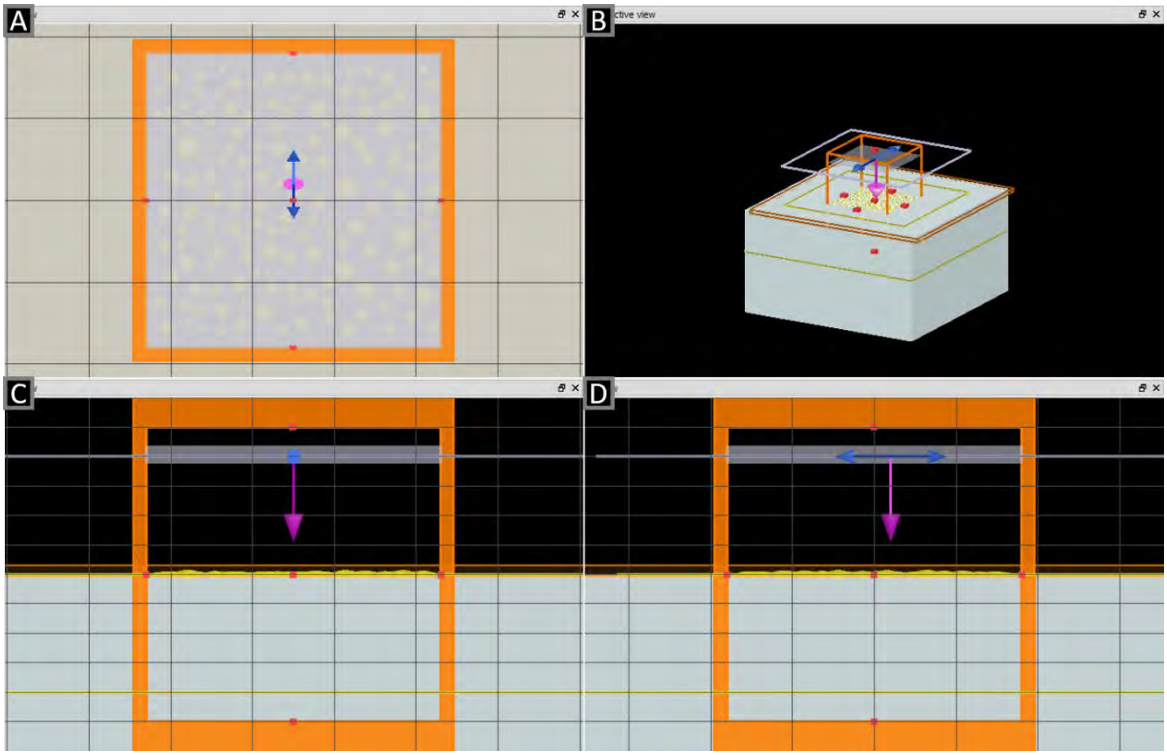

Figure 4.2 Lumerical FDTD Solutions simulation window. Glass substrate with gold nanoisland array. The purple arrow represents the direction of the source wave, the blue arrows represent the direction of polarization.

4.2 Cell culture

4.2.1 Preparation of cell suspension solution

Bone marrow-derived mesenchymal stromal cells (BM-MSCs) were obtained from Lonza (Walkersville, MD, USA) and stored at -196ºC in liquid nitrogen prior to experimentation (**paper I-III**). The cells were thawed in a 37ºC water bath and transferred into a preheated DMEM/F12+glutamax medium (Gibco, Grand Island, NY, USA) containing 1% penicillin/streptomycin (Gibco), 2 IU/ml heparin (Leo Pharma A/S, Ballerup, Denmark) supplemented with 10% human platelet lysates (hPL; Platome, Reykjavik, Iceland), referred to as "expansion medium" and centrifuged at 609×g (1750 rpm) for 5 minutes to minimize the effects of DMSO (IDT Biologika GmbH, Steinbach, Germany) preservation. DMSO is used during the storage of MSCs in liquid nitrogen to prevent cell rupture. The supernatant was discarded, and the cells were resuspended in 1 ml of preheated expansion medium before being seeded into a tissue culture flask at a density of 6000 cells/cm^2. The NuncTM EasYFlaskTM 75 cm^2 (T75) tissue culture flask (Thermo Fischer Scientific Nunc A/S, Roskilde, Denmark) was placed in a Steri-Cult CO2 Incubator, HEPA Class 100 (Thermo Scientific) with 95% humidity, 5% CO_2 and temperature at 37ºC. The cell culture medium

was replaced every 2-3 days. At 80-90% confluence, cells were gently washed with PBS (Gibco, Grand Island, NY, USA) and detached from the surface in 0.25% Trypsin-EDTA (Gibco, Grand Island, NY, USA) for 5 minutes. An equal amount of preheated expansion medium was added to neutralize the trypsin before the cells were centrifuged at 609×g (1750 rpm) for 5 minutes. After centrifugation, the supernatant was discarded, and the cell pellet was re-suspended in 1 ml of the expansion medium prior to cell counting. The cells were diluted by mixing 20 µl re-suspended cell solution, 30 µl PBS and 50 µl 0.4% Trypan Blue stain (Gibco, Grand Island, NY, USA). The cell counting solution was transferred onto a hemocytometer (BRAND GmbH & Co. KG, Wertheim, Germany) covered by a glass cover slip and counted at 50× magnification using a Leica DM IRB inverted microscope (Leica Microsystems, Wetzlar, Germany). Viable cells were distinguished from the dead cells by their lack of Trypan Blue uptake. All viable cells in 4 large squares of the hemocytometer (Figure 4.3) were counted twice using the upper and lower chambers and averaged to estimate the number of cells using Eq. (2), where the total cell count was divided by the number of squares and the average cell count multiplied by 5 (the dilution factor) and by 10.000 (the conversion factor) to estimate viable cells per ml.

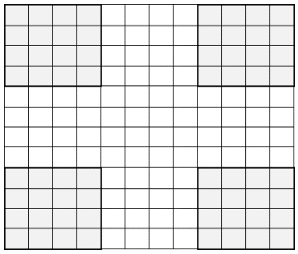

Figure 4.3 Layout of hemocytometer. The total cell count was calculated by adding the viable cell count of each grey square.

$$\frac{Viable\ cells}{ml} = \frac{Total\ cell\ count}{4} \cdot 5 \cdot 10^4 \qquad (2)$$

4.2.2 Cell culture on SERS substrates

SERS substrates, along with untreated glass controls, were placed in 2-well chamber slides (Nunc® Lab-Tek® Chamber Slide System, Thermo Fischer Scientific Nunc A/S, Roskilde, Denmark) and exposed to a high dose of UV light for 40 minutes to ensure proper sterilization. 5.500 cells/cm^2 were seeded onto the SERS/glass substrates and transferred to a shaking incubator at 37ºC for 3-4 minutes to ensure proper attachment of the cells. Subsequently, 1 ml of expansion medium was added to each well and maintained in a Steri-Cult CO2 Incubator, HEPA Class 100 (Thermo Scientific) with 95% humidity, 5% CO_2 and temperature at 37ºC. The cell culture medium was fully replaced every two to three days and the cell culture was terminated on day seven. For **paper II**, biocompatibility of the SERS substrates was evaluated by PrestoBlue viability assay, LDH cytotoxicity assay and immunofluorescence staining, as shown in Figure 4.4. For Raman measurements, SERS substrates (along with glass controls for reference) were washed 3 times with PBS, fixed for 20 minutes in 4% paraformaldehyde at room temperature, and thoroughly washed again three times with PBS prior the analysis.

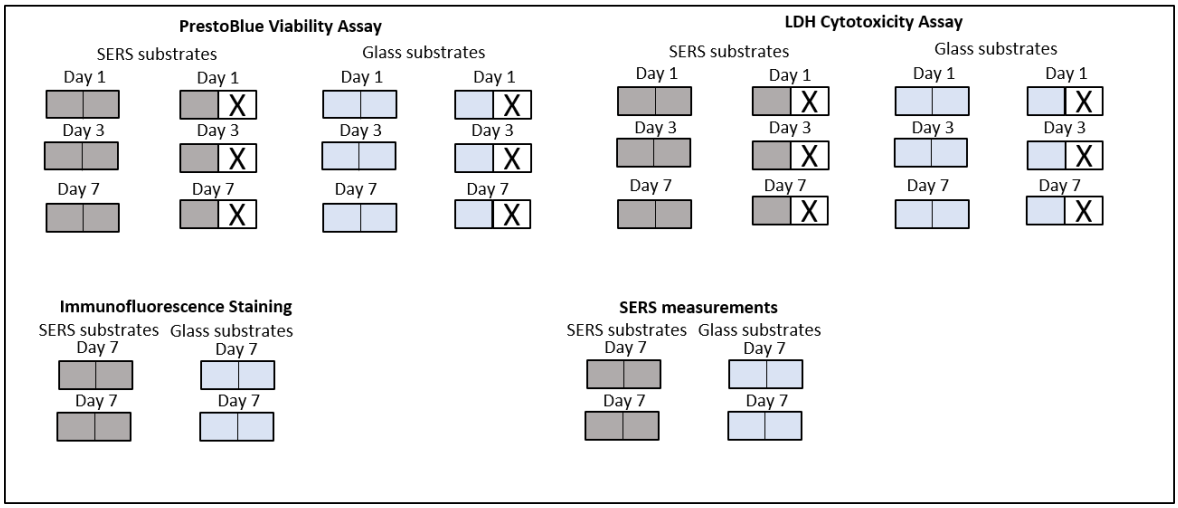

Figure 4.4 Experimental setup for cell proliferation. MSCs were seeded in 2-well chamber slides containing either a SERS substrate (grey) or a glass cover slip (blue) at a 5.500 cells/cm^2 density. Triplicates per experimental day were used for PrestoBlue and LDH assays and duplicates for immunofluorescence staining and SERS measuresments. X stands for an empty well.

4.2.3 Evaluation of cell proliferation

PrestoBlue viability assay

Cell proliferation was assessed by the PrestoBlue (PB) method (**paper II**). Briefly, MSCs on the SERS substrates and glass controls were incubated at 37ºC for 2 hours in expansion medium spiked with PrestoBlue reagent (Thermo Fisher Scientific, Frederick, MD, USA) in a 9:1 ratio. After a visually determined color change, 100 µl of medium from each well was transferred to a 96-well plate (Falcon) in triplicate and the absorbance was measured in the wavelength range 570-600 nm (Thermo Scientific Multiscan Spectrum, Thermo Fisher Scientific, Vantaa, Finland). The assay was performed on days 1, 3 and 7.

LDH cytotoxicity assay

LDH level in the culture medium of MSCs grown on SERS substrates and glass controls was assessed on days 1, 3 and 7 using a Pierce LDH Cytotoxicity Assay (Thermo Fisher Scientific, Rockford, IL 61105, USA) (**paper II**). In brief, 50 µl of each sample was transferred to a 96-well plate (Falcon) in triplicates, and 50 µl of reaction mixture was added to each well. The reaction mixture consisted of 46.5 µl substrate mix and 2.5 µl assay buffer. Serum-free DMEM medium without cells was included as control to determine LDH background activity. Water-treated cells, referred to as LDH Activity Controls and 10X Lysis Buffer-treated cells, referred to as Maximum LDH Activity Controls were included as well. Next, the plate was incubated at room temperature for 30 minutes protected from light. After incubation, 50 µl of stop solution was added to each well and the absorbance was measured at 490 nm and 680 nm (Thermo Scientific Multiscan Spectrum, Thermo Fisher Scientific, Vantaa, Finland).

Immunofluorescence staining

Prior to immunofluorescence staining (**paper II**), cells on SERS substrates were fixed with 4% paraformaldehyde for 20 minutes at room temperature and subsequently blocked with 1% bovine serum albumin - BSA (Thermo Fisher Scientific, Rockford, IL 61105, USA) in PBS for 30 minutes. Samples were incubated with primary antibody Anti-Vinculin (FAK100, Merck KGaA, Darmstadt, Germany) diluted 1:500 in blocking solution for 1 h at room temperature. Following incubation with primary antibody, samples were incubated (1 h at room temperature) with secondary antibody Goat Anti-Mouse IgG, H+L FITC (Abcam plc, Cambridge, CB2 0AX, UK) and TRITC-conjugated Phalloidin (FAK100, Merck KGaA, Darmstadt, Germany) both diluted 1:1000 in PBS. Subsequently, 4'6-Diamidino-2-phenylindole – DAPI (FAK100, Merck KGaA, Darmstadt, Germany) diluted 1:1000 in PBS was applied for 5 minutes. SERS substrates were then washed with buffer solution and mounted on glass slides using SlowFade™ Gold Antifade Mountant with DAPI (Thermo Fisher Scientific, Rockford, IL 61105, USA). Between all the above-mentioned steps in the sample processing, the SERS substrates with the cells were washed with 0.1% Triton X-100 (Sigma-Aldrich, St. Louis, MO, USA) in PBS washing buffer. Control samples on conventional culture slides were stained in the same manner. Immunofluorescence was visualized and captured using an Olympus FV1200 (Olympus, Tokyo, Japan) confocal laser scanning microscope. Image panels were constructed using Image-J software (NIH, Bethesda, MD, USA).

4.2.4 Osteogenic differentiation on SERS substrates

Osteogenesis was evaluated at predefined timepoints during 28 days of stimulation in osteogenic medium (**paper III**). The osteogenic medium at pH 7.4 consisted of 45 ml DMEM/F12 + glutamax (Gibco, Grand Island, NY, USA) containing 1% penicillin/streptomycin (Gibco, Grand Island, NY, USA), 2 IU/ml heparin (Leo Pharma A/S, Ballerup, Denmark), 5 ml 10% human platelet lysates (hPL; Platome, Reykjavik, Iceland), 50 µl dexamethasone (Sigma-Aldrich), 50 µl human/murine/rat BMP-2 10 ng/ml (Peprotech, Rocky Hill, NJ, USA), 50 µl L-ascorbic acid (Sigma-Aldrich) and 108 mg β-glycerophosphate disodium salt hydrate (Sigma-Aldrich). In brief, SERS substrates, along with glass controls, were placed in 2-well chamber slides (Nunc® Lab-Tek® Chamber Slide System, Thermo Fischer Scientific Nunc A/S, Roskilde, Denmark) and exposed to a high dose of UV light for 40 minutes to ensure proper sterilization. The cells were seeded onto the substrates at a density of 5.500 cells/cm^2. The substrates were transferred to a shaking incubator at 37ºC for 4 minutes to ensure proper attachment of the cells. Subsequently, 1 ml of expansion medium was added to each well. The cells were placed in a Steri-Cult CO2 Incubator, HEPA Class 100 (Thermo Scientific) incubator and maintained at 37ºC and 95% relative humidity with 5% CO_2. The cell culture medium was fully replaced on the second day. On day 3 the expansion medium was switched to the osteogenic medium. The control samples were included by seeding 5.500 cells/cm^2 on glass plates as well as on SERS substrates in expansion media in absence of osteogenic stimulation. Cell culture media were replaced every two to three days to replenish nutrients and maintain stable pH. The experimental setup is shown in Figure 4.5. For Raman measurements, SERS substrates were washed 3 times with PBS, fixed for 20 minutes in 4% paraformaldehyde at room temperature, and thoroughly washed again three times with PBS prior the analysis. Osteogenic differentiation was performed for two independent MSC donors in two independent experiments.

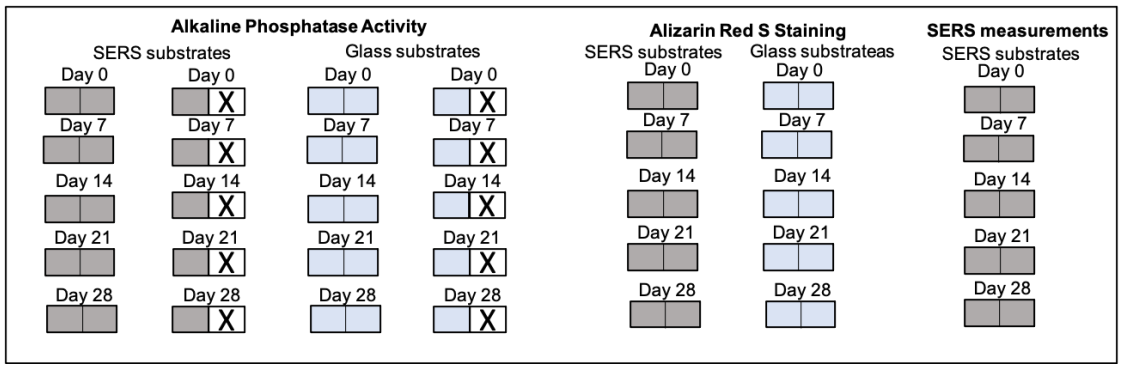

Figure 4.5 Experimental setup for osteogenic differentiation. MSCs were seeded in 2-well chamber slides containing either SERS substrate (grey) or glass cover slip (blue) at a 5.500 cells/cm^2 density. Triplicates per experimental day were used for ALP assay and duplicates for Alizarin Red S staining and SERS measuresments. X stands for an empty well.

4.2.5 Assessment of osteogenic differentiation

Alkaline Phosphatase (ALP) activity

The status of osteogenic differentiation was determined after 7, 14, 21 and 28 days by ALP assay via the conversion of p-nitrophenol phosphate to p-nitrophenyl (**paper III**). Undifferentiated cells at 7 days in expansion media were included as controls (marked as day 0). Triton-X (0.02%, Sigma-Aldrich) diluted in PBS (Gibco, Grand Island, NY, USA) was added to all samples and the cells were scraped off the surface and transferred to an Eppendorf tube. The cells were vortexed and centrifuged at 13.200 ×g for 15 minutes at 4ºC. A pNPP solution consisting of one tablet of SIGMA FAST™ pNPP and SIGMA FAST™ Tris Buffer (Sigma-Aldrich, Missouri, SL, USA) was prepared. After centrifugation, the supernatant was transferred to a new microtube and mixed with pNPP solution. Next, the solution was incubated for 30 minutes at 37ºC in the dark. After incubation, 300 µl of each sample was transferred to a 96-well plate (Falcon) in triplicates and the absorbance was measured at 400 nm in spectrophotometer (Thermo Scientific Multiscan Spectrum, Thermo Fisher Scientific, Vantaa, Finland). The average of three blank replicates was subtracted from each sample. Alkaline phosphatase activity was calculated as shown in Eq. (3):

$$\text{nmol}\left(\frac{\text{p}-\text{nitrophenol}}{min}\right) = \frac{\frac{OD}{18.8}}{\text{Time(min)}} * 1000 \qquad (3)$$

where the optical density (OD) at 400 nm divided by 18.8 - the extinction coefficient of p-nitrophenol (µmol^{-1}) was divided by the time of incubation and the result multiplied by 1000 to convert the µmol to nmol.

Alizarin Red S staining

Alizarin Red S staining was performed to visualize mineralization during osteogenic differentiation (**paper III**). The cells on the SERS substrates and glass cover slips were washed three times with PBS and fixed in 4% paraformaldehyde after 7, 14, 21, and 28 days and stored at 4ºC before the staining procedure. Undifferentiated cells at 7 days in expansion media were included as controls (marked as day 0). The cells were washed three times with DI water and stained with 2% Alizarin Red S dye (Sigma Aldrich Inc., St. Louis, MO, USA)

diluted in DI water at pH 4.1. The cells were placed on a rotating shaker and stained for 20 minutes at room temperature followed by four washing steps using DI water. The dye was allowed to dry for 24 hours and pictures were taken using an inverted microscope (Leica DM IRB) with Infinity Capture 5.0.2 software.

4.3 Raman measurements

4.3.1 Estimation of Enhancement Factors (EFs)

In **paper II**, normal Raman and SERS spectra were recorded over a spectral range of 300 cm^{-1} to 1900 cm^{-1} using a single-stage spectrograph (Horiba, Munich, Germany) with a CCD detector and a 60× water-immersion objective (Olympus, Hamburg, Germany). For excitation, a diode laser (Toptica, Munich, Germany) operating at 785 nm was used (1 µm laser spot size). In order to estimate the SERS enhancement factor (EF) of the substrates, Raman signals from crystal violet (CV) were collected, with and without SERS enhancement. The excitation intensity on the sample was 2.0×10^5 W/cm^2 and an acquisition time of 1 s per spectrum was used. The CV concentration was 1×10^{-4} M in the SERS experiments while in the normal Raman experiments the CV concentration was 1×10^{-2} M. Both were performed in aqueous solution. All spectra were frequency-calibrated using a spectrum of a toluene-acetonitrile mixture (1:1).

SERS enhancement factors were estimated by comparing intensities in the normal Raman spectrum (I_{RS}) and in the SERS spectrum (I_{SERS}) for the band at 1618 cm^{-1} of crystal violet, taking into account the number of molecules in the focus volume (N_{RS}) versus the number of molecules on the nanoparticle surface (N_{SERS}), assuming a surface area per CV molecule of 4 nm^2 [213]:

$$EF = \frac{I_{SERS} N_{RS}}{I_{RS} N_{SERS}} \tag{4}$$

where $I_{RS/SERS}$ is the intensity of the specific band in normal Raman or SERS spectrum, respectively, and $N_{RS/SERS}$ is the number of molecules in the focus volume in the absence or presence of the nanosurface, respectively.

4.3.2 SERS experiments

SERS spectra of MSCs cultured on SERS substrates (**paper I**) were recorded over a spectral range of 100 cm^{-1} to 1800 cm^{-1} with a WITec Alpha 300R+ microscope using a 50× long working distance objective and a diode laser operating at 785 nm. SERS spectra of MSCs (**paper II**) were recorded over a spectral range of 300 cm^{-1} to 1900 cm^{-1} using a single-stage spectrograph (Horiba, Munich, Germany) with a CCD detector and a 60× water-immersion objective (Olympus, Hamburg, Germany). For excitation, a diode laser (Toptica, Munich, Germany) operating at 785 nm was used (1 µm laser spot size). Typical spectra in the SERS experiment on cells were collected using intensity on the sample of 2.0×10^5 W/cm^2, with a raster size of 2 µm and an acquisition time of 3 s per spectrum. All spectra were frequency-calibrated using a spectrum of a toluene-acetonitrile mixture (1:1).

SERS spectra of live 3T3 fibroblast cells (**paper IV**) were obtained over the same spectral range as described above, with 785 nm laser and the excitation intensity of 1.0×10^5 W/cm^2 at a step size of 2 µm, with an acquisition time of 1 s per spectrum. SERS maps and spectra of osteogenic differentiation (**paper III**) were recorded over a spectral range of 300 cm^{-1} to 1800 cm^{-1} with Horiba LabRAM Evolution microscope using a 60× water-immersion objective and a diode laser operating at 785 nm (excitation spot size 1 µm). The excitation intensity on the sample of 6.0×10^5 W/cm^2 and an acquisition time of 3 s per spectrum was used. The microscope was calibrated prior the experiments using the silicon (Si) Raman scattering peak at 520 cm^{-1}.

4.4 Data processing and analysis

SERS spectral analyses, including elimination of cosmic spikes and background subtraction, were performed using LabSpec 6.0 software. For chemical mapping, intensities were determined from the original spectral datasets after baseline correction. Pre-processed normal Raman and SERS spectra were analyzed using OriginPro 2019 software, MatLab (The MathWorks, Inc.), WITec Suite FIVE (WITec Wissenschaftliche Instrumente und Technologie GmbH) and CytoSpec 2.00.06 software (CytoSpec, Inc.). Statistical analysis was performed using GraphPad Prism 6.0 software. Image panels were constructed using ImageJ v1.52a software.

Chapter 5

Results and Discussion

This thesis is composed of four published papers (**Paper I, Paper II, Paper III and Paper IV**) and unpublished data. In all the papers, SERS substrates are used to study molecular fingerprints of cellular membrane of either BM-MSCs (**Papers I-III**) or live fibroblast cells and membrane models (**Paper IV**). In this chapter, the main results from each paper are summarized and discussed, including some unpublished data.

In **Paper I**, the SERS substrate fabrication method is presented and the challenges of managing gold atoms on dielectric surfaces to realize the structural features of interest are discussed. **Paper II** concentrates on thorough characterization and numerical simulation of the SERS substrates, including evaluation of enhancement factors during different steps of preparation, as well as their applicability as *in vitro* sensing platforms for SERS detection of cellular fingerprints. **Paper III** demonstrates that long term cell proliferation on SERS substrates is not compromised and osteogenic differentiation of BM-MSCs on the substrates is discussed, using chemical mapping and analysis of SERS spectra for revealing signs of differentiation. **Paper IV** demonstrates that live cell studies of 3T3 fibroblast cell line on the fabricated SERS substrates are feasible, confirming also that the measurement conditions do not adversely affect live cells. Unpublished findings include SERS substrate fabrication details, fluorescence microscopy of cells cultured on SERS substrates and SERS data from different days of osteogenic differentiation.

5.1 Gold nanoisland arrays on glass supports as SERS substrates

In order to obtain a relatively flat nanosurface with sufficient density and uniform distribution of hot spots, repeated evaporation of thin gold films and subsequent thermal annealing was performed, as described in the previous chapter. The high surface mobility of gold was thus harnessed to reduce the interparticle spacings between nanoislands down to length scales that are difficult to obtain reproducibly and over large areas with conventional lithographic techniques. Although this method leads to uncontrolled coalescence of gold particles and yields somewhat smaller enhancement factors than specially engineered pre-patterned structures, it is, however, notably simpler and can be readily used to cover arbitrarily large substrates. This is particularly important in cell studies, where high density of hot spots across large areas is needed as cells tend to choose their place to grow randomly, not necessarily in the spots with the highest enhancement.

5.1.1 Characterization of initial gold nanoisland substrates

Nanostructured thin films were produced by successive steps of gold deposition and annealing, as previously discussed, in order to fabricate large-area SERS substrates having a wide random distribution of island sizes. In the initial step of gold deposition, a discontinuous film is formed, which upon annealing is transformed into a thin layer of nanoislands, having sizes around 10 nm on average, separated by substantial gaps (Figure 5.1 A, B step 1). After an additional step of deposition and annealing, smaller islands were eventually consumed by bigger islands, thereby producing wider distribution of island sizes (ranging from 5 to 30 nm, Figure 5.1 C step 2), simultaneously reducing the interparticle spacing. Ultimately, after a third step of consecutive gold deposition and annealing, a wide random distribution of islands sizes was obtained, ranging from 5 nm to 40 nm, with an increased occurrence of gaps between the nanoislands smaller than 10 nm (Figure 5.1 A, B, C step 3).

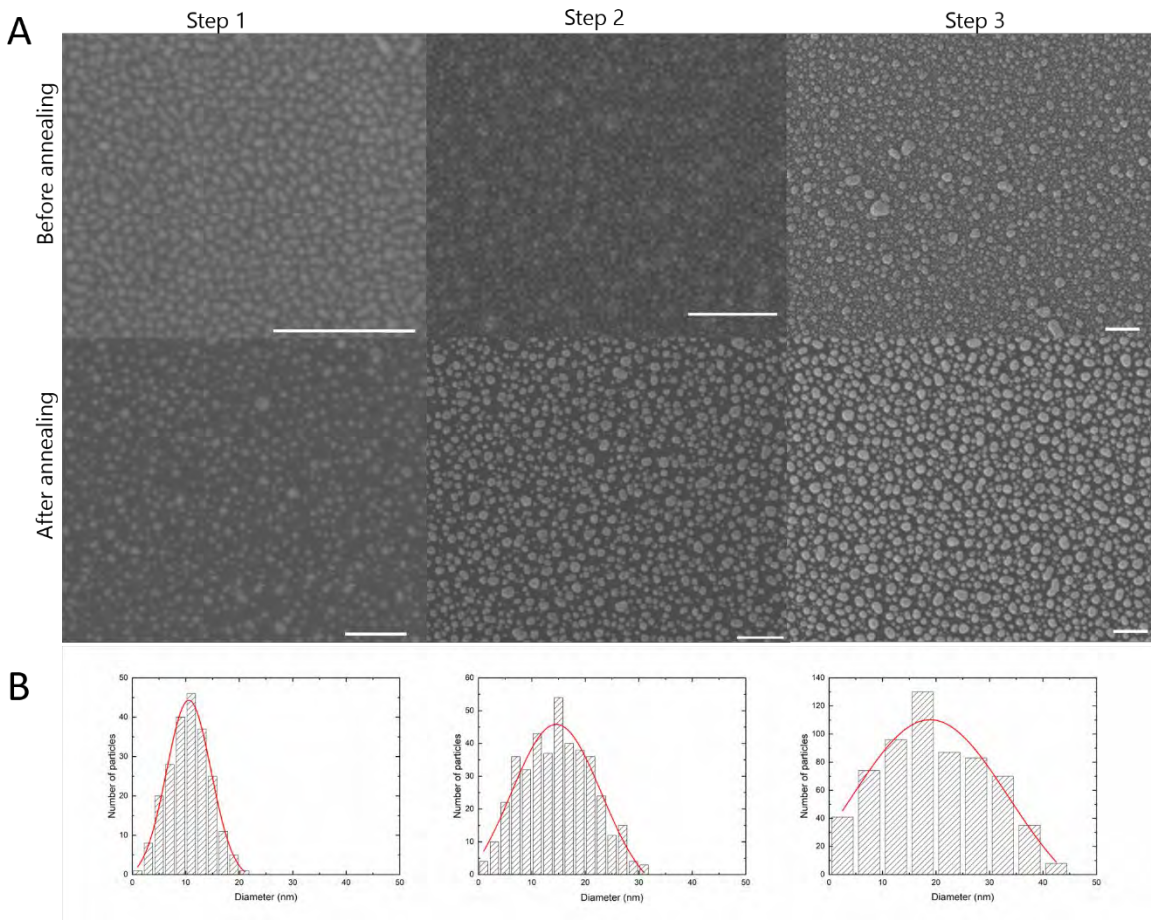

Figure 5.1 Characterization of the SERS substrates. A) Scanning electron microscopy images of self-organized gold islands fabricated by succesive deposition and annealing of ultra-thin gold layers. Upper images show the surface after the 1st, 2nd and 3rd gold deposition and the lower images show the corresponding surfaces after thermal annealing. All scale bars represent 100 nm. B) Particle size distributions corresponding to each step of sample fabrication after annealing (unpublished data).

As demonstrated, the method of repeated thin gold film deposition, followed by thermal annealing is able to achieve small interparticle spacing, widely known to be the main regions of increased local electric fields generating high plasmonic enhancement [134, 214]. To determine the most suitable laser wavelength for SERS measurements for the particular island film geometry obtained, finite-difference time-domain (FDTD) simulations were performed on hemispherical island structures having the same placement and size distribution as the actual structures, thus also taking into account the variation in island height (using data for the gold dielectric function from Olmon et al. [215]). While there is not an exact correspondence between the real and the simulated structures, due to limitations of the simulation software and the imaging techniques, such simulations still provide some insight into the development of the pattern of field enhancement after the different processing steps and potential location of hotspots at different wavelengths. The averaged wavelength-dependent field enhancement in the plane of the nanostructure, derived from FDTD simulations for each step of fabrication, is shown in the plot on Figure 5.2. The simulation results suggest that the highest maximum local field enhancement is obtained for the wavelength around 630 nm for the fabricated substrate, although there is also an increase around 800 nm wavelength. This enhancement corresponds well to the laser wavelengths 632.8 nm and 785 nm commonly used in Raman spectroscopy. Substrates fabricated in this fashion were used for initial cell culturing studies and SERS detection, as described in Chapters 5.3.1 and Chapter 5.5.1. For later experiments, however, the substrate fabrication method was adjusted, as described below, and the laser wavelength in the near-IR range was chosen, which is more suitable for SERS measurements of biological samples, where the fluorescence background is largely mitigated [30].

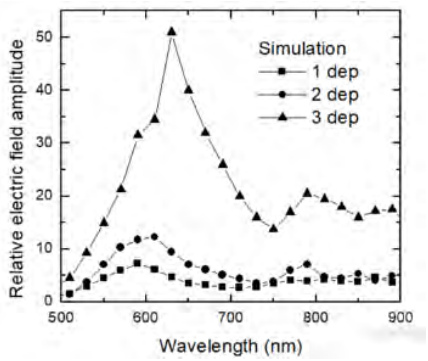

Figure 5.2 The plot shows the maximum amplitude of the local electric field between islands relative to the incident field, as determined by a numerical (FDTD) simulation of a similar structure of gold islands. *Adapted in part with permission from [216].*

5.1.2 Properties of gold nanoisland substrates

In the improved substrate fabrication protocol, the annealing temperature was increased from 350°C to 500°C, as higher temperature accelerates the particle coalescence [217]. The deposition thickness was kept unchanged (approximately 4 nm). In the first step, the ultra-thin gold film deposition gives rise to a discontinuous metal film (Figure 5.3 A). After thermal annealing, the small islands rapidly coalesce into nanoparticles with an average diameter of around 20 nm, about two times larger than in the previous case (Figure 5.1). Repeating the deposition and thermal annealing in subsequent steps resulted in a bimodal particle distribution of larger islands of diameter around 27 nm and smaller islands with diameter around 7 nm for step 2, and respectively 37 nm and 7 nm for step 3 (Figure 5.3 A,

B). Simultaneously, the average minimum distance between adjacent particles was decreasing from 15 nm for step 1 to 10 nm for step 3, and at the same time surface coverage was increasing, as shown in Table 5.1. These substrates, after three steps of deposition and annealing, resulted in substantial distribution of particle sizes, ranging from 5 nm up to 80 nm. As noted before, the size distribution of nanoislands is an important factor in determining the overall SERS enhancement [133] and along with small interparticle spacing, leads to the highest local electric field enhancements.

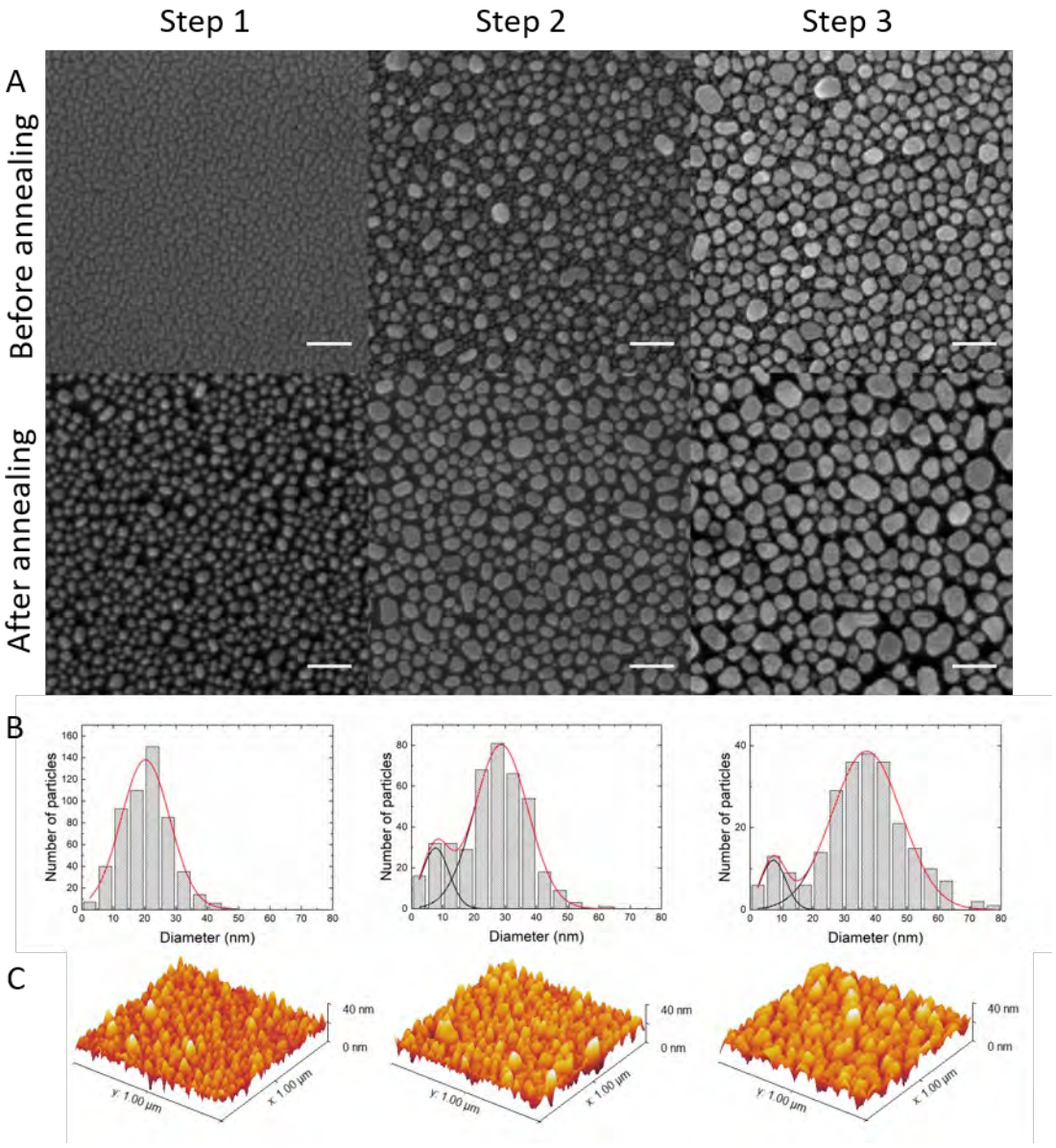

Figure 5.3 Characterization of the SERS substrates. A) Scanning electron micrographs of SERS substrates at different stages of fabrication. Upper images correspond to 1st, 2nd and 3rd gold deposition and lower images correspond to thermal annealing at 500°C. All scale bars represent 100 nm. B) Particle size distributions corresponding to each step of sample fabrication after annealing. C) AFM images corresponding to sequential steps of deposition and post-deposition annealing (step 1, 2 and 3). *Reprinted with permission from [211].*

The surface topography after each deposition and annealing step is shown in Figure 5.3 C. After each deposition and annealing cycle, the mean particle height was increasing (9 nm, 18 nm and 24 nm, respectively), correlating well with the total deposition thickness and measured surface coverage at each step. With additional gold deposition beyond step 3, the film eventually reaches the percolation threshold, decreasing the number and intensity of hotspots on the film surface, as the nanogaps between isolated islands start to diminish.

Table 5.1 *Average values of density, particle size, gap spacing and height for three steps of deposition and post-deposition annealing of the SERS substrates*

Surface parameter.	Step 1	Step 2	Step 3
Density	40%	49%	55%
Average diameter	20 nm	27 nm	37 nm
Average smallest gap	15 nm	13 nm	10 nm
Average height	9 nm	18 nm	24 nm

5.2 Enhancement factor

To understand the impact of the metallic nanostructured surface on the electromagnetic enhancement in SERS, 3D finite-difference time-domain (3D-FDTD) simulations were performed on hemispherical island structures derived from SEM images to build adequate geometrical models of the same placement and size distribution of AuNPs, as in the actual structures. Although the exact correspondence between the real and the simulated structures is not ideal, it is still more reflective of the actual substrate response than FDTD simulations that use simplified artificial nanostructure geometries. Experimental proof of increased local electric fields on the SERS substrates was obtained by measuring SERS signals of crystal violet (CV) dye molecules at different points on the substrates. The experimentally determined enhancement factors were compared to the FDTD simulations of the electromagnetic field enhancement, although it should be emphasized that the local field enhancement is not the only mechanism underlying observed SERS enhancements [218, 219], as discussed in Section 2.2 above.

5.2.1 FDTD simulation results

Results of FDTD simulation for the three steps of sample fabrication are displayed in Figure 5.4 A, corresponding to the particle size distributions shown in Figure 5.3 A, B. To estimate the approximate electromagnetic contribution to the SERS EF caused by the presence of the SERS substrates, the field enhancement in the simulations was evaluated at the excitation wavelength 785 nm (Figure 5.4 A first column) and at the Stokes-scattered wavelength 830 nm (Figure 5.4 A second column), corresponding to the band 1618 cm^{-1} of crystal violet [220]. The third column in Figure 5.4 A represents the product of the two intensity distributions which relates to the actual SERS enhancement ($|E_{exc}|^2|E_{Stokes}|^2$). The field maps are plotted for a distance of 2 nm from the glass surface. The plot in Figure 5.4 B illustrates how repeated deposition and thermal annealing results in higher maximum enhancement values that are also substantially extended from the glass surface. This is particularly important in SERS studies of cells grown on nanostructured surface, as they tend to attach to the surface in random places, at random depth, and in principle, might not attach

precisely in the “hot spot” located closest to the glass surface. Thus, uniform enhancement across the height values extended from the glass surface is a necessity. Interestingly, for the final step of SERS substrate fabrication (step 3) and for intermediate step (step 2), the maximum enhancement values are substantial not only close to the glass surface, but as well at the heights of 20-24 nm from the surface. For the final step, however, the maximum enhancement values are more evenly distributed across the whole nanosurface topography, as compared to the previous steps. FDTD simulations indicate that the order of magnitude of the field enhancement factor is fairly consistent across the typical range of emission wavelengths, varying within approximately a factor of 3–4 for Stokes shifts up to 2200 cm^{-1} for the excitation wavelength 785 nm, as shown in Figure 5.4 C. For step 3, the highest average enhancement factor is present for the smallest Raman shifts, becoming slightly lower for shifts around 1200 – 1500 cm^{-1}, where it is still, however, of the order of 10^6. The simulated maximum field enhancement factor (averaged for heights 2–40 nm and Stokes shifts 0–2200 cm^{-1}) corresponding to each deposition and annealing step is shown in Figure 5.4 D, with the maximum averaged enhancement factor for the final step of SERS substrate fabrication estimated at around $2 \cdot 10^6$. It should be noted that the full simulation area corresponds approximately to the focused spot size of the excitation laser in the SERS measurements.

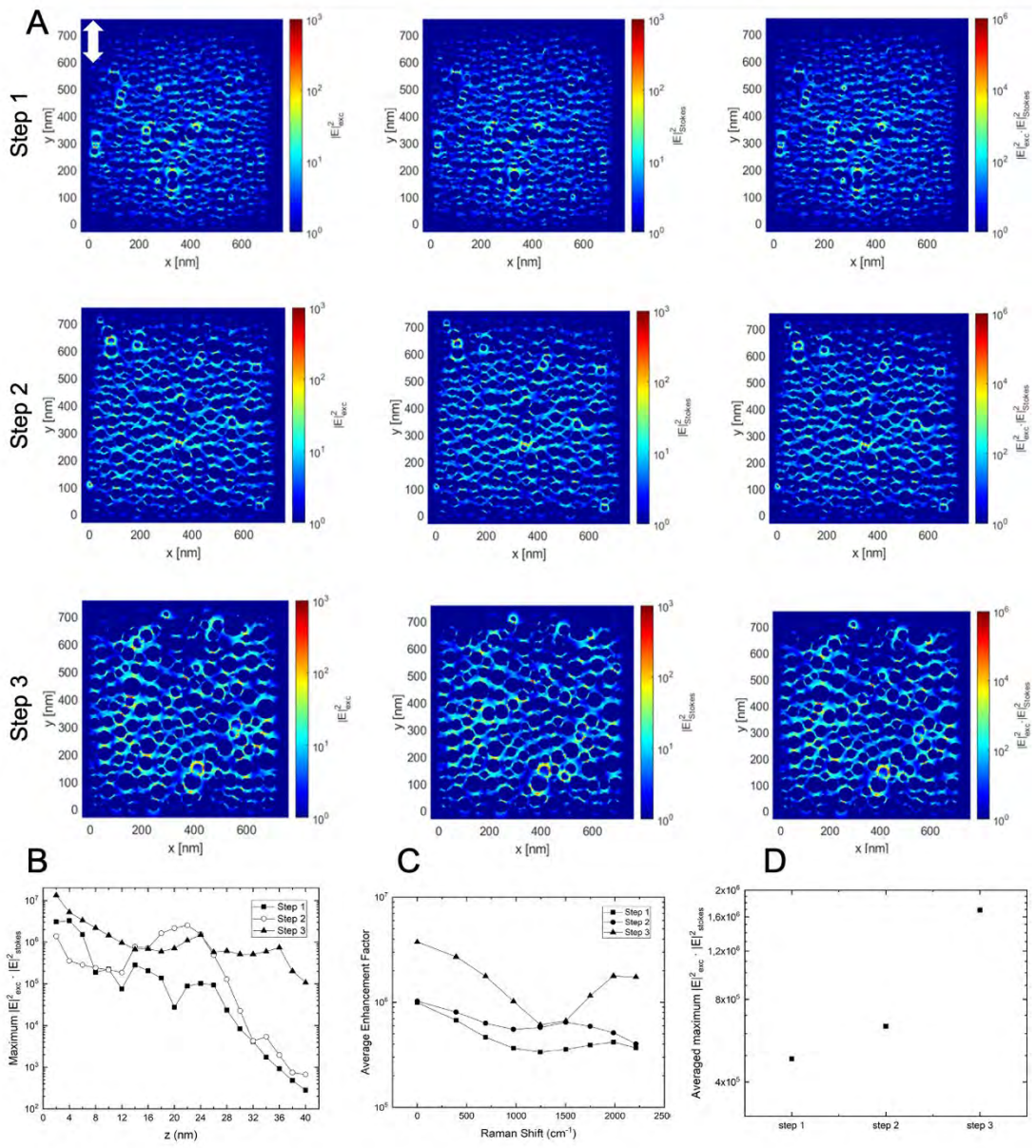

Figure 5.4 FDTD simulations of field intensity distribution in the xy-plane (plotted for a distance of 2 nm above the substrate surface). The field distribution was obtained for A) excitation wavelength at 785 nm ($|E_{exc}|^2$); Raman scattered wavelength at 830 nm ($|E_{Stokes}|^2$); and the product of the two intensity distributions which relates to the actual SERS enhancement ($|E_{exc}|^2|E_{Stokes}|^2$). The calculations were performed for structures modelled according to the gold particle geometry following steps 1, 2 and 3 of substrate fabrication (Figure 5.3 A). The direction of polarization of the incident light is indicated with the white arrow. B) Maximum product of field intensities at excitation wavelength 785 nm and Stokes wavelength 830 nm for different heights above the glass surface. C) Average enhancement factor as a function of Stokes shift for all steps of substrate fabrication excited by 785 nm laser. D) Maximum field enhancement factor obtained by FDTD simulations for sequential fabrication steps, averaged over the simulated range of heights and Stokes wavelengths. *Adapted in part with permission from [211].*

5.2.2 Experimental evaluation of EFs

Results of the experimental evaluation of the enhancement factors for three steps of substrate fabrication using crystal violet (CV) dye as analyte are displayed in Figure 5.5. SERS enhancement factors were estimated by comparing intensities in the normal Raman spectrum (I_{RS}) and in the SERS spectrum (I_{SERS}) for the band at 1618 cm^{-1} of crystal violet, taking into account the number of molecules in the focus volume (N_{RS}) versus the number of molecules on the nanoparticle surface (N_{SERS}), as specified in Eq. (4). In accordance with electromagnetic field simulations, the maximum SERS enhancement factor was observed after step 3 of substrate fabrication. In this case, 36 measurements at different points on the SERS substrate (inset of Figure 5.5 B) gave an average EF value of $9 \cdot 10^5$, exhibiting a better uniformity across the substrate than for the preceding fabrication steps, with relative standard deviation of 7% between 36 measurement points. After the first step of substrate fabrication, the average measured enhancement factor was $1 \cdot 10^4$ with relative standard deviation of 24%, while after second step the average enhancement factor was $1 \cdot 10^5$ with a standard deviation of 33% (Figure 5.4 B). These results, especially for the final step of substrate fabrication, are comparable to the results from FDTD simulations of the realistic arrangements of the nanoparticles on the glass supports ($9 \cdot 10^5$ experimental EF versus $2 \cdot 10^6$ simulation EF). For steps 1 and 2, variations are more notable, and the surfaces are less uniform. This correlates with the lower coverage of the surface with the metal, and larger interparticle spacing observed between islands at the initial steps of fabrication (compare SEM images in Figure 5.3 A).

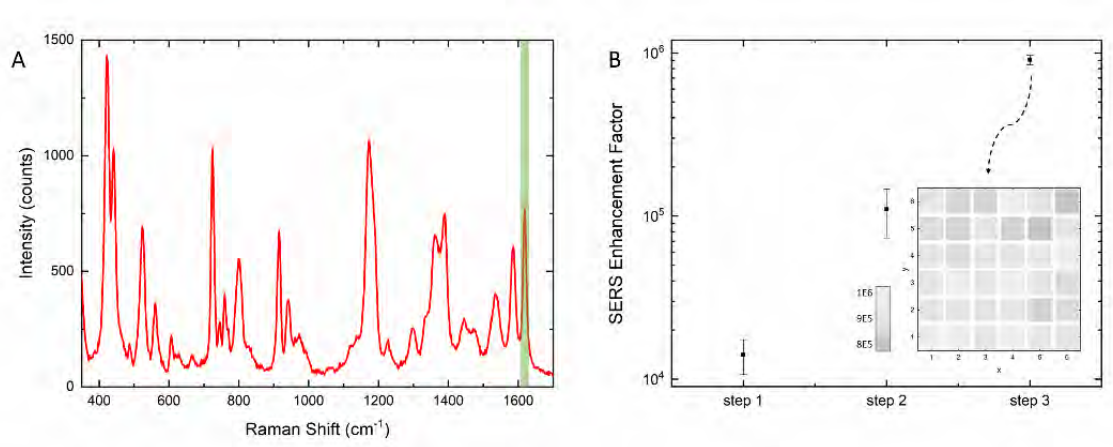

Figure 5.5 Experimental evaluation of enhancement factors. A) Representative single SERS spectrum of crystal violet (c = 10^{-4} M). The signal at 1618 cm^{-1} (marked in green) was used to estimate the enhancement factor (excitation: 785 nm, intensity: 2.0 × 10^5 W/cm^2, acquisition time: 1 s). B) Experimentally determined SERS enhancement factor for each step of substrate fabrication. Inset: Schematic distribution of enhancement factors at positions (x,y) on a substrate after three deposition and annealing steps. Data points are separated by 10 µm in x and y and the diameter of the probed spot was 1 µm (not to scale in the schematic). *Reprinted with permission from [211].*

The enhancement of Raman scattering was confirmed also by culturing cells on the SERS substrates and on uncoated glass slides, as controls. Raman imaging and spectral acquisition of the cells cultured on glass exhibited featureless spectra with low intensity in all cases, using the 785 nm excitation laser and 3 s acquisition time. Utilizing the same acquisition

conditions for cells cultured on the SERS substrates, however, resulted in enhanced spectral fingerprints of the cultured cells, as shown in Figure 5.6 (compare red and black trace). Moreover, as cells were fixed in 4% paraformaldehyde before measurements, the SERS enhancement indicated that cells were attaching sufficiently close to the surface and that Raman signals from the fixed cells were not compromised by the fixative agent.

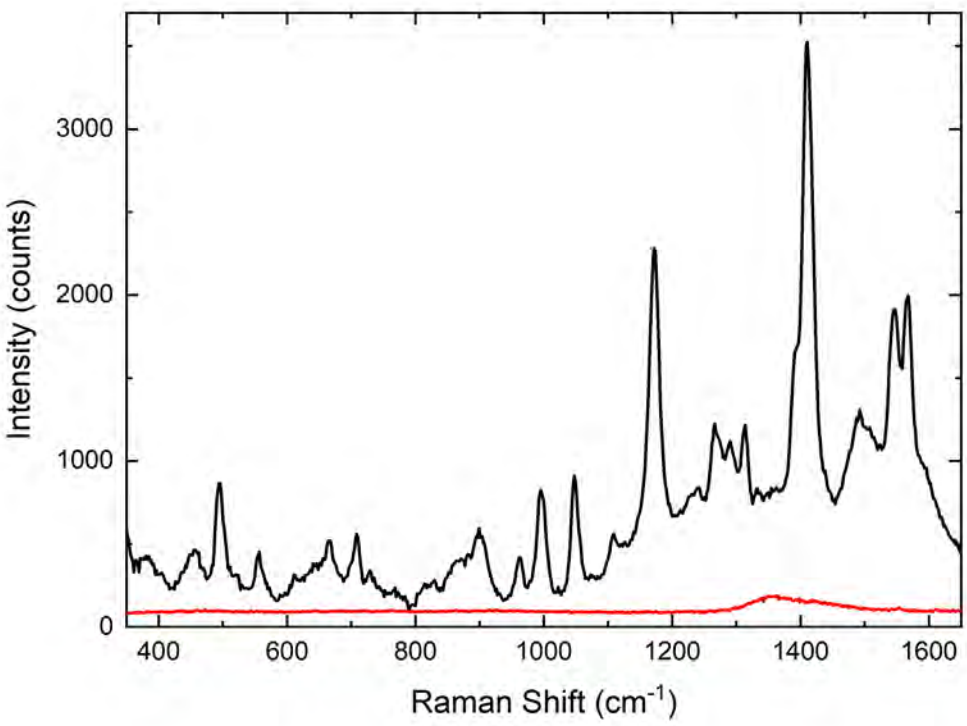

Figure 5.6 Representative Raman spectra obtained from mesenchymal stromal cells grown on a SERS substrate (black line) and on a glass cover slip (red line), respectively. The same excitation and collection conditions were used in both cases (excitation: 785 nm, intensity: 2.0×10^5 W/cm^2, acquisition time: 3 s). *Reprinted with permission from [211].*

5.3 SERS substrate biocompatibility

In SERS, close interaction of the nanostructure with the molecules of the analyte is crucial [221]. Therefore, cell adhesion to the underlying substrate is essential to comply with this requirement. Despite decades of SERS research and development, biocompatible SERS substrates that allow for long term cell culturing are not readily available. In case of mesenchymal stromal cells, biocompatibility of the SERS substrate is the most important prerequisite. The cells can grow, multiply and differentiate only under appropriate conditions and even slight adjustments to the growth environment may determine their fate. Thus, prior to SERS analysis, various viability assays were performed on the fabricated substrates, including immunofluorescence staining, to ensure their biocompatibility and to prove that the cells could thrive in the environment otherwise unknown to them. As controls, the cells were cultured on conventional glass slides and the activity of cells on glass and SERS substrates was compared.

5.3.1 Fluorescence microscopy

In initial experiments, cell attachment to the SERS substrate was essential to ensure the applicability of the methodology for long term cell culturing, using standard culturing protocols. Therefore, an immunofluorescence staining was performed after 10 days of cell proliferation in expansion media, to provide evidence that the cells were able to attach to the underlying substrates. A fluorescent stain 4'6-Diamidino-2-phenylindole (DAPI) exposed the cellular nuclei (Figure 5.6 A), whereas mouse anti-Vinculin monoclonal antibody and FITC-conjugated secondary antibody revealed a clear evidence of F-actin (Figure 5.6 B) and focal adhesion plaques (Figure 5.6 C) at the junctions between cells and the extracellular matrix. In general, cells were observed to be organized in predominantly parallel manner, grown together in clusters, as shown on Figure 5.6 D. DAPI-stained nuclei revealed that cells are in the interphase, and, in some cases, going through mitosis (the brighter stained nuclei have their DNA condensed), as shown on Figure 5.6 A. This confirms that SERS substrates do not disturb proliferation of the cells, nor induce cell death. Immunofluorescence staining was captured by fluorescence microscope Olympus BX51 (Olympus, Tokyo, Japan) using a 40× long working distance objective.

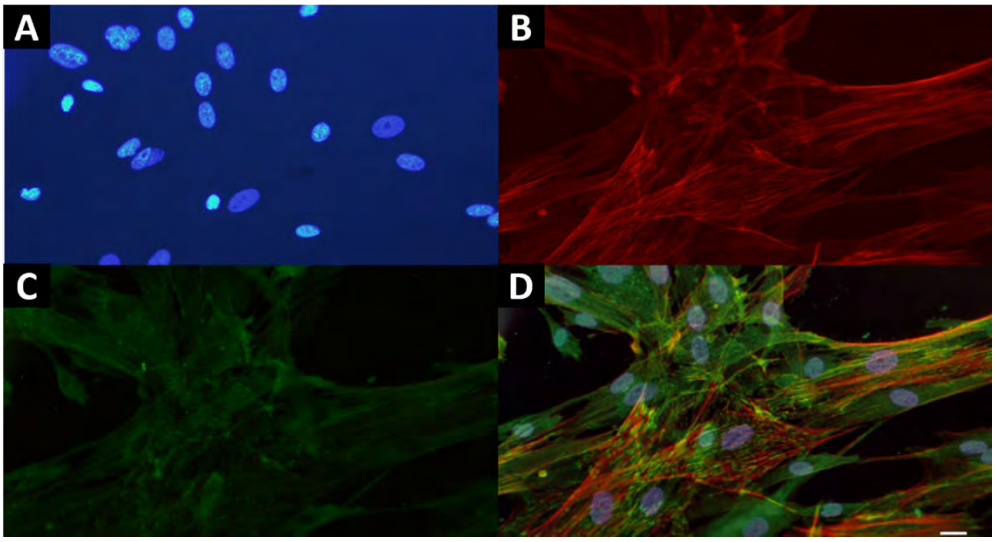

Figure 5.7 Fluorescence microscopy of focal adhesion, actin cytoskeleton and nuclei in mesenchymal stromal cells cultured on the fabricated SERS substrates. A) nuclear counterstaining revealed with DAPI, B) F-actin detected using TRITC-conjugated Phalloidin, C) focal contacts revealed using anti-Vinculin monoclonal antibody and FITC-conjugated secondary antibody, D) overlaid images A, B and C. Scale bar: 100 µm (unpublished data).

5.3.2 Viability assays

Results of colorimetric assessments PrestoBlue proliferation assay and LDH cytotoxic activity assay further determined the biocompatibility of the substrates. For each assay, and for each day of evaluation, three identical SERS substrates and three glass control slides were used, as shown in the experimental setup in Figure 4.4. PrestoBlue assay results revealed increasing proliferation of cells with time (Figure 5.8 A). Cell proliferation remained low until day 3, but it notably increased on day 7. No significant differences were

observed between the three SERS substrates at any point in time during expansion. Moreover, cell proliferation was only slightly lower on the SERS substrates than on the glass controls. Lactate dehydrogenase (LDH) release was evaluated as a marker for substrate toxicity. The results demonstrated that none of the substrates tested had cytotoxic effects on the cells after days 1, 3 and 7 (Figure 5.8 B). LDH release was low at all times, as cytotoxic percentage did not exceed 25%, and furthermore decreased with time. No significant differences were observed between the SERS substrates on one hand, and glass controls on the other hand. Thus, both PrestoBlue and LDH assays confirmed that the SERS substrates are biocompatible, as they did not disturb cell proliferation.

In addition, immunofluorescence staining was performed, followed by imaging with an Olympus FV1200 (Olympus, Tokyo, Japan) confocal laser scanning microscope (as shown in Figure 5.8 C, D). In this case, cell adhesion to the SERS substrates was compared to cell adhesion on conventional culture slides. Identical markers as in the previous experiment were used to reveal cellular components, i.e., actin filaments, which are the main cell adhesion proteins, were detected with TRITC-conjugated Phalloidin, whereas mouse anti-Vinculin monoclonal antibody and FITC-conjugated secondary antibody revealed focal adhesion plaques at the edges of actin filaments (inset in Figure 5.8 C). Cellular nuclei were stained and detected with 4'6-Diamidino-2-phenylindole (DAPI), which binds strongly to A-T rich regions in DNA. Compared to the cells grown on conventional slides (Figure 5.8 D), cells on the SERS substrates tend to grow in higher densities with less spaces between them, although no significant differences in the quantity of cells on both kinds of substrates were observed.

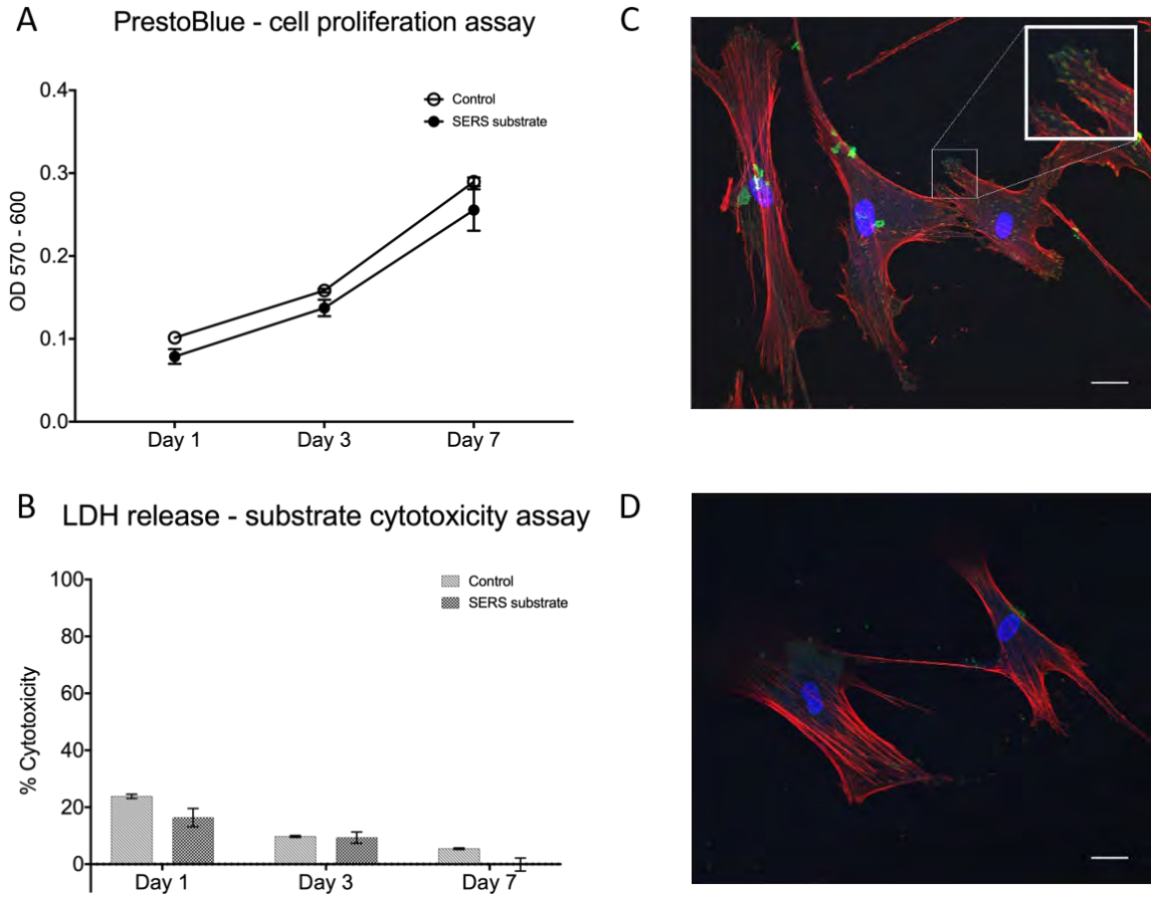

Figure 5.8 A) Results for PrestoBlue cell proliferation assay for BM-MSCs cultured on glass controls and on SERS substrates (n=3), error bars represent the standard deviation. B) Results for LDH cell cytotoxicity assay for BM-MSCs cultured on glass controls and SERS substrates (n=3), error bars represent the standard deviation. C) Representative confocal image of focal adhesion plaques (green), actin cytoskeleton (red) and nuclei of mesenchymal stromal cells (blue) grown on a SERS substrate and D) on a conventional culture slide as control. Scale bars: 20 µm. *Reprinted with permission from [211].*

5.4 Evaluation of the degree of differentiation

As evidenced in Chapter 5.3, bone marrow-derived mesenchymal stromal cells can be successfully cultured on the gold nanoisland SERS substrates developed in the present project. Differentiation of MSCs takes 2-3 weeks and during that time cells need to be maintained under standard conditions, i.e., 37ºC, 95% humidity and 5% CO_2. In addition, osteogenic differentiation is induced by a cocktail of specific chemical factors, such as dexamethasone, ascorbic acid, β-glycerophosphate (BGP), and bone morphogenetic protein BMP2 [200]. All these factors will regulate the osteogenesis process and will take part in determining the fate of the MSCs. The introduction of SERS substrates can also be expected to have an impact on cell behavior. Mesenchymal stromal cells are not uniform populations of cells. Therefore, delivering repeatable results from studies conducted with such cells is challenging, especially considering that individual labs use different isolation and expansion methods [186, 189, 190]. Although cell lines are more robust and can yield highly reproducible results, using MSCs is much more reflective of the *in vivo* environment [35, 36]. Implementing non-invasive approaches, such as SERS, to study heterogeneous populations of cells might broaden our understanding of MSCs and their differentiation processes. However, the interaction between SERS substrates and mesenchymal stromal cells has to be evaluated over a long period of time. In most cases, where SERS is used to study cells, SERS probes, tags or substrates are introduced to the culture media just before the measurement [23, 169], which is both stressful and can induce disarrangement to the equilibrium state of cells. Thus, in this project, long-term proliferation and differentiation of mesenchymal stromal cells on SERS substrates was evaluated, where cells were exposed to the substrates from the beginning of their propagation up until the measurement.

ALP activity assay was used to evaluate the degree of differentiation on SERS substrates and compared to conventional glass slides in two independent experiments, using two independent MSC donors. Results indicated that the enzymatic activity of ALP increased during the osteogenic differentiation process of MSCs, regardless of the substrate used (Figure 5.9). The increase in ALP activity was observed from day 7 to day 21. After 7 and 14 days of osteogenesis, ALP activity was slightly lower on the SERS substrates, as compared to glass controls. The peak in ALP activity was observed on day 21, with negligible differences between SERS and glass substrates. On day 28, however, ALP activity decreased for both SERS and glass substrates, indicating that differentiation had ceased. Although the enzymatic activity of ALP was lower on SERS substrates, than on glass slides, the differentiation was not compromised, as it followed the same pattern on SERS substrates and glass slides.

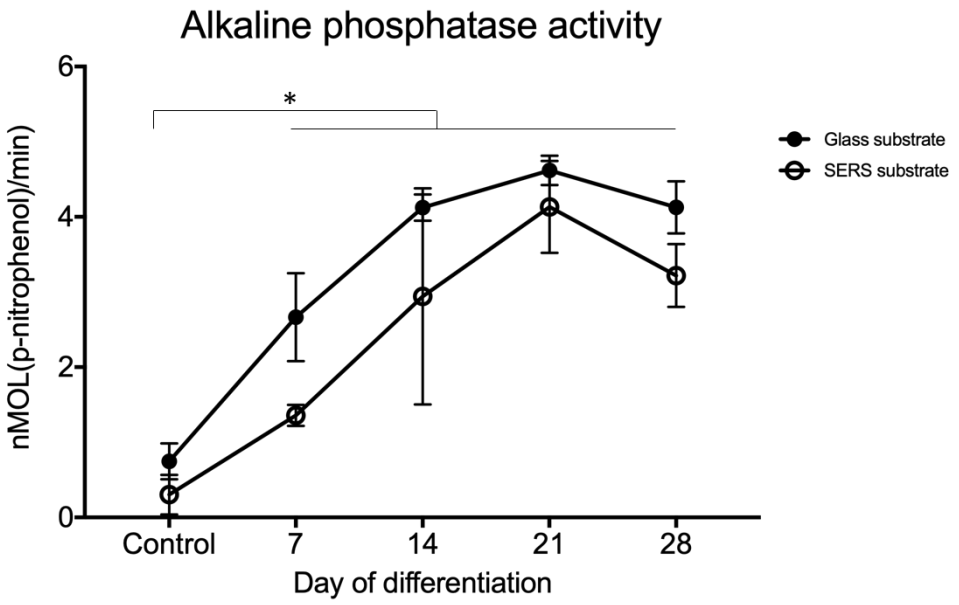

Figure 5.9 Alkaline phosphatase activity during osteogenic differentiation. Mesenchymal stromal cells (MSCs) cultured in osteogenic media on SERS substrates and glass controls were assessed for ALP activity on days 7, 14, 21 and 28. MSCs cultured in expansion media were included as control. Points represent averages of n = 6 cell cultures per timepoint assessed in two independent experiments. Asterisk over bracket indicates statistical significance versus control. * $p < 0.05$; Two-way ANOVA with Tukey's post hoc test. *Reprinted with permission from [222].*

Mineralization of the matrix by deposition of calcium hydroxyapatite crystals during osteogenic differentiation process was visualized by Alizarin Red S staining. In control cultures on conventional glass slides calcification can be observed over a period of 28 days. The amount of mineralization and changes in osteoblast morphology were exceptionally similar for cells cultured on SERS substrates. As can be seen on Figure 5.10 A and F, for cells cultured in non-osteogenic media, there was no evidence of mineral formation, regardless of the substrate on which they were grown. When cultured in osteogenic medium, after 7, 14, 21 and 28 days, cells on both types of substrates changed their morphology from fibroblastic appearance to more cuboidal shapes and the mineralized cell clusters consisting of calcium hydroxyapatite crystals were clearly stained red (see Figure 5.10 B, C, D, E and G, H, I, J; indicated with black arrows). From day 7 on, cells started forming aggregates, which occurred prior to nodule formation and continued to expand in size with time in the osteogenic medium. These dense mineralized structures (magnified areas on the SERS substrates for days 7, 14, 21 and 28 shown in Figure 5.10 K) are referred to as bone nodules. The staining confirmed that nodule formation and deposition of mineralized matrix occurred in discrete patches throughout the cell culture, further indicating that the mesenchymal stromal cells, and thus the processes they are undergoing, are not homogeneous. The fact that each cell differentiates according to its own pace makes quantification of osteogenesis immensely difficult, showing how important it is to study such populations of cells also at the single cell level. Although the cells on glass control are more confluent than on the SERS substrates, there are no differences in the quality of differentiation between different substrates. The results from both colorimetric and staining assays evidently show that SERS substrates do not adversely affect the long-term differentiation process of cells, despite the

fact that cells tend to grow in smaller quantities than on conventional glass slides. The quality of differentiation, however, is equally advanced, regardless the substrate used.

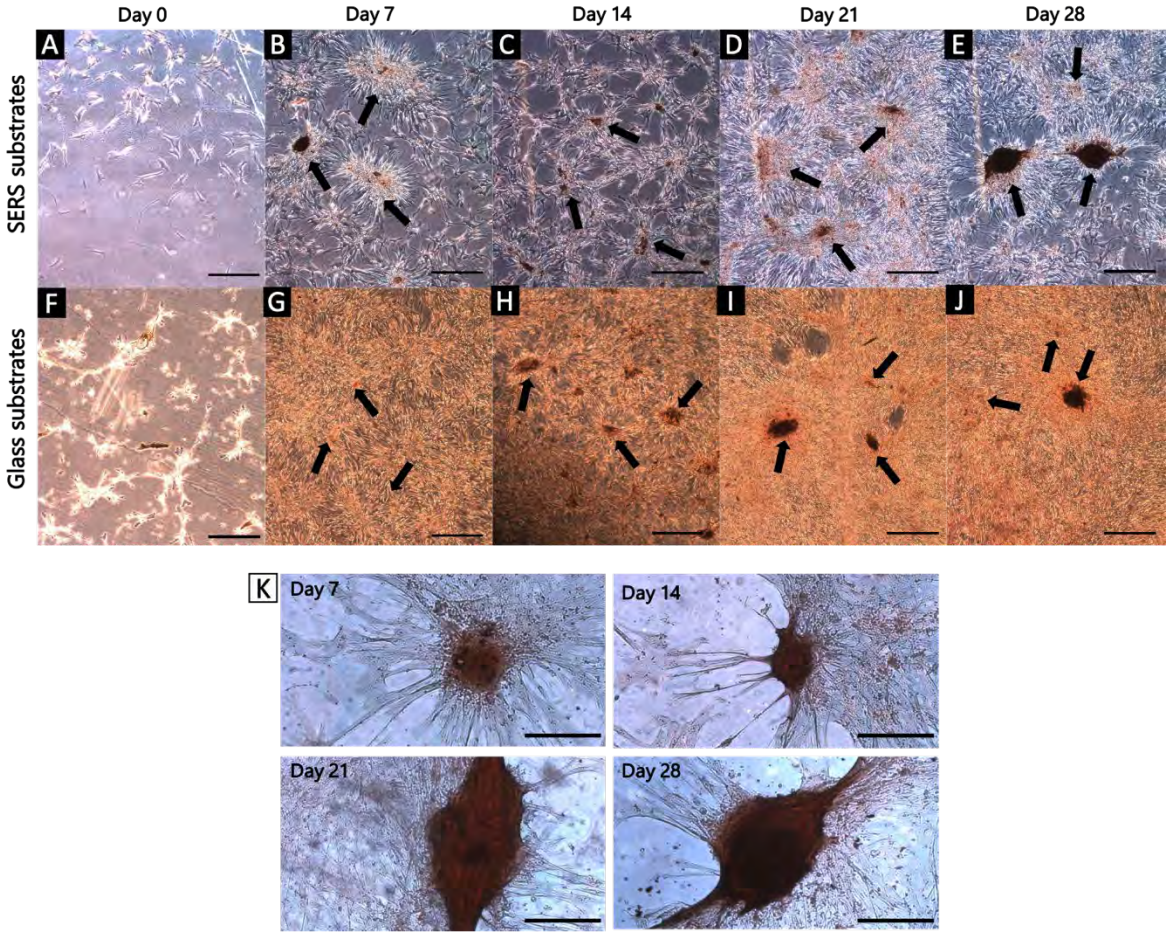

Figure 5.10 Mineralization during osteogenic differentiation. Mesenchymal stromal cells (MSCs) on SERS substrates (A-E) and glass controls (F-J) stained with Alizarin Red S on days 7, 14, 21 and 28 of osteogenic differentiation. MSCs cultured in expansion media (A, F) included as controls. Black arrows depict mineralized clusters. Scale bars: 100 µm (A-J). K magnified areas of osteogenic cell mineralization on SERS substrates for days 7, 14, 21 and 28. Scale bars: 20 µm (K). *Adapted in part with permission from [222].*

5.5 SERS characterization of mesenchymal stromal cells

The use of SERS as a sensitive tool to detect signals from cell membranes and to characterize the molecular changes during long term osteogenic differentiation at the interface between the outer cell membrane and the gold nanoisland substrates was one of the main targets of the present study. In addition to ensuring close proximity between the cultured cells and the substrates, as discussed above, spectral acquisition conditions had to be optimized to prevent prolonged cell exposure to laser light in order to avoid photodegradation and unnecessary disturbance of the cells. Based on a comparison of previous research by other groups,

optimum laser powers of the near-IR 785 nm laser and corresponding acquisition times were selected, i.e., up to 5mW laser power and 3 seconds acquisition time for each imaging point.

5.5.1 SERS detection of MSC signal

In initial experiments, the compatibility of the substrates with MSC growth and subsequent SERS imaging was tested, confirming that enhanced Raman signals were detected and that they could be correlated with imaged cells (Figure 5.11). Raman maps overlaid on bright-field images of cells were recorded over the spectral range of 100 cm^{-1} to 1800 cm^{-1}. The map on Figure 5.11 B is based on the intensity of 462 cm^{-1} band. The brightest pixels on the map indicate the highest intensities of the selected band, which are predominantly located at the focal contacts of adhering cells. Cell attachment there is the strongest, thus probed molecules are in close vicinity to SERS hot spots. The example SERS spectrum on Figure 5.11 A displays several distinct bands, which can be assigned chiefly to modes of lipids (552 cm^{-1} band of cholesterol, 1450 cm^{-1} C-H vibration mode of lipids), carbohydrates (847 cm^{-1} band of monosaccharides) and proteins (1208 cm^{-1} mode of phenylalanine, 1234 cm^{-1} band of amide III) [223, 224]. The molecular components that can be correlated with the detected bands are mostly present on the outer cell membrane [31, 225, 226], indicating that the probed signals are consistent with biomolecules located close to the underlying substrate, as the cell membrane and its immediate vicinity is the only part of the cell in direct, nm-proximity contact with the metallic nanostructure. A comprehensive investigation on cell membrane components is described in the following section.

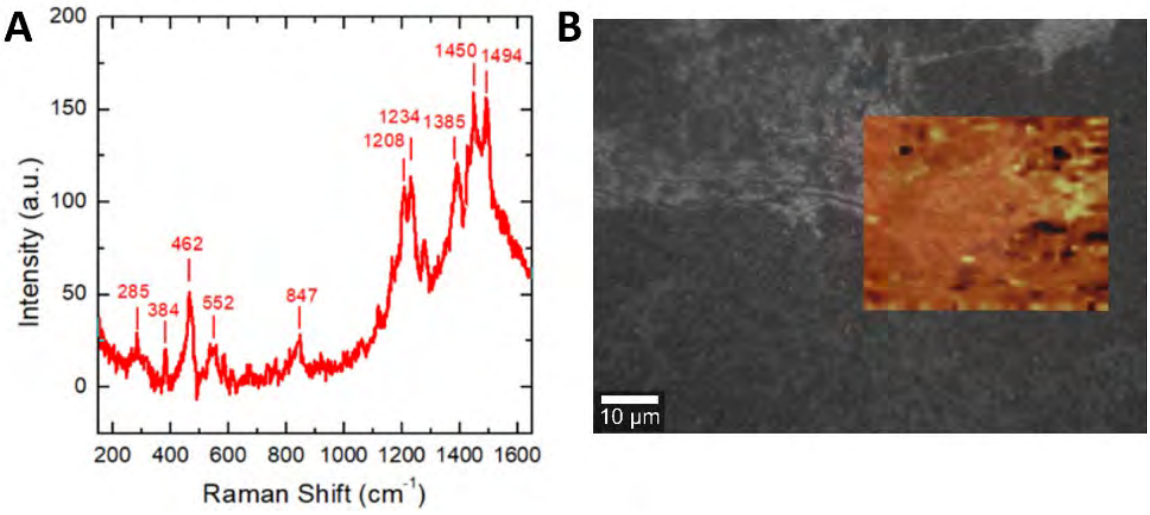

Figure 5.11 A) Raman spectrum from a fixed undifferentiated MSC cultured on a gold nanoparticle film. The broad background signal from 1100-1600 cm^{-1} originates from the glass substrate. B) Raman image (462 cm^{-1} band) overlaid on an optical microscope image of the MSCs. Excitation wavelength: 785 nm, acquisition time: 5s. *Adapted in part with permission from [216].*

5.5.2 SERS spectra from mesenchymal stromal cells

On selected parts of bone marrow-derived mesenchymal stromal cells (BM-MSCs) cultured on gold nanoisland SERS substrates, Raman maps with over 400 spectra each were collected. Representative SERS spectra from two different MSCs on two different SERS substrates are

shown in Figure 5.12 and tentative assignments of the representative bands are listed in Table 5.2. The spectra exhibit a wide diversity within different parts of the cell. However, several bands dominate the spectra, and these can be assigned predominantly to proteins, lipids, and carbohydrates, presumably from the outer cell membrane. As discussed in previous sections, SERS spectra can be only generated from spots where the molecules of interest are located in close vicinity to the nanostructured surface. Thus, the probed molecules are predominantly, although not exclusively, constituents of focal adhesion sites that anchor the cytoskeleton within the extracellular matrix, as well as the external part of the cellular membranes. Prior to SERS measurements, cells on SERS substrates were fixed in paraformaldehyde to prevent them from degradation before they were observed with the microscope. There is evidence that fixing procedures may alter the Raman spectra of fixed cells as compared to unfixed cells [15], although methanol is considered more invasive than formaldehyde. Nevertheless, the possible influence of the fixative has to be taken into account in the interpretation of data. As some studies suggest that paraformaldehyde induces changes in the Raman spectra of nucleic acids and proteins [227, 228], the possible signals correlated with cellular interior cannot be excluded.

Characteristic peaks that can be correlated with the molecules synthesized during extracellular matrix formation, i.e., on the outer part of the cell, that can confirm the origin of the SERS signals to the cellular exterior and membrane regions are bands at 1067 cm^{-1} of proline and 1322 cm^{-1} of CH_3CH_2 twisting, considered pivotal markers of collagen type I [223], the main element of the ECM [31, 192, 193, 225]. The most distinctive peaks, however, are those that can be assigned to the vibrations of proteins, e.g., bands at 524 cm^{-1} corresponding to S-S stretching vibration of disulfide bridges that are found in many different proteins [223, 224, 229], or the 1552 cm^{-1} vibration band associated with tryptophan C=C stretching [223, 224]. Other major protein-related vibrations were found at 823 cm^{-1}, 1002 cm^{-1} and 1304 cm^{-1}, representing a ring breathing mode of tyrosine, symmetric stretching of phenylalanine, and a component of the amide III band, respectively [223, 224, 229-232]. The band at 1278 cm^{-1}, assigned to an amide III vibration of proteins, but also to the symmetric stretching of PO_4^{3-} that can be attributed to phosphate groups contained in the phospholipids [223, 224, 233, 234] has a significant presence in the SERS spectra. The lipid-related vibrational modes are represented by bands at 418 cm^{-1} or 608 cm^{-1} of cholesterol, phospholipid alkyl chains at 1140 cm^{-1}, unsaturated fatty acids at 1270 cm^{-1} and CH_2 deformation of lipids at 1440 cm^{-1} [223, 224, 230, 232, 233, 235]. Several bands that also often appear in the spectra relate to the vibrations of carbohydrates, such as the peak at 842 cm^{-1} characteristic of polysaccharides [223, 224], known to be major constituents of the extracellular matrix.

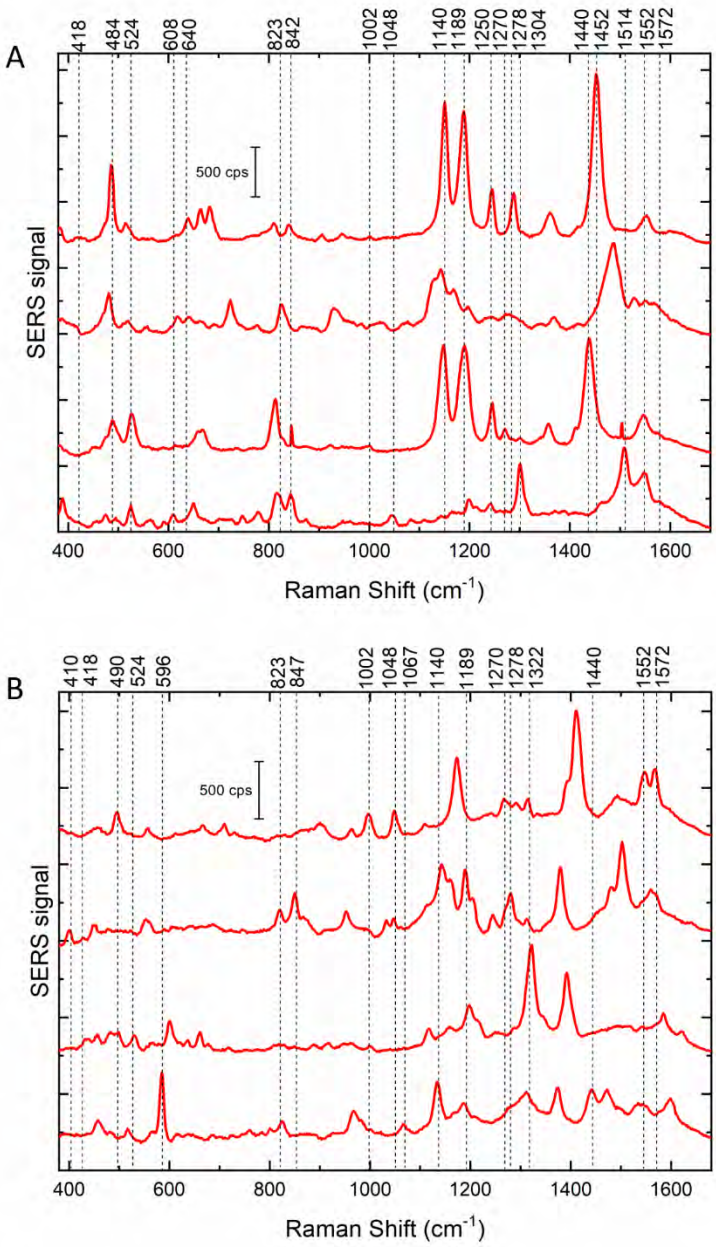

Figure 5.12 Representative SERS spectra extracted from the mapping datasets of two different mesenchymal stromal cells on two different SERS substrates (excitation: 785 nm, intensity: 2.0×10^5 W/cm^2, acquisition time: 3 s, step size: 2 μm). *Reprinted with permission from [211].*

Table 5.2 *Tentative assignments of the most representative bands in the SERS spectra of BM-MSC cells obtained during mapping, based on Refs. [161, 223, 229-233, 235-237]*

Raman shift [cm^{-1}]	Tentative assignments
410	CH_2 bending, phosphatidylinositol
418	CH_2 bending in the ring, cholesterol
484-490	C-O-C ring deformation, carbohydrates, e.g., glycogen
524	S-S disulfide stretching, proteins
596	Phosphatidylinositol
608	Cholesterol
640	C-S stretching and C-S twisting, proteins
823	Ring breathing, tyrosine
842-847	C-O-C skeletal mode, polysaccharides
1002	C-C symmetric stretching, symmetric ring breathing, phenylalanine
1048	Polysaccharide, e.g., glycogen
1067	Proline, e.g., in collagen
1140	C-C stretching, phospholipid alkyl chains
1189	Arginine
1270	C=C groups, unsaturated fatty acids
1278	PO_4^{3-} stretching and amide III, lipids and proteins
1304	CH_2 twist and amide III, lipids and proteins
1322	CH_3CH_2 twisting, collagen
1440	CH_2 deformation, lipids
1514	N-H deformation, proteins
1552	C=C stretching, tryptophan

5.5.3 SERS mapping of the biochemistry of the cell membrane

To gain insight into the allocation of molecules represented by the important bands, some of the vibrational modes were mapped and shown as chemical images in Figure 5.13. Chemical maps of two different cells are constructed based on bands that can be assigned to proteins, lipids, and carbohydrates, which are the main components of the cells, and in case of the lipid signals possibly to the cell membrane. The maps of bands assigned to cholesterol (418 cm^{-1}), phospholipid alkyl chains (1140 cm^{-1}), polysaccharides (842 cm^{-1}), C=C stretching of tryptophan (1552 cm^{-1}), S-S disulfide stretching in proteins (524 cm^{-1}), CH_2 deformation in lipids (1440 cm^{-1}), symmetric stretching of phenylalanine (1002 cm^{-1}), and fatty acid (1270 cm^{-1}) show the signal distribution of the respective molecular species. The pixels of high intensity in the maps generated at 1140 cm^{-1} and 1440 cm^{-1} (see red maps in Figure 5.13) are co-localized, in agreement with both bands being assigned to lipid chains, mainly phospholipids, known to be the most abundant membrane lipids [31, 225, 238]. Furthermore, the distribution of high signal intensities assigned to phospholipids correlates with the distribution of a high signal band at 418 cm^{-1} (see green map in Figure 5.13), which indicates the presence of cholesterol, known to co-localize with phospholipids [226]. In Figure 5.14, representative spectra from two labeled positions in the map of the band intensity 418 cm^{-1} of cholesterol are shown, further illustrating the co-localization of the different spectral signals assigned to membrane lipids. In agreement with the above discussion, the spectra from the labeled positions contain several bands characteristic of lipid vibrations (418 cm^{-1}, 1140 cm^{-1}, 1270 cm^{-1} and 1440 cm^{-1}). The fatty acids in phospholipids can vary in length, hydroxylation, and saturation. As indicative from the signal at 1270 cm^{-1}, unsaturated chains of fatty acids containing *cis*-double bonds are present and co-localize with the high signals from the phospholipids at 1140 cm^{-1} and 1440 cm^{-1}, conclusively confirming the vibrational

assignment to lipid molecules. Unsaturated fatty acids are known to be responsible for membrane fluidity and adding strength to the cell membrane [226].

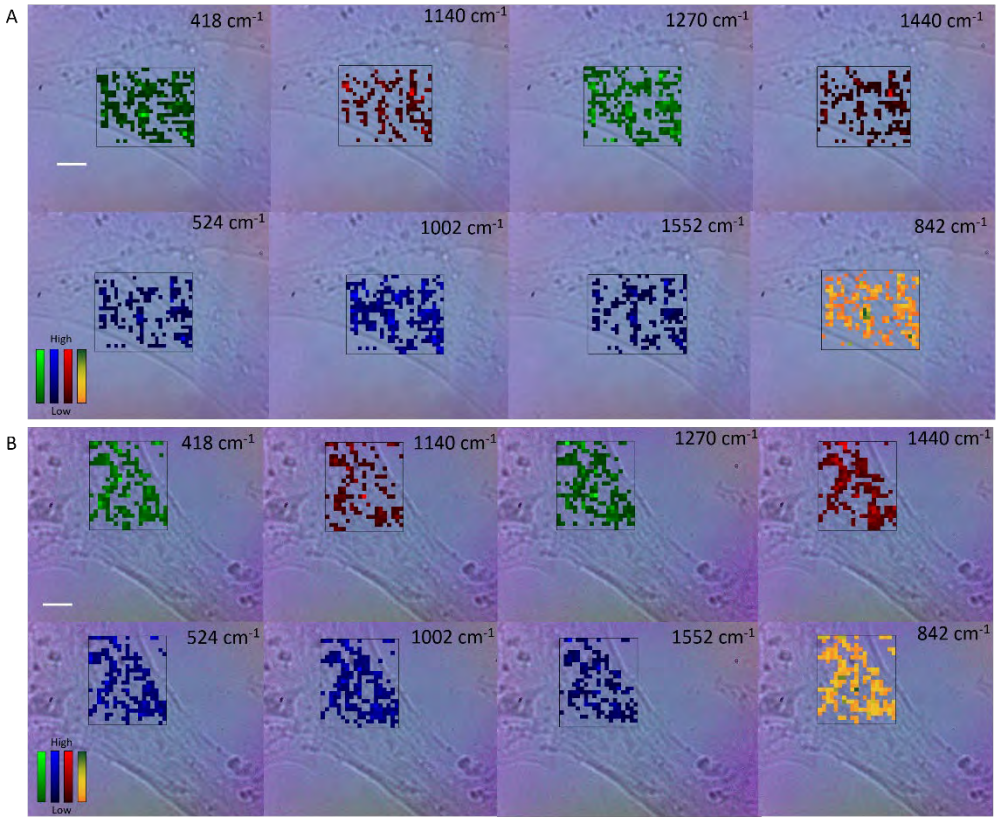

Figure 5.13 Raman maps showing the distribution of SERS signals in two different BM-MSCs on two different SERS substrates, and their overlay with microscope images. Raman maps are generated by mapping intensities at 418 cm^{-1} assigned to cholesterol (green), 1140 cm^{-1} to phospholipid alkyl chains (red), 1440 cm^{-1} to CH_2 deformation in lipids (red) and 1270 cm^{-1} to C=C groups in unsaturated fatty acids (green), 524 cm^{-1} to S-S disulfide stretching in proteins (blue), 1002 cm^{-1} to phenylalanine symmetric C-C stretching (blue), 1552 cm^{-1} to tryptophan C=C stretching (blue) and 842 cm^{-1} to polysaccharides (yellow). Scale bars: 10 μm. *Reprinted with permission from [211].*

The Raman cross sections of various vibrational modes of proteins vary significantly, with amino acid side chains yielding the highest signal intensities [239]. Several bands related to protein species were observed in the spectra, including the band at 1002 cm^{-1} of the amino acid phenylalanine and a band at 524 cm^{-1} that can be assigned to the S-S stretching vibration of disulfide bonds. In membrane proteins, such disulfide bridges are formed on the non-cytosolic side [229, 240], where they can help stabilize the folded structure of the polypeptide chains. This provides further indication that the SERS substrate mainly probes the outer membrane of the adhering cells. It can be seen in Figure 5.13 that the maps of the band at 524 cm^{-1} overlap with the maps of the band at 1002 cm^{-1}, the latter including contributions also from other proteins than exclusively those with an abundance of disulfide bonds. Another characteristic band of proteins can be found at 1552 cm^{-1} and is assigned to the C=C stretching of tryptophan [237]. Its abundance in membrane proteins is also high, and the amino acid preferentially resides near the polar heads of the lipids in the membrane bilayers [241], which also explains the similar distribution to that of the lipids (compare the blue and the red maps in Figure 5.13). The map of the band at 842 cm^{-1}, assigned to

carbohydrates [223, 224], also often co-localizes with the lipid bands (yellow maps in Figure 5.13). This may be due to the fact that the bilayers contain lipids with sugars attached by glycosidic bonds, known as glycolipids [31, 225], which explains the localization of the lipids and carbohydrates at similar positions in the maps.

In can be also noted that the distribution of the intensity of the peak at 1002 cm^{-1}, which is assigned to the ring breathing of phenylalanine [223, 224], widely matches that of the band at 842 cm^{-1}. This is in agreement with the fact that many outer membrane proteins are glycosylated [226, 242].

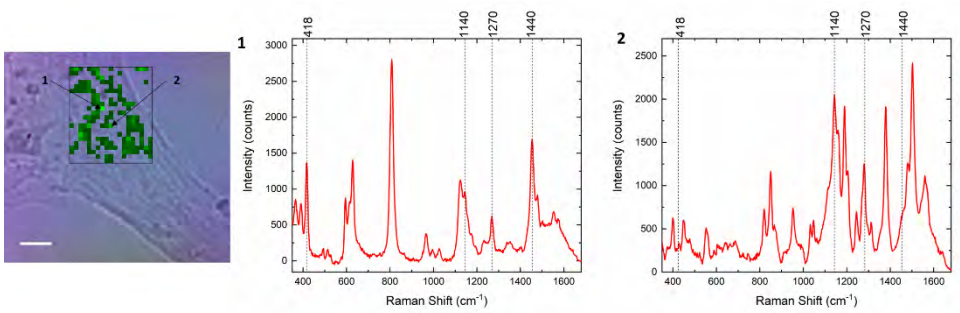

Figure 5.14 Chemical image displaying the distribution of the band intensity at 418 cm^{-1}, assigned to cholesterol, followed by example spectra extracted from the maps at two different points labeled in the panel. The SERS spectra represent two different intensities of the 418 cm^{-1} band (excitation: 785 nm, intensity: 2.0×10^5 W/cm^2, acquisition time: 3 s, step size: 2 μm). Scale bar: 10 μm. *Reprinted with permission from [211].*

The data above confirms that informative SERS studies of cellular membranes are possible using the fabricated gold nanoisland substrates, as long as tight adhesion of cells to the underlying surface is realized. Respective spectra of molecular fingerprints relating to lipids, proteins and carbohydrates were obtained without targeting specific molecular species and in spite of that, their co-localization in chemical maps suggests the probing of cell membrane components. This selectivity, however, is a direct effect of the substrate SERS enhancement that results from the intimate contact of the cells with the gold nanosurface. This particular model of cell culturing directly on the surface-enhanced Raman scattering substrates of self-organized gold nanoislands offers a unique way to investigate the molecular aspects of the behavior of mesenchymal stromal cells *in vitro*, and yields insight into differentiation process, as well as being suitable for live cell studies, as described in the following chapters.

5.6 SERS of osteogenic differentiation

Precise characterization of mesenchymal stromal cell differentiation into specific lineages, particularly using non-destructive and non-invasive approaches, is pivotal for generating patient-specific therapies. The differentiation process of heterogeneous populations of mesenchymal stromal cells is far from being completely understood, although many research groups have explored Raman microscopy and SERS to obtain better insight into the osteogenesis process in a non-invasive, label-free way [22, 49, 50, 52, 167, 169-171, 243]. These works represent comprehensive descriptions of detection of osteogenic markers, such as following changes in hydroxyapatite peaks during the course of osteogenesis [52] or intracellular monitoring of microRNA changes throughout differentiation [169], as well as discrimination between different MSC subtypes [167]. Many efforts have been directed

towards detection of 959-966 cm^{-1} PO_4^{3-} symmetric vibration of calcium hydroxyapatite and comparison of its intensity at different timepoints during osteogenic differentiation. However, inconsistencies have arisen as different research groups have reported the initial appearance of this peak in Raman spectra on different days of differentiation. Suhito et al. [22] detected the hydroxyapatite peak at day 9 of differentiation and Manadir et al. [243] at day 8, whereas for McManus et. al. [49] and Hofemeier et al. [52] its first appearance was at day 14. In all these studies, stem cells were used, and yet they have produced such varying results, which only proves how heterogeneous stem cells are. The present study has been directed towards increasing knowledge about the differentiation process, by studying it at the single-cell level in a non-disruptive manner. Undifferentiated cells (depicted as day 0 for simplification) and cells after 7 and 21 days of culturing in osteogenic media were extensively described, as they mark important timepoints during osteogenic differentiation of these specific BM-MSCs used in the study, as exhibited by colorimetric ALP assay, where day 7 marks first signal of differentiation and day 21 marks the peak of osteogenesis. For these timepoints the differences are expected to be most significantly reflected in SERS spectra. In addition, some examples of SERS spectra for days 14 and 28 will also be presented below. Although the present studies of BM-MSCs osteogenic differentiation were performed on fixed cells, there are strong indications that this process can be conducted on live cells as well, with the suitable equipment. Live-cell studies on fibroblast cells will be demonstrated in Chapter 5.7.

5.6.1 SERS spectra from mesenchymal stromal cells undergoing the osteogenic differentiation process

The observed SERS spectra extracted from the mapping datasets of both undifferentiated MSCs and MSCs grown in osteogenic media for 7 and 21 days for two independent donors reflect the biochemistry and dynamics of the mesenchymal stromal cells undergoing osteogenic differentiation. Mapping datasets yielded between 500 and 800 SERS spectra for each imaged cell. They were found to exhibit a large degree of diversity within different parts of the cell. On the other hand, the averages of all SERS spectra from different individual cells represent a high degree of similarity, indicating low overall cell-to-cell variability. The spectral averages are dominated by several strong bands, most of them assigned to vibrations of proteins and lipids, being principal components of all cell membranes. Nevertheless, as osteogenic differentiation occurs widely in the stem cell niche, i.e., on the outer cell membrane, changes in the SERS spectra during differentiation are expected. Averages of SERS spectra on days 0, 7 and 21 from two independent donors are shown in Figure 5.15 with their main tentative assignments listed in Table 5.3.

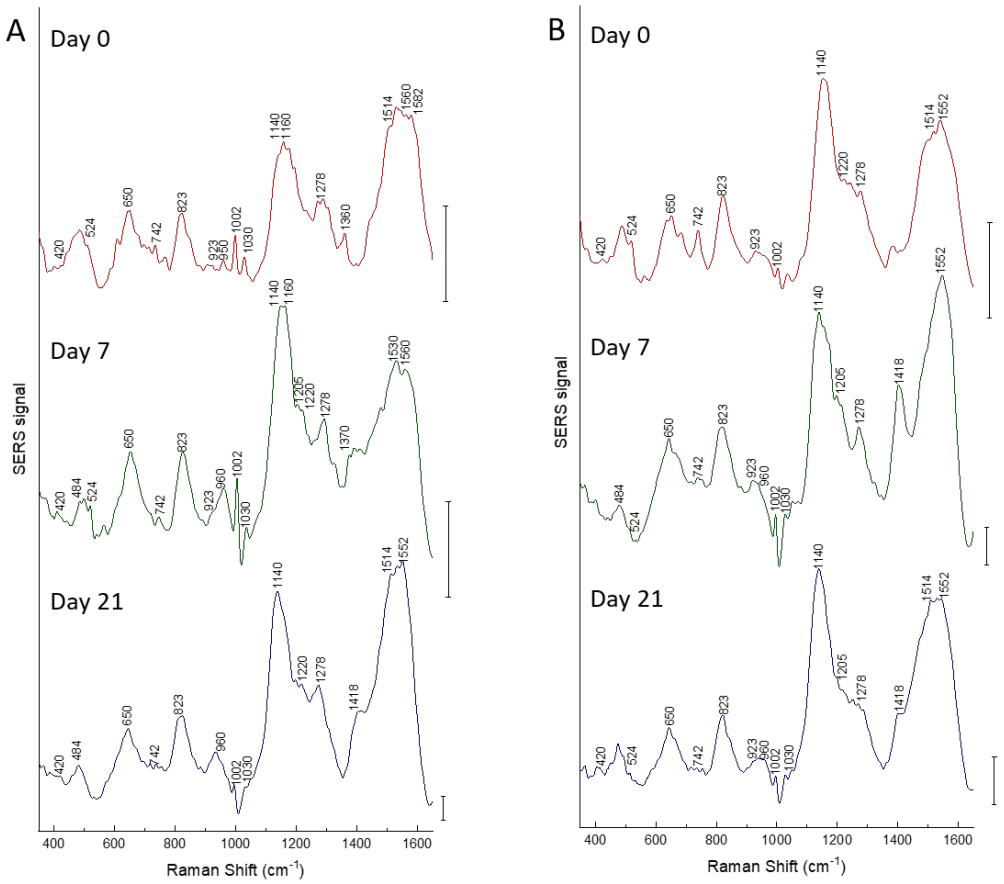

Figure 5.15 Averages of SERS spectra extracted from the mapping datasets of mesenchymal stromal cells from two independent donors. Each spectrum is an average of all SERS spectra measured in one part of an individual cell. The total number of SERS spectra contributing to the average is between 500 and 800 individual measurements. Control spectra of undifferentiated cells (day 0), spectra of cells differentiated for 7 days and spectra of cells differentiated for 21 days are shown. Excitation wavelength: 785 nm, excitation intensity: 6.0×10^5 W/cm^2, and acquisition time: 3s. Scale bars: 10 cps. *Reprinted with permission from [222].*

The most abundant modes present in SERS spectra include bands at around 505-524 cm^{-1}, 645-650 cm^{-1}, 1002 cm^{-1} and 1552-1560 cm^{-1} originating from different vibrations of proteins [223, 224, 229]. The bands at 1130 cm^{-1} and 1140 cm^{-1} can be assigned to C-C stretching modes of lipid chains [223, 224, 233, 235] and the band at 1440 cm^{-1} is present due to the deformation vibrations of the CH_2 groups from fatty acids [244]. Also, bands at 415 cm^{-1} and 420 cm^{-1} can be correlated with phosphatidylinositol [223, 224], residing in the plasma membrane, and CH_2 bending in the ring of cholesterol [233], respectively. Stretches of amide III (1220 - 1278 cm^{-1}) are also widely present in the representative SERS spectra (Figure 5.16). Specifically, the mode at 1278-1280 cm^{-1}, assigned to amide III band of proteins, but also symmetric stretching of PO_4^{3-} correlated with phosphate groups contained in phospholipids [223, 224, 229]. In undifferentiated MSCs spectra, there is little or no evidence of a PO_4^{3-} symmetric stretching band of phosphate of hydroxyapatite (mode between 960 cm^{-1}, 966 cm^{-1}, up to 970 cm^{-1}, depending on the matrix mineral maturation). However, it starts to appear on day 7 of differentiation, as noticed on both averaged and

single representative SERS spectra. This further suggests that the biomolecular composition of cell membranes changes during differentiation and is different from that of undifferentiated control cells. Some proline and hydroxyproline contributions around 923 cm^{-1} can be found on undifferentiated cells, which are the sign of collagen synthesis during extracellular matrix formation [49, 170, 243]. On day 7, when osteoblasts start to form, the bands associated with collagen fibrils [170, 223, 224] at 813-817 cm^{-1}, 852-856 cm^{-1} and 923 cm^{-1} of proline and hydroxyproline, are more prominent. This can be related to the fact that osteoblasts produce so-called osteoids, which are freshly deposited new uncalcified matrix, consisting chiefly of type I collagen [31, 34, 245]. Also, the contributions of PO_4^{3-} symmetric stretching band of hydroxyapatite $Ca_{10}(PO_4)_6(OH)_2$ start to appear near the 960 cm^{-1} region, which is a sign of rapid conversion of osteoids into hard bone matrix by the deposition of calcium phosphate crystals [33, 34, 49]. This mode varies in intensity from spectrum to spectrum, indicating that the mineralization is highly localized and that cells start to differentiate in aggregates and not evenly in monolayers, in agreement with the results of Alizarin Red S staining, where clear calcified patches were distinguished (see Figure 5.10). This is also well represented by SERS spectral averages, where the hydroxyapatite band at 960 cm^{-1} indeed appears at day 7 and 21, but it does not dominate the spectra, which further indicates the heterogeneity of differentiation within a single cell. Moreover, with the progress of differentiation we can also notice a higher degree of multiplexing of the SERS signals, suggesting that more bands in the similar vibrational range contribute to one wide band. Therefore, the investigation of single-point SERS spectra brings more information about the differentiation progress within one cell and hence the cell population. In the initial stage of osteogenic differentiation, so called calcium-phospholipid-phosphate complexes are formed, which are known to trigger the biological mineralization process [246, 247], consistent with the band at 1280 cm^{-1} assigned to phosphate groups contained in phospholipids being more prominent on day 7 than on undifferentiated cells (Figure 5.16). This correlates well with the increase of the hydroxyapatite mode at 960 cm^{-1}. Prior to detectable mineral formation, signals from complexed acidic phospholipids appear to be increasing, suggesting that these lipids play a role in promoting calcification [246-248]. The mode at 1278-1280 cm^{-1} is additionally assigned to amide III stretches of proteins, therefore direct correlation between phospholipids and mineral formation is difficult to extract from the SERS spectra. Nevertheless, the mode at 1278-1280 cm^{-1} is more pronounced in the averaged SERS spectra on day 7 of differentiation, as compared to undifferentiated cells (Figure 5.15), suggesting increased presence of phospholipids in the cell membrane, presumably due to the formation of calcium-phospholipid-phosphate complexes (compare average spectra on day 7 and 21 in Figure 5.15), also further indicating the importance of these complexes mainly in the initial stages of osteogenesis. Several vibrational modes that are often appearing in the spectra and can be attributed to phosphates of HA [170, 223, 224], are 589 cm^{-1}, present mostly on day 7 of differentiation, and symmetric stretching of $v_3PO_4^{3-}$ in the spectral range between 1044 and 1076 cm^{-1}, which is more prominent later in the culture. On day 21, the SERS spectra exhibit more pronounced signals of hydroxyapatite and the slight band shift to higher frequencies between 966 cm^{-1} and 970 cm^{-1}, which highlight changes in mineral crystallinity of bone tissue components throughout the cell culture [31, 33, 34]. Bone tissue combines various amounts of the mineral species at different levels of development within each cell, resulting in differences in phosphate band positions [49, 170, 243]. This further indicates the complexity of the differentiation process and difficulties in quantifying it.

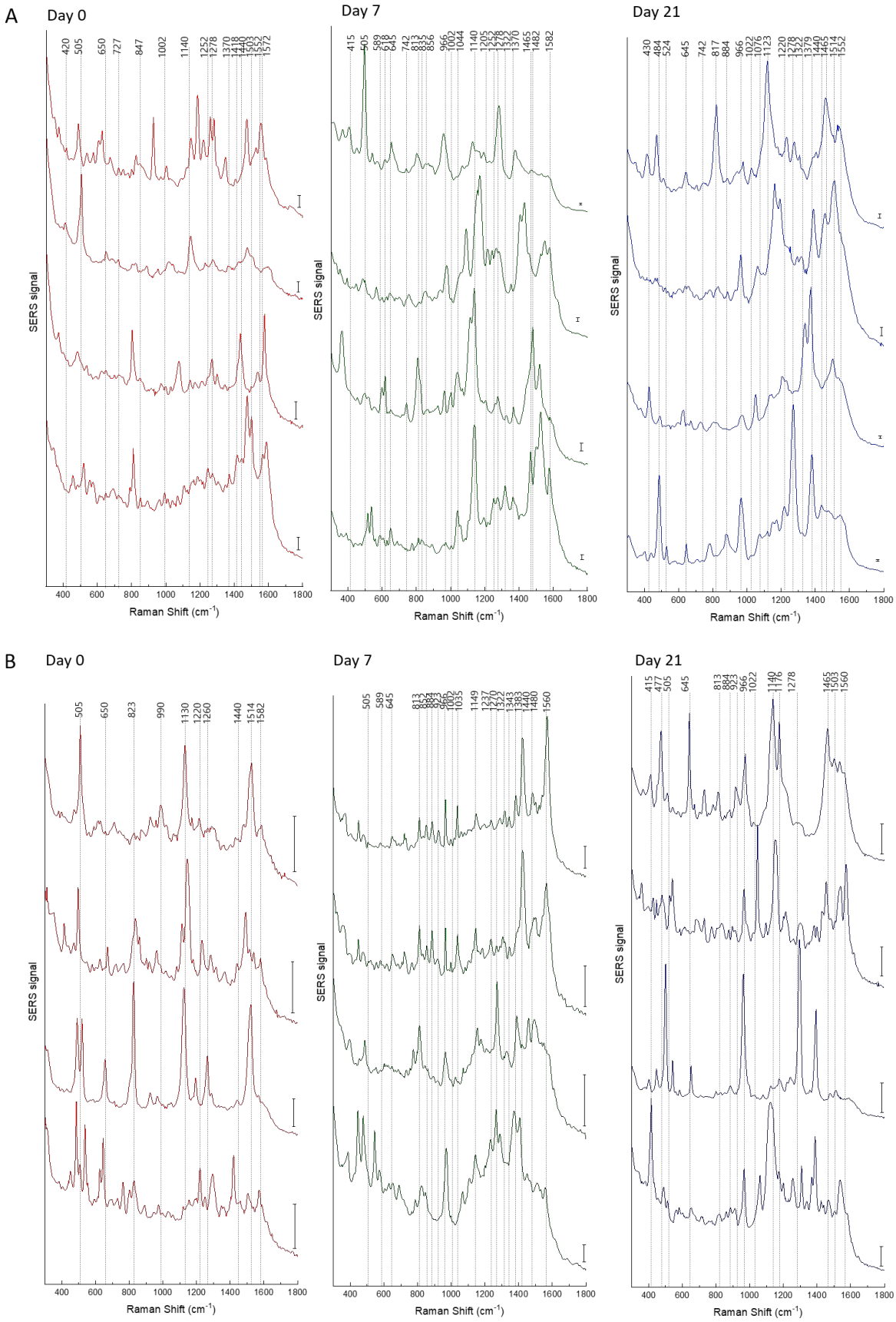
A
Day 0
Day 7
Day 21
SERS signal
Raman Shift (cm-1)
420 505 650 727 847 1002 1140 1252 1278 1370 1448 1503 1552 1572
415 505 589 618 645 742 813 835 856 966 1002 1044 1140 1205 1278 1322 1370 1465 1482 1582
430 484 524 645 742 817 884 966 1002 1076 1123 1220 1278 1322 1379 1440 1465 1514 1552
B
Day 0
Day 7
Day 21
SERS signal
Raman Shift (cm-1)
505 650 823 990 1130 1220 1260 1440 1514 1582
505 589 645 813 852 877 884 923 966 1002 1035 1149 1237 1270 1322 1343 1383 1440 1480 1560
415 477 505 645 813 884 923 966 1022 1140 1176 1278 1465 1503 1560

Figure 5.16 Examples of individual SERS spectra extracted from the mapping datasets of mesenchymal stromal cells for two independent donors (A-B). Control spectra of undifferentiated cells (day 0), spectra of cells differentiated for 7 days and spectra of cells differentiated for 21 days. Excitation wavelength: 785 nm, excitation intensity: 6.0×10^5 W/cm^2, acquisition time: 3s. Scale bars: 50 cps. *Reprinted with permission from [222].*

In addition, some representative SERS spectra from day 14 and 28 of differentiation are shown in Figure 5.17. In accordance with previous SERS spectra for other days of differentiation, they show a high variability, indicating strong variation in composition in different parts of the cell, although some frequent modes of abundant cell membrane components are widely present, e.g., the bands at 505-524 cm^{-1} of disulfide bridges, 650 cm^{-1} C-C twisting mode of phenylalanine, or 1140 cm^{-1} of C-C stretching in phospholipids. Furthermore, on day 14 the mode of hydroxyapatite at 966 cm^{-1} is widely present in the spectra, indicating that osteogenesis is progressing, and bone matrix mineral maturing. SERS spectra on day 28, however, exhibit lower intensities in all cases. One explanation would be that the cell monolayer on the substrates on day 28 of osteogenic differentiation reached maximum confluency and cells started slowly detaching from the surface, which would explain the overall lower cell signals, as the distance between the molecules and the hot spots on the surface likely increased.

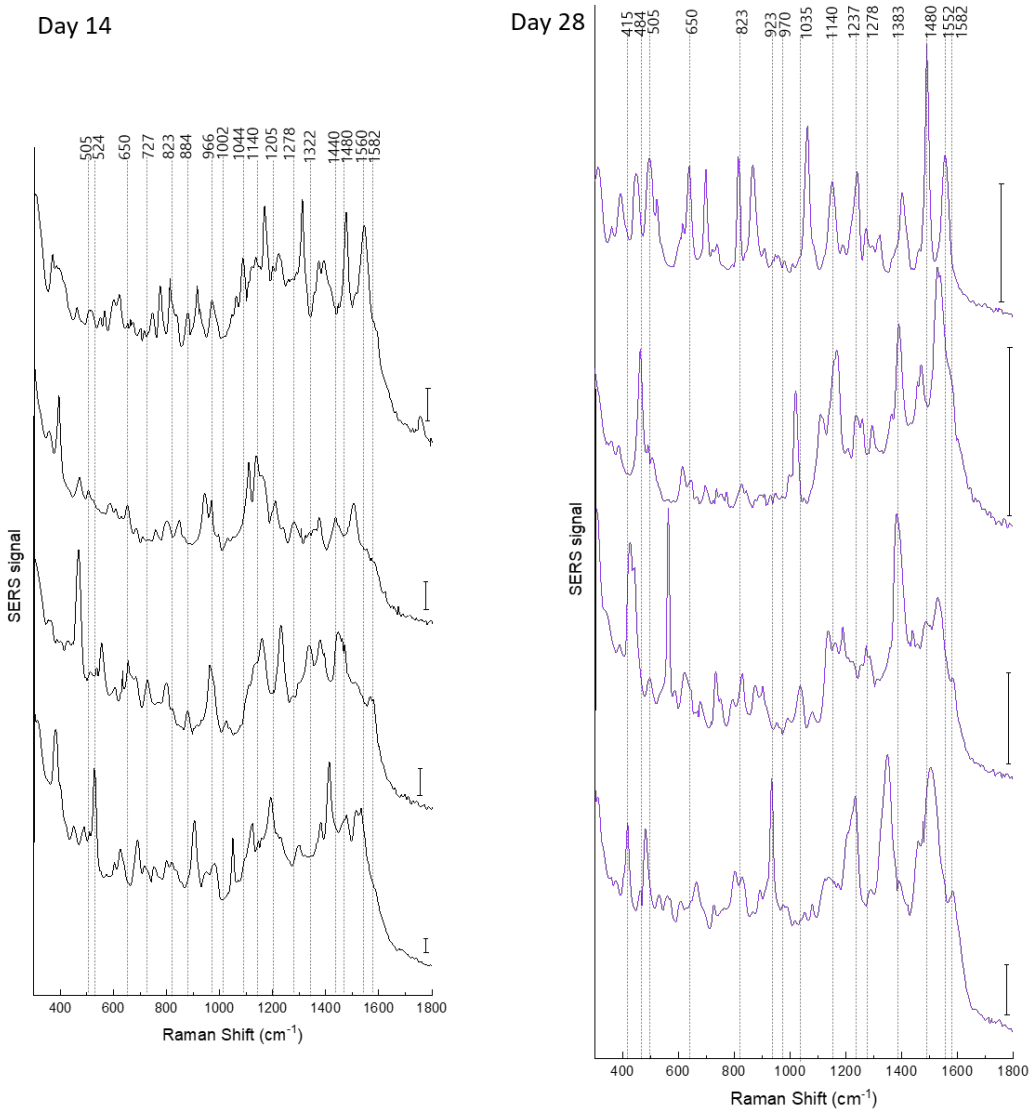

Figure 5.17 Examples of individual SERS spectra extracted from the mapping datasets of mesenchymal stromal cells of cells differentiated for 14 and for 28 days. Excitation wavelength: 785 nm, excitation intensity: 6.0×10^5 W/cm^2, acquisition time: 3s. Scale bars: 50 cps (unpublished data).

5.6.2 SERS mapping of the biochemistry of the cell membrane of the mesenchymal stromal cells during osteogenesis

Averages of SERS spectra are convenient for representation and discussion of big datasets. However, some information might be lost compared to using single SERS spectra, e.g., spectral patterns of low occurrence in the similar vibrational range in large datasets may average out and contribute to one wide band. Thus, single point SERS analysis is especially important in such heterogeneous populations of cells, although the wealth of information might be, at times, overwhelming. To simplify the analysis and at the same time gain insight into the distribution of the intensities of specific vibrational modes, representing the location of respective molecular species, chemical maps can be generated, as shown in Figure 5.18.

As evidenced in the previous study, albeit using formaldehyde as fixative, the respective SERS signal is coming predominantly from the membrane of the adhering cells, due to close vicinity of the outer membrane and extracellular matrix molecules to the underlying nanopatterned gold substrate. In Figure 5.18, the bands at 420 cm^{-1}, 505 cm^{-1}, 856 cm^{-1}, 966 cm^{-1} and 1140 cm^{-1} are displayed, as they represent the allocation of the main components of the cell membrane, i.e., lipids (green maps), proteins (blue maps), as well as the important molecular species of the extracellular matrix deposited during osteogenic differentiation process, i.e., collagen (yellow maps) and calcium phosphate (red maps). The maps at 420 cm^{-1} and 1140 cm^{-1} represent different types of lipids (Figure 5.18 A-B, green maps). The most abundant type of membrane lipids are phospholipids [238] (1140 cm^{-1} phospholipid alkyl chains), therefore the distribution of high intensity pixels in the maps assigned to phospholipids are present throughout the whole culture period, regardless of the day of differentiation as they are the main cell membrane components forming the fluid lipid bilayer. Cholesterol, a small sterol lipid, is embedded in between phospholipids in the membrane bilayer, where it plays an important role in membrane fluidity [226, 249]. Hence, the distribution of high-intensity pixels of the 420 cm^{-1} cholesterol band is comparable to that of the phospholipids. In order to include contributions from many different membrane proteins, the band at 505 cm^{-1} was chosen, which represents the S-S stretching vibration of disulfide bonds, predominantly present on the outer cell membrane, however, not exclusively [240]. The contributions of this band do not particularly change during the differentiation process (blue maps). Production of the extracellular matrix composed mainly of type I collagen and bone matrix proteins [33, 34, 245], which are gradually mineralized with time and form bone nodules embedded in ECM layer, is indicative of the beginning of osteogenic differentiation in BM-MSCs. For this reason, the distribution of intensities of the band at 856 cm^{-1} is also shown, predominantly assigned to amino acid side chains of proline and hydroxyproline [170, 223, 224]. The proteins proline and hydroxyproline are major components of type I collagen and play an important role for collagen stability, which is the base for calcium phosphate deposition. However, at earlier stages of cell proliferation and differentiation, this band can overlap with contributions from ring breathing of the protein tyrosine (823, 830-835 cm^{-1}) as well as (C-O-C) stretching of poly- and monosaccharides at 842-847 cm^{-1} [223, 224, 229]. Also, the extracellular matrix, which contains collagen proteins, is formed during attachment process of the cell to the substrate, therefore the high intensity pixels of this band are present on undifferentiated cells as well [31, 250]. The most widely used mineral vibrational mode of bone tissue is a hydroxyapatite band at 966 cm^{-1}. This band is sensitive to the carbonate (CO_3^{2-}) and monohydrogen phosphate (HPO_4^{2-}) content of the mineral [243]. Freshly deposited hydroxyapatite mineral has a high HPO_4^{2-} content that shifts this vibrational mode to lower frequencies (around 959 cm^{-1}) [223, 224]. Mature bone, containing a crystalline non-substituted hydroxyapatite shifts the band to higher frequencies (966-70 cm^{-1}) [223, 224, 243]. To include as many mineral contributions as possible, the map of hydroxyapatite was constructed based on the integrated intensities of modes between 959 and 970 cm^{-1} (red maps). The hydroxyapatite contributions increase with the progress of differentiation, again in agreement with Alizarin Red S staining (Figure 5.10) – cells on day 21 are much more calcified than cells on day 7. As discussed before, the formation of bone nodules is localized in individual patches and, as bone tissue is a highly complex material, it is clear that its composition will vary in different locations of the cells, depending on the maturation stage and the content of mineral species. Some minor contributions of 966 cm^{-1} vibration can be found on undifferentiated cells, which might be due to the fact that cells can undergo spontaneous differentiation towards the osteogenic pathway, even though osteogenic stimuli were not introduced [251]. This signal could also

be caused by other vibrational contributions around the phosphate region, such as band at 950 cm^{-1} of carbohydrates, which are widely present in the outer cell membrane where glycosylated proteins primarily reside [226].

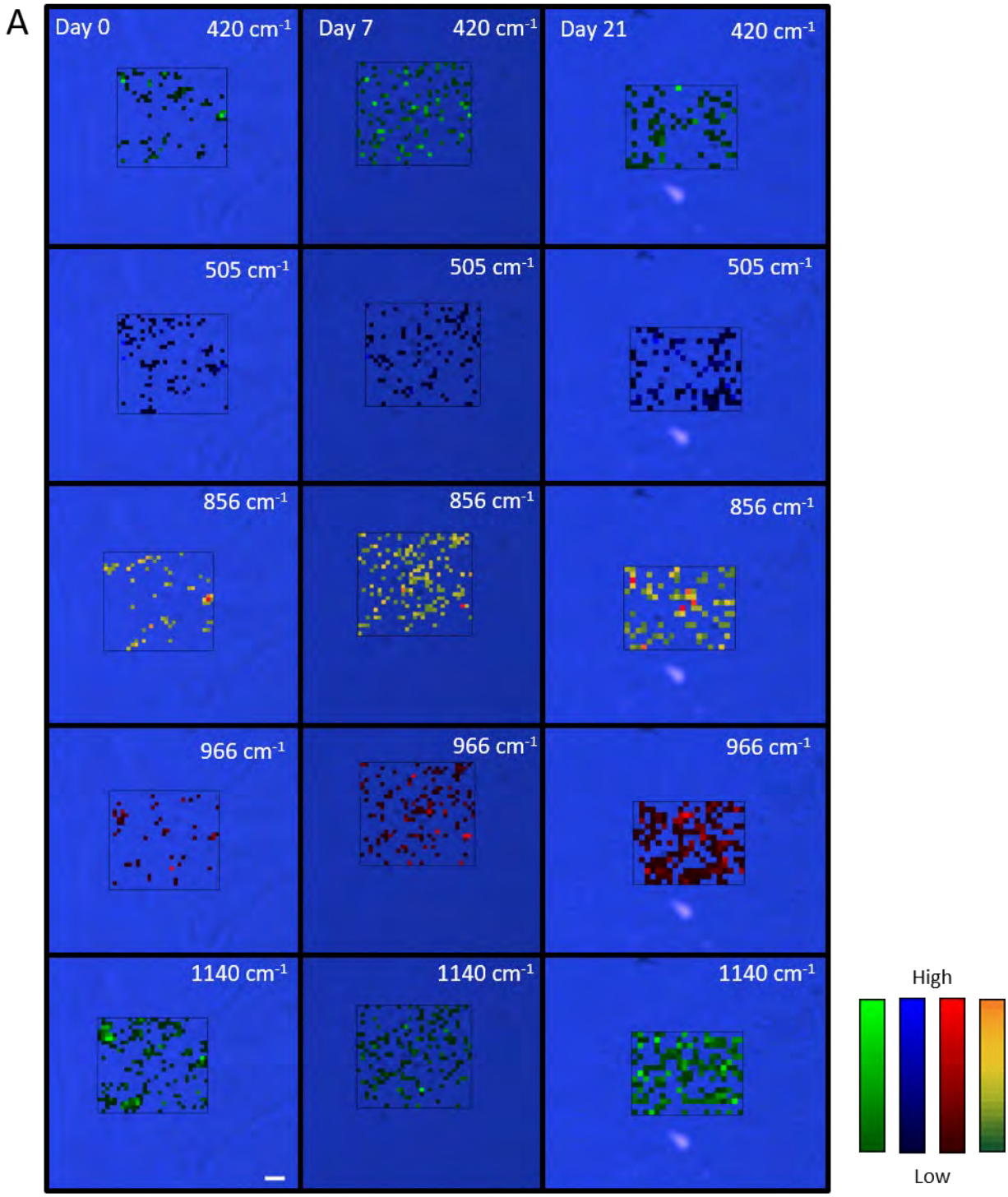

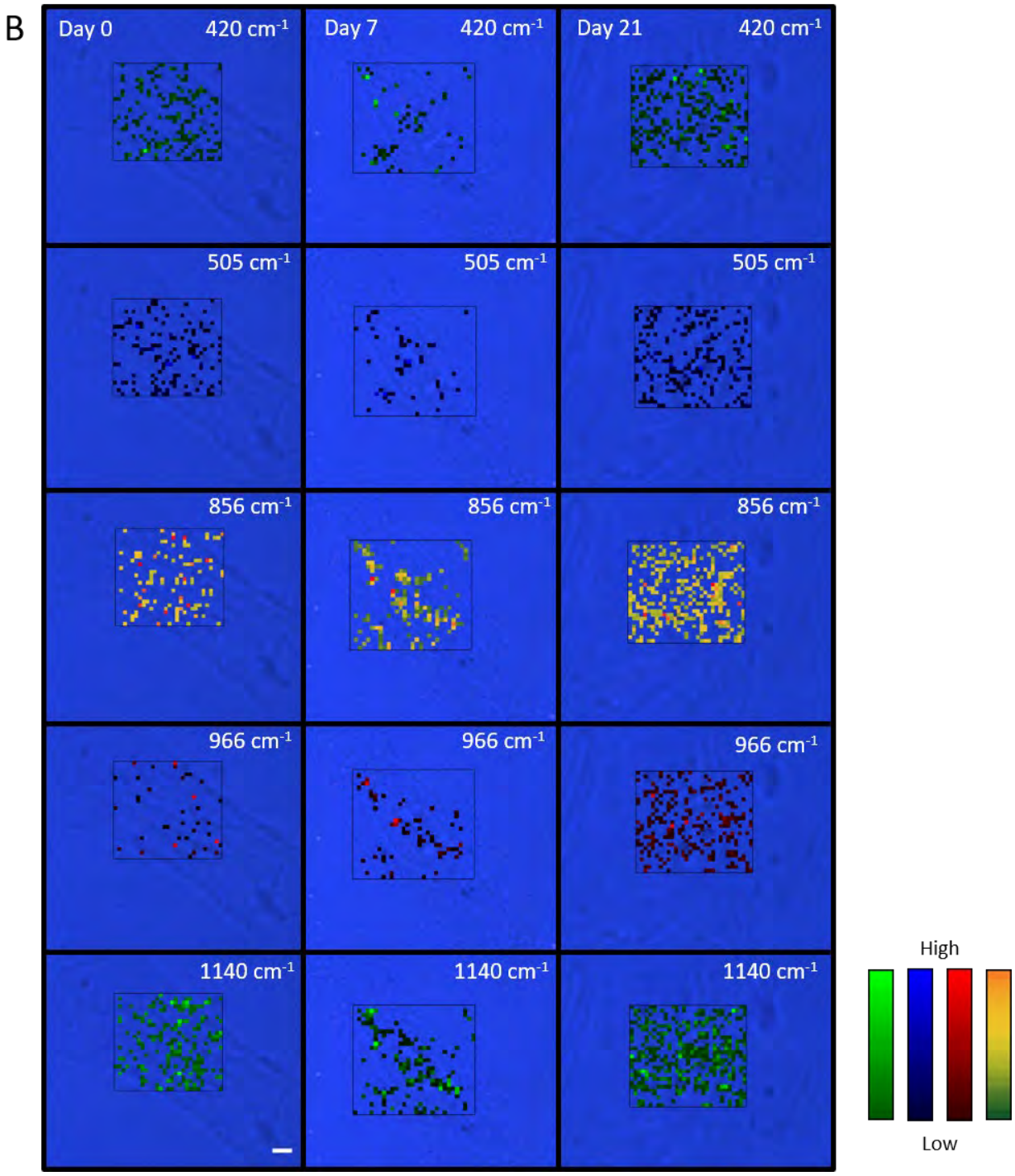

Figure 5.18 Distribution of signals related to molecular species characteristic to cell membrane components present during osteogenic differentiation of mesenchymal stromal cells for two independent donors (A and B). Raman maps are generated by mapping the intensity of the 420 cm^{-1} peak assigned to cholesterol (green), 505 cm^{-1} peak assigned to S-S stretching and disulfide bonds of proteins (blue), 856 cm^{-1} peak mainly assigned to amino acids side chain vibrations of proline, hydroxyproline and C-C vibration of type I collagen (yellow), 966 cm^{-1} peak assigned to calcium hydroxyapatite (red) and 1140 cm^{-1} peak assigned to phospholipid alkyl chains (green). Scale bar: 4 µm. *Reprinted with permission from [222].*

Table 5.3 *Raman shifts and tentative assignments of important bands in the SERS spectra of osteogenic differentiation of BM-MSCs, based on Refs. [49, 52, 168-171, 223, 224, 229, 233, 243, 244, 252, 253]*

Raman shift [cm^{-1}]	**Tentative assignments**
415	CH_2 bending, phosphatidylinositol
420	CH_2 bending in the ring, cholesterol, sterols
430	PO_4^{3-} symmetric stretching vibration, phosphate of HA
477	Polysaccharides (amylase, amylopectin)
484	C-O-C ring deformation, carbohydrates, e.g., glycogen
505/524	S-S disulfide stretching, proteins
589	$v_4PO_4^{3-}$ symmetric stretching vibration (phosphate of HA)
618	C-C twisting, proteins
645-650	C-C twisting mode of phenylalanine, proteins
727	Sterols, ring deformation
742	Tryptophan
813-817	C-C stretching (collagen assignment)
823	Polysaccharides
835	Ring breathing, Tyrosine
847	C-O-C skeletal mode, polysaccharides
852-856	C-C vibration of the collagen backbone, amino acid side chain vibrations of proline and hydroxyproline, hydroxyproline (collagen type I)
884	Proteins, including collagen I
923	Proline, hydroxyproline
960/966/970	PO_4^{3-} symmetric stretching vibration, phosphate of HA, calcium-phosphate stretch band, hydroxyapatite, calcium hydroxyapatite
990	P-O-P stretching, phosphorylated proteins
1002	C-C symmetric stretching, symmetric ring breathing, phenylalanine
1035	Phenylalanine of collagen
1022	Glycogen
1044/1076	$v_3PO_4^{3-}$ symmetric stretching vibration of HA
1123/1128	C-N stretching (proteins), C-O stretching (carbohydrates)
1130	C-C stretching, phospholipids/proteins, Tyrosine
1140	C-C stretching, lipids
1149	Glycogen
1176	C-H bending tyrosine (proteins)
1205	Tyrosine, hydroxyproline (collagen assignment)
1220	Amide III
1237	Amide III and CH_2 wagging vibrations from glycine backbone and proline side chains
1252	Amide III
1260	Amide III, lipids, fatty acids
1278-1280	PO_4^{3-} stretching and amide III, lipids, and proteins
1322	CH_2, CH_3 deformation, CH_3CH_2 twisting, proteins, collagen
1370/1379	CH_2 deformation, lipids
1383	CH_3 deformation, lipids
1418	CO_2^- stretching, amino acids
1440	CH_2 deformation, lipids
1465	CH_2, CH_3 deformation of lipids and collagen
1480-1482	Amide II
1503	-
1514	N-H deformation, proteins
1552-1560	C=C stretching, tryptophan
1572	Amide II, proteins
1582	Phenylalanine

5.7 SERS of live cells

Probing bone marrow-derived mesenchymal stromal cell osteogenic differentiation by SERS can yield comprehensive molecular information on cell membrane biochemistry and reveal changes of the membrane during osteogenesis. Extensive details on MSC differentiation were obtained from studies of fixed cells as presented in the previous chapter. Nevertheless, such an experimental set-up is not ideal, and a live cell probing model would be more practical. In principle, mesenchymal stromal cells are difficult to maintain even in normal cell culturing conditions and several reports suggested that MSCs can be sensitive to, e.g., thermal stress [254] and ionizing radiation [255], which raises the question whether the laser excitation won't cause so-called cell "blebbing" and degradation due to overheating. Moreover, live cells degrade quickly and if they are not provided with adequate temperature and humidity, they may be viable only for some hours. For these reasons, fixing cells at a certain metabolic state in a controlled, long-lasting manner is convenient for SERS studies, as it avoids risking the integrity of the cell. Nevertheless, scientists have attempted to investigate live cells by SERS [5, 162, 231, 234, 256-258], using predominantly SERS probes induced to the culture media before the measurement and choosing more robust cell lines, which are significantly easier to maintain in the culture, less prone to extrinsic factors, and in principle, able to produce repeatable results. Thus, as a first step towards live-cell screening, proof-of-principle experiment on live cell measurements of 3T3 fibroblast cell line were conducted on the gold nanoisland SERS substrates developed in the present work. Results presented here are done with collaboration with Dr. Vesna Živanović and Prof. Janina Kneipp from Humboldt University in Berlin.

5.7.1 SERS spectra from fibroblast cells

Cells from fibroblast cell line 3T3 were seeded on the previously UV-sterilized SERS substrates in 6-well plates and grown for 48 hours to ensure proper attachment. Prior to the measurements, the culture medium consisting of DMEM supplemented with 10% FBS was removed, and cells thoroughly washed with PBS. SERS spectra were obtained in PBS buffer, using a 60× water immersion objective, 785 nm excitation light at the intensity of 1.0×10^5 W/cm^2 and 1 s acquisition time. The observed SERS spectra from the cell mapping experiments reflect the biochemistry of the cell membrane. As shown in previous experiments, SERS substrates probe predominantly the molecules at the interface between the surface of the substrates and the outer cell membrane. In Figure 5.19, average SERS spectra of three individual fibroblast cells are displayed and they broadly resemble the average SERS spectra of undifferentiated BM-MSCs (see Figure 5.15 and Tables 5.2 and 5.3 for assignments), which further indicates that the SERS substrates probe mainly the cell membrane. The most prominent bands that dominate the spectra include modes around 505 cm^{-1} of disulfide bonds, 650 cm^{-1} of C-S stretching in proteins, 1000 cm^{-1} C-C stretching of phenylalanine, 1140 cm^{-1} C-C stretching mode of phospholipids, 1440 cm^{-1} CH_2 deformation of the lipid chains and mode around 1278 cm^{-1} which can be assigned both to lipids and proteins [223, 224, 229, 233]. The average spectra are particularly conclusive regarding the composition of the cell membrane, which is common for many cell types [31, 225, 226], as evidenced by high degree of similarity of the averages from different individual fibroblast cells. Interestingly, pronounced contributions of the modes assigned to the lipid chains in SERS averages, e.g., 1140 cm^{-1}, 1440 cm^{-1} and 1480 cm^{-1} indicate that the live cell is, in fact, closely adhering to the underlying gold surface, since the whole volume of the lipid bilayer is probed, both the polar heads of phospholipids (e.g., 820 cm^{-1} antisymmetric diester

mode of the polar head groups) and phospholipid chains. The fact that lipid modes dominate the spectra, despite their low Raman cross sections as compared to those of proteins [239, 259] means that they must be relatively abundant, what serves as a further confirmation of membrane probing.

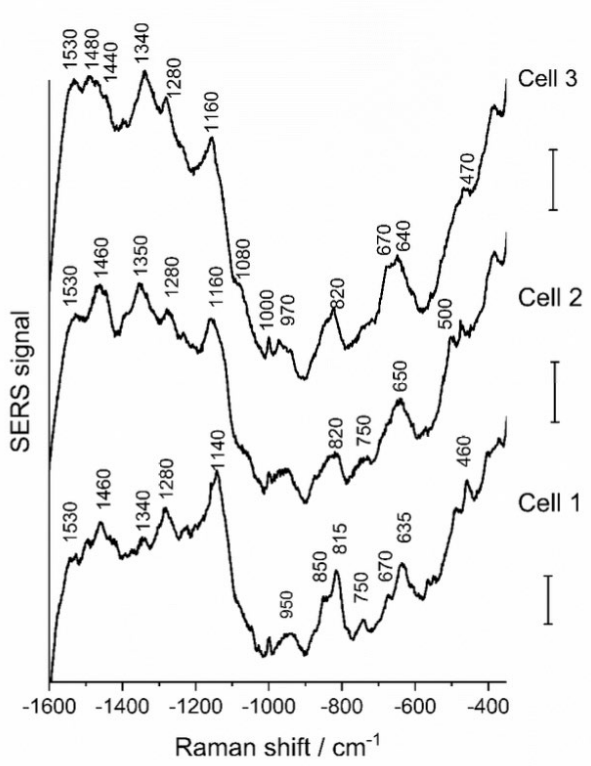

Figure 5.19 Averages of live-cell SERS spectra extracted from the mapping datasets of 3T3 fibroblast cells grown on the gold nanoisland substrates for 48 hours under standard cell culturing conditions. Each spectrum is an average of all SERS spectra measured in one individual cell. Excitation wavelength: 785 nm, acquisition time: 1 s per spectrum, excitation intensity: 1×10^5 W/cm^2. All scale bars: 20 cps. *Reprinted with permission from [260].*

5.7.2 SERS mapping of the biochemistry of fibroblast cell membranes

Some important bands were mapped as chemical images representing the distribution of intensities of selected vibrational modes and overlaid on the corresponding bright-field images of two individual fibroblast cells (Figure 5.20). Each pixel represents one SERS spectrum, which is, in fact, an average of many signals of molecules generated in the vicinity of different hot spots, which are in nm-scale, whereas the diameter of the focused laser spot is in the µm-scale. The distribution of the different lipid components is displayed in chemical maps of typical vibrations of cholesterol (Figure 5.20 A, B all green maps), and the most abundant in the lipid bilayer – phospholipids, i.e., polar head groups (Figure 5.20 A, B all blue maps) and respective lipid chains (Figure 5.20 A, B all pink maps). In the cell membrane bilayer, cholesterol often co-localizes with phospholipids and plays an important role in membrane fluidity [225, 226]. Representative vibrational modes of cholesterol at 420 cm^{-1}, 470 cm^{-1} and 700 cm^{-1} indicate that this molecule is abundant in the cell membrane bilayer. Figure 5.20 C displays three individual SERS spectra from arbitrary positions of the 420

cm^{-1} intensity maps, where the intensity of cholesterol band was high. Moreover, some modes characteristic to phospholipid chains are present in the spectra, further indicating co-localization of these molecules in the membrane. This is well represented by chemical maps of 1070 cm^{-1}, 1090 cm^{-1} and 1130 cm^{-1} assigned to C-C stretching of lipid tails, which correlate closely with intensity bands distribution of cholesterol (compare, e.g., 700 cm^{-1} and 1070 cm^{-1} maps). The distribution of high band intensities related to the polar heads of different phospho- and sphingolipids show that they are localized everywhere across the cell membrane and further exhibit similar distribution to their respective lipid chains (compare blue and pink maps). As shown on chemical maps of 650 cm^{-1} and 1000 cm^{-1} modes assigned to the C-S stretching and to the ring breathing vibration of phenylalanine, respectively, proteins are also widely present in the cell membrane. Phenylalanine can be bound to the cell membrane either by one or more covalently attached lipid groups, which can be either fatty acid chains or prenyl groups [31, 225], suggesting that both (cytosolic and non-cytosolic) sides of the membrane can be probed. This is further evidenced by the co-occurrence of the high intensity modes of proteins and lipid tails (compare, e.g., 1000 cm^{-1} and 1130 cm^{-1} maps), pointing out to complex interactions of the molecules within the cell membrane.

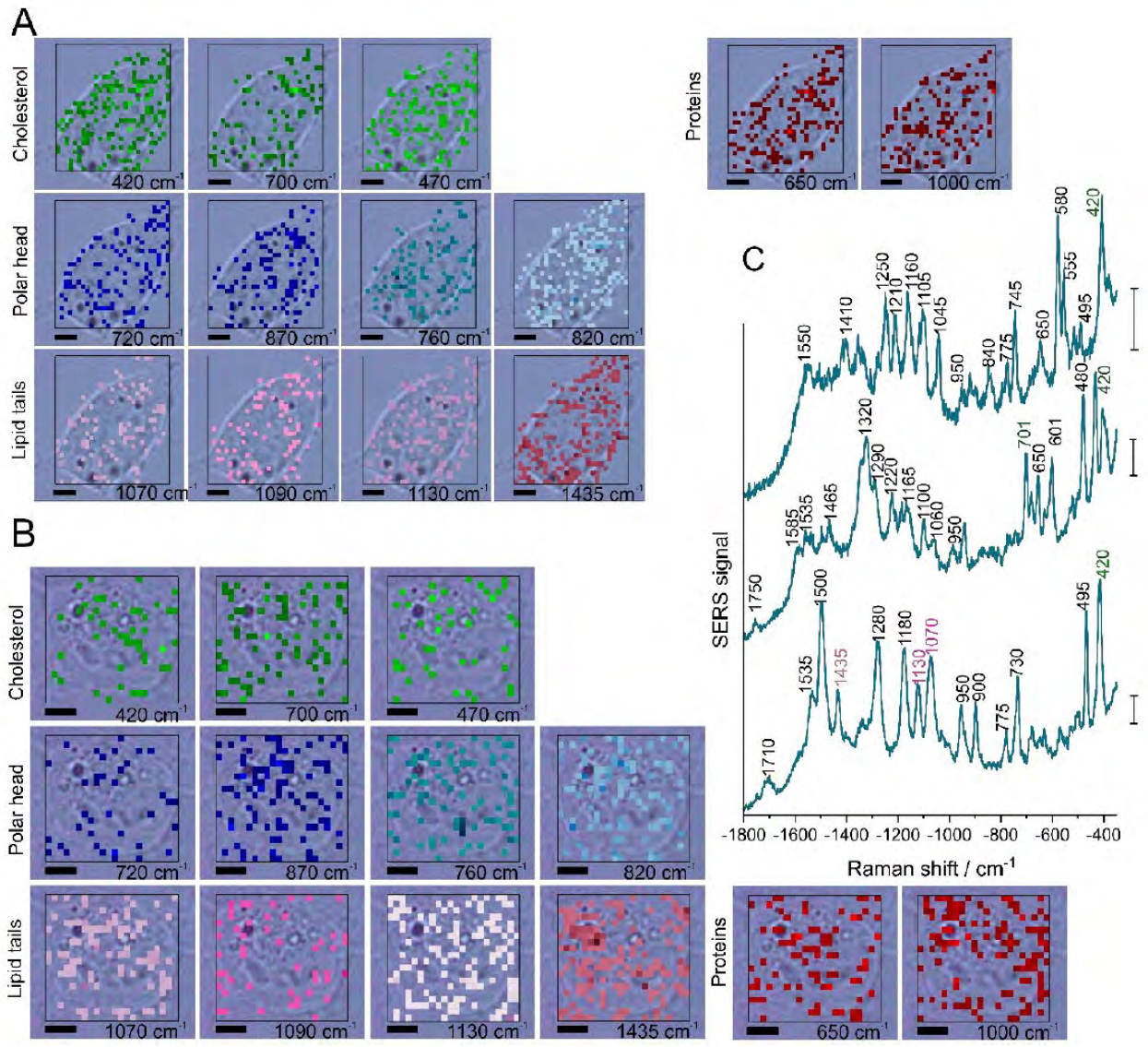

Figure 5.20 Distribution of characteristic SERS signals related to the components of the cellular membrane in two different cells cultured on the SERS substrates, overlaid with a bright field image (A, B). Chemical images are generated by mapping the intensity of the bands at 420 cm^{-1} and 700 cm^{-1} assigned to cholesterol, 720 cm^{-1} and 870 cm^{-1} to C–N stretching of choline group, 760 cm^{-1} to the ethanolamine group in phosphatidylethanolamine, 820 cm^{-1} to phosphate group in phospholipids, 1070 cm^{-1}, 1090 cm^{-1}, and 1130 cm^{-1} to C–C stretching of lipid tails, 1435 cm^{-1} to CH_2, CH_3 deformations of alkyl chains, 650 cm^{-1} to C–S stretching in proteins, 1000 cm^{-1} to phenylalanine. All Scale bars: 5 μm. (C) Examples of SERS spectra extracted from the chemical images generated by mapping the intensity of the band at 420 cm^{-1}. Excitation wavelength: 785 nm, acquisition time: 1 s per spectrum, excitation intensity: 1×10^5 W/cm^2. All scale bars: 50 cps. *Reprinted with permission from [260].*

The data shown in this chapter demonstrate the possibility to study the molecular structure and dynamics of cell membranes of living fibroblast cells cultured on gold nanoisland substrates by SERS. A comperhensive description of interactions between different membrane components, as well as state-of-order of respective molecules is further elucidated in the paper, however, it's beyond the scope of this thesis. Importantly, live studies of fibroblast cell line on the gold nanoisland substrates confirmed that the optical excitation conditions used in the present work do not adversely affect live cells, paving a way towards long-term live cell studies of mesenchymal stromal cells.

Chapter 6

Summary and conclusions

This thesis has focused on implementation of a simple, sensitive, uniform, and biocompatible SERS platform for monitoring changes in molecular composition of cell membranes. Its usefulness has been demonstrated in the study of mesenchymal stromal cell differentiation and in live-cell Raman imaging.

A simple electron-beam evaporation of gold on glass, combined with thermal annealing, was employed as a method to fabricate relatively flat gold nanoisland substrates providing uniform SERS enhancement. The results from both experiments and FDTD simulations confirmed that the enhancement depended on the size distribution of the island particles, as well as on their spatial arrangement on the substrates, in particular, on the size of the gaps between respective particles. Despite not yielding extreme signal amplifications, the resulting enhancement was sufficient to significantly increase the Raman signals of the studied cells. The flat surface of the SERS substrates was shown to ensure high degree of cell attachment to the underlying surface, which is a key factor in the utilization of electromagnetic enhancement, being a distance dependent process. Furthermore, as the substrates do not possess any sharp edges that could potentially breach the cell membrane structure, cell culturing on such platforms can be considered non-disruptive, contrary to, e.g., SERS investigations of cell components by internalization of gold nanoparticles.

Although there are some controversies around nanotoxicity of gold and its use in cellular investigations, indicating that gold can disrupt gene expression and consequently lead to cell apoptosis, the results of viability assays showed no significant differences in quality of cell proliferation nor differentiation of mesenchymal stromal cells on the developed substrates, as compared to glass slides. Even though initially less cells attach to the SERS surfaces, as compared to glass, which results in lower number of cells on SERS substrates throughout the duration of the cell culture, the morphology of the cells and their ability to differentiate was not compromised. This further points out that SERS substrates consisting of thin gold films are, in fact, biocompatible and can be used as sensitive, sensing platforms for non-invasive, label-free detection of molecular species of the studied cells. In addition, long-term proliferation and differentiation of mesenchymal stromal cells on SERS substrates was evaluated and the results specifically showed that the substrates do not adversely affect the cells. This is a key aspect of the experimental setup, as cells are exposed to the substrates from the beginning, meaning that before the SERS measurements no additional elements, that could influence the cell behavior, will enter the system. In contrast, in traditional SERS experiments when SERS nanoparticles are internalized, they are usually introduced to the cells just before the measurements, disturbing the cell state of equilibrium, causing, e.g.,

oxidative stress, which might reflect in the results. The possibility of seeding cells on SERS sensing platforms is of particular importance in live cell studies of mesenchymal stromal cells, which are prone to extrinsic factors, further indicating that exposing cells to the SERS substrates from the beginning represents a promising approach to improve reproducibility of the results.

The application of SERS substrates for the detection and chemical analysis of the components of the cell membranes of mesenchymal stromal cells has been demonstrated. The results imply that the substrate selectively probes the outer cell membrane and the extracellular matrix components that have been deposited by the cell on the interface between the gold nanoisland surface and cell membrane. The most prominent bands present in the SERS spectra of MSCs were chiefly assigned to carbohydrates, proteins, and lipids (both phospholipid heads and tails). The fact that lipid chains, which are rather present on the inner side of the cell membrane bilayer, can be probed indicates that the cells must tightly adhere to the gold surface. Moreover, the widely present bands associated with vibrational modes of lipids, despite their small Raman cross sections compared to those of proteins, further suggest that lipids must be abundant within the sensing volume, confirming out that signals are mainly detected from the cell membrane. The simultaneous mapping of many molecular constituents in individual cells allowed for visualization of spatial distribution of the molecules forming membrane bilayers, indicating that chemical events occurring in the cell membrane can be followed by SERS. Conversely, signals that could be associated with the cellular interior molecules, such as DNA, were either absent or negligible in SERS spectra. This approach is useful in limiting the complexity of SERS data and for extracting information relevant for, e.g., studying mesenchymal stromal cell differentiation, occurring predominantly on the outer cell membrane.

Osteogenic differentiation of mesenchymal stromal cell cultured on gold nanoisland substrates was carried out for two independent donors and was followed for 28 days. The important timepoints were mapped and results compared with undifferentiated cells. The data showed significant changes occurring on the cell membrane and extracellular matrix, which highlighted the diversity in mineral crystallinity of bone tissue within the cell population, but also within single cell, indicating that the process of bone formation and differentiation itself is complex and, more importantly, heterogeneous. These results correlate particularly well with the Alizarin Red S staining, that clearly shows the diversity of osteogenesis, which occurs in individual patches, depending on the maturation stage and the content of mineral species. SERS data obtained from differentiated cells were compared with each other and with SERS data from undifferentiated cells and, based on the analysis, it can be proposed that SERS alone is sufficient to monitor the progress of extracellular matrix development and osteoblasts formation. However, the results clearly show that osteogenic differentiation is far from being uniform and it is evidently not enough to report on intensity changes in the most prominent mode of hydroxyapatite, which is considered the marker band for osteogenesis, as each cell seems to undergo differentiation differently, at its own pace. The same goes for displaying averages of SERS spectra, which surely gives a great overview of the level of differentiation within one cell, or within cell population, but it simultaneously diminishes the information delivered by single-point SERS analysis. Even though the probing area is confined to the cell membrane, the wealth of information is still elaborate. The observed results slightly contradict with the previously reported studies on osteogenesis, where the hydroxyapatite peak at 966 cm^{-1} indeed shifts in position depending on the degree of bone maturation, but also increases in intensity, indicating that

hydroxyapatite eventually dominates the spectra, and consequently is the most abundant on the cell membrane. This is not the case in the present study, where this mode is obviously widely occurring in the spectra, but never exceeds the signals of lipids or proteins. These results might be controversial, but they undoubtedly demonstrate that monitoring and characterizing differentiation of such heterogeneous populations of cells is not always straightforward.

Although these preliminary experiments were performed on fixed cells, to minimize the risk of unexpected cell damage during long-term process of differentiation, it was demonstrated that live cell measurements of more robust fibroblast cell line cultured on the gold nanoisland substrates was also possible. However, in order to fully exploit the potential of long-term live cell screening and visualization of differentiation or other cellular processes, the Raman microscope should be equipped with an incubator to maintain the optimal cell culturing conditions over extended periods of time. This type of advanced equipment was not available within the present project. The combined results of the present project indicate, however, that the osteogenic differentiation process of live mesenchymal stromal cells cultured on gold nanoisland substrates can be monitored by SERS.

Surface-enhanced Raman scattering with gold nanoisland substrates offers a unique approach to study biochemistry, but also biophysics, through the study of the molecular composition of the cell membranes, paving a way towards non-invasive studies of cells and their processes. In the future, it is desirable to show whether such an approach is feasible to study numerous cell processes, e.g., apoptosis, cancer detection, or differentiation into other tissue types, such as adipocytes or chondrocytes, ultimately in a live cell setup. Ideally, stem cells originating from several donors should be investigated, to confirm repeatability and adequacy of the results, bringing researchers closer to better understanding of these heterogeneous cell populations. Moreover, cell membrane dynamics can be detected by SERS, as the conformation of molecular bonds and their state-of-order are reflected in the SERS spectra. By analyzing the spatial distribution of atoms within the molecule and the conformational changes caused, presumably, by some extrinsic factors, such as temperature, humidity, or nutrition adjustments in the culturing environment over time, one could yield information on preferred cell culturing conditions and feeding strategies, leading to better quality of proliferation and differentiation.

Some future improvements to the presently developed SERS substrates can be envisioned. For instance, the substrate fabrication procedure could be improved further in order to generate higher enhancement leading to potential detection of molecules with smaller Raman cross sections or of low quantity. In the SERS field, it is no longer a big challenge to obtain enhancement factors of the order of 10^{11}. However, achieving this uniformly over large areas is not quite simple. Therefore, there must always be a compromise between high enhancements and uniformity of substrates, the latter being significantly more important in biological studies. In addition, the thermal-, chemical- and photo-stability of the substrates during storage and measurements should be evaluated. Especially, in case where studied samples on SERS substrates are irradiated with high laser powers and/or long acquisition times, one should be cautious not only about the sample photodegradation, but also substrate photodegradation, which can lead to gold particle coalescence due to local sample heating.

Thus far, SERS has mostly been used for identification and discrimination purposes, rather than for quantitative analyses due to the complexity and wealth of information that can be derived from SERS. Simultaneously, however, more advanced data preprocessing and

multivariate analyses are being developed, along with machine learning approaches. Combining SERS substrates with high sensitivity and reproducibility, with appropriate detection environments for cells, retaining their native states, improved SERS biomolecule databases and implementing multivariate analyses as an approach to translate the complex spectral information into quantitative data, this particular SERS protocol may contribute to answering different important biological questions in the future.

References

1. M. Fleischmann, P. J. Hendra, and A. J. McQuillan, "Raman spectra of pyridine adsorbed at a silver electrode," Chem Phys Lett **26**, 163-166 (1974).
2. K. Kneipp, Y. Wang, H. Kneipp, L. T. Perelman, I. Itzkan, R. R. Dasari, and M. S. Feld, "Single Molecule Detection Using Surface-Enhanced Raman Scattering (SERS)," Physical Review Letters **78**, 1667-1670 (1997).
3. S. Nie and S. R. Emory, "Probing Single Molecules and Single Nanoparticles by Surface-Enhanced Raman Scattering," Science **275**, 1102-1106 (1997).
4. K. Kneipp, H. Kneipp, I. Itzkan, R. R. Dasari, and M. S. Feld, "Surface-enhanced Raman scattering and biophysics," Journal of Physics-Condensed Matter **14**, R597-R624 (2002).
5. J. Kneipp, H. Kneipp, A. Rajadurai, R. W. Redmond, and K. Kneipp, "Optical probing and imaging of live cells using SERS labels," J Raman Spectrosc **40**, 1-5 (2009).
6. W. L. Barnes, A. Dereux, and T. W. Ebbesen, "Surface plasmon subwavelength optics," Nature **424**, 824-830 (2003).
7. S. A. Maier and H. A. Atwater, "Plasmonics: Localization and guiding of electromagnetic energy in metal/dielectric structures," Journal of Applied Physics **98**(2005).
8. J. A. Dieringer, A. D. McFarland, N. C. Shah, D. A. Stuart, A. V. Whitney, C. R. Yonzon, M. A. Young, X. Zhang, and R. P. Van Duyne, "Surface enhanced Raman spectroscopy: new materials, concepts, characterization tools, and applications," Faraday Discuss **132**, 9-26 (2006).
9. X. M. Lin, Y. Cui, Y. H. Xu, B. Ren, and Z. Q. Tian, "Surface-enhanced Raman spectroscopy: substrate-related issues," Anal Bioanal Chem **394**, 1729-1745 (2009).
10. T. K. Sau and C. J. Murphy, "Room temperature, high-yield synthesis of multiple shapes of gold nanoparticles in aqueous solution," J Am Chem Soc **126**, 8648-8649 (2004).
11. W. Cai, T. Gao, H. Hong, and J. Sun, "Applications of gold nanoparticles in cancer nanotechnology," Nanotechnol Sci Appl **1**, 17-32 (2008).
12. Z. Yang, Q. Li, F. Ruan, Z. Li, B. Ren, H. Xu, and Z. Tian, "FDTD for plasmonics: Applications in enhanced Raman spectroscopy," Chinese Science Bulletin **55**, 2635-2642 (2010).
13. Z. Zeng, Y. Liu, and J. Wei, "Recent advances in surface-enhanced raman spectroscopy (SERS): Finite-difference time-domain (FDTD) method for SERS and sensing applications," TrAC Trends in Analytical Chemistry **75**, 162-173 (2016).
14. G. S. Bumbrah and R. M. Sharma, "Raman spectroscopy – Basic principle, instrumentation and selected applications for the characterization of drugs of abuse," Egyptian Journal of Forensic Sciences **6**, 209-215 (2016).
15. R. Smith, K. L. Wright, and L. Ashton, "Raman spectroscopy: an evolving technique for live cell studies," Analyst **141**, 3590-3600 (2016).

16. M. Moskovits, "Surface-enhanced spectroscopy," Reviews of Modern Physics **57**, 783-826 (1985).
17. M. Moskovits, "Surface roughness and the enhanced intensity of Raman scattering by molecules adsorbed on metals," The Journal of Chemical Physics **69**, 4159-4161 (1978).
18. E. C. Le Ru, P. G. Etchegoin, and M. Meyer, "Enhancement factor distribution around a single surface-enhanced Raman scattering hot spot and its relation to single molecule detection," J Chem Phys **125**, 204701 (2006).
19. T. Vo-Dinh, "Surface-enhanced Raman spectroscopy using metallic nanostructures," TrAC Trends in Analytical Chemistry **17**, 557-582 (1998).
20. C. Krafft, M. Schmitt, I. W. Schie, D. Cialla-May, C. Matthaus, T. Bocklitz, and J. Popp, "Label-Free Molecular Imaging of Biological Cells and Tissues by Linear and Nonlinear Raman Spectroscopic Approaches," Angew Chem Int Ed Engl **56**, 4392-4430 (2017).
21. D. Lahnemann, J. Koster, E. Szczurek, D. J. McCarthy, S. C. Hicks, M. D. Robinson, C. A. Vallejos, K. R. Campbell, N. Beerenwinkel, A. Mahfouz, L. Pinello, P. Skums, A. Stamatakis, C. S. Attolini, S. Aparicio, J. Baaijens, M. Balvert, B. Barbanson, A. Cappuccio, G. Corleone, B. E. Dutilh, M. Florescu, V. Guryev, R. Holmer, K. Jahn, T. J. Lobo, E. M. Keizer, I. Khatri, S. M. Kielbasa, J. O. Korbel, A. M. Kozlov, T. H. Kuo, B. P. F. Lelieveldt, Mandoiu, II, J. C. Marioni, T. Marschall, F. Molder, A. Niknejad, L. Raczkowski, M. Reinders, J. Ridder, A. E. Saliba, A. Somarakis, O. Stegle, F. J. Theis, H. Yang, A. Zelikovsky, A. C. McHardy, B. J. Raphael, S. P. Shah, and A. Schonhuth, "Eleven grand challenges in single-cell data science," Genome Biol **21**, 31 (2020).
22. I. R. Suhito, Y. Han, J. Min, H. Son, and T. H. Kim, "In situ label-free monitoring of human adipose-derived mesenchymal stem cell differentiation into multiple lineages," Biomaterials **154**, 223-233 (2018).
23. B. Kann, H. L. Offerhaus, M. Windbergs, and C. Otto, "Raman microscopy for cellular investigations--From single cell imaging to drug carrier uptake visualization," Adv Drug Deliv Rev **89**, 71-90 (2015).
24. P. Arpornmaeklong, S. E. Brown, Z. Wang, and P. H. Krebsbach, "Phenotypic characterization, osteoblastic differentiation, and bone regeneration capacity of human embryonic stem cell-derived mesenchymal stem cells," Stem Cells Dev **18**, 955-968 (2009).
25. C. M. McLeod and R. L. Mauck, "On the origin and impact of mesenchymal stem cell heterogeneity: new insights and emerging tools for single cell analysis," Eur Cell Mater **34**, 217-231 (2017).
26. C. De Schauwer, E. Meyer, G. R. Van de Walle, and A. Van Soom, "Markers of stemness in equine mesenchymal stem cells: a plea for uniformity," Theriogenology **75**, 1431-1443 (2011).
27. C. Geraldes, "Introduction to Infrared and Raman-Based Biomedical Molecular Imaging and Comparison with Other Modalities," Molecules **25**(2020).
28. E. Dumont, C. De Bleye, P. Y. Sacre, L. Netchacovitch, P. Hubert, and E. Ziemons, "From near-infrared and Raman to surface-enhanced Raman spectroscopy: progress, limitations and perspectives in bioanalysis," Bioanalysis **8**, 1077-1103 (2016).
29. J. Kneipp, H. Kneipp, M. McLaughlin, D. Brown, and K. Kneipp, "In vivo molecular probing of cellular compartments with gold nanoparticles and nanoaggregates," Nano Lett **6**, 2225-2231 (2006).

30. R. Pilot, R. Signorini, C. Durante, L. Orian, M. Bhamidipati, and L. Fabris, "A Review on Surface-Enhanced Raman Scattering," Biosensors (Basel) **9**(2019).
31. B. Alberts, J. H. Wilson, and T. Hunt, *Molecular biology of the cell*, 5th ed. (Garland Science, New York, 2008), pp. xxxiii, 1601, 1690 p.
32. F. Long, "Building strong bones: molecular regulation of the osteoblast lineage," Nat Rev Mol Cell Biol **13**, 27-38 (2011).
33. J. E. Aubin, "Bone stem cells," Journal of Cellular Biochemistry **72**, 73-82 (1998).
34. X. Lin, S. Patil, Y. G. Gao, and A. Qian, "The Bone Extracellular Matrix in Bone Formation and Regeneration," Front Pharmacol **11**, 757 (2020).
35. A. Wilson, A. Webster, and P. Genever, "Nomenclature and heterogeneity: consequences for the use of mesenchymal stem cells in regenerative medicine," Regen Med **14**, 595-611 (2019).
36. A. Wilson, M. Hodgson-Garms, J. E. Frith, and P. Genever, "Multiplicity of Mesenchymal Stromal Cells: Finding the Right Route to Therapy," Front Immunol **10**, 1112 (2019).
37. D. Sipp, P. G. Robey, and L. Turner, "Clear up this stem-cell mess," Nature **561**, 455-457 (2018).
38. C. V. Raman, "A Change of Wave-length in Light Scattering," Nature **121**, 619-619 (1928).
39. C. V. Raman and K. S. Krishnan, "A New Type of Secondary Radiation," Nature **121**, 501-502 (1928).
40. G. Landsberg and L. Mandelstam, "Über die Lichtzerstreuung in Kristallen," Zeitschrift für Physik **50**, 769-780 (1928).
41. R. Singh, "The 90th Anniversary of the Raman Effect," Indian Journal of History of Science **53**(2018).
42. A. Smekal, "Zur Quantentheorie der Dispersion," Die Naturwissenschaften **11**, 873-875 (1923).
43. R. R. Jones, D. C. Hooper, L. Zhang, D. Wolverson, and V. K. Valev, "Raman Techniques: Fundamentals and Frontiers," Nanoscale Res Lett **14**, 231 (2019).
44. D. W. Shipp, F. Sinjab, and I. Notingher, "Raman spectroscopy: techniques and applications in the life sciences," Adv Opt Photonics **9**, 315-428 (2017).
45. E. V. Efremov, F. Ariese, and C. Gooijer, "Achievements in resonance Raman spectroscopy review of a technique with a distinct analytical chemistry potential," Anal Chim Acta **606**, 119-134 (2008).
46. B. Brozek-Pluska, J. Musial, R. Kordek, E. Bailo, T. Dieing, and H. Abramczyk, "Raman spectroscopy and imaging: applications in human breast cancer diagnosis," Analyst **137**, 3773-3780 (2012).
47. H. Abramczyk, A. Imiela, and A. Śliwińska, "Novel strategies of Raman imaging for exploring cancer lipid reprogramming," Journal of Molecular Liquids **274**, 52-59 (2019).
48. A. Ghita, F. C. Pascut, V. Sottile, C. Denning, and I. Notingher, "Applications of Raman micro-spectroscopy to stem cell technology: label-free molecular discrimination and monitoring cell differentiation," EPJ Tech Instrum **2**, 6 (2015).
49. L. L. McManus, G. A. Burke, M. M. McCafferty, P. O'Hare, M. Modreanu, A. R. Boyd, and B. J. Meenan, "Raman spectroscopic monitoring of the osteogenic differentiation of human mesenchymal stem cells," Analyst **136**, 2471-2481 (2011).
50. P. S. Hung, Y. C. Kuo, H. G. Chen, H. H. Chiang, and O. K. Lee, "Detection of osteogenic differentiation by differential mineralized matrix production in mesenchymal stromal cells by Raman spectroscopy," PLoS One **8**, e65438 (2013).

51. Y. Gao, C. Xu, and L. Wang, "Non-invasive monitoring of the osteogenic differentiation of human mesenchymal stem cells on a polycaprolactone scaffold using Raman imaging," RSC Advances **6**, 61771-61776 (2016).
52. A. D. Hofemeier, H. Hachmeister, C. Pilger, M. Schurmann, J. F. Greiner, L. Nolte, H. Sudhoff, C. Kaltschmidt, T. Huser, and B. Kaltschmidt, "Label-free nonlinear optical microscopy detects early markers for osteogenic differentiation of human stem cells," Sci Rep **6**, 26716 (2016).
53. R. J. Swain, G. Jell, and M. M. Stevens, "Non-invasive analysis of cell cycle dynamics in single living cells with Raman micro-spectroscopy," J Cell Biochem **104**, 1427-1438 (2008).
54. A. Zoladek, F. C. Pascut, P. Patel, and I. Notingher, "Non-invasive time-course imaging of apoptotic cells by confocal Raman micro-spectroscopy," J Raman Spectrosc **42**, 251-258 (2011).
55. M. Okada, N. I. Smith, A. F. Palonpon, H. Endo, S. Kawata, M. Sodeoka, and K. Fujita, "Label-free Raman observation of cytochrome c dynamics during apoptosis," Proc Natl Acad Sci U S A **109**, 28-32 (2012).
56. A. Ali, Y. Abouleila, Y. Shimizu, E. Hiyama, T. M. Watanabe, T. Yanagida, and A. Germond, "Single-Cell Screening of Tamoxifen Abundance and Effect Using Mass Spectrometry and Raman-Spectroscopy," Anal Chem **91**, 2710-2718 (2019).
57. I. W. Schie and T. Huser, "Methods and Applications of Raman Microspectroscopy to Single-Cell Analysis," Applied Spectroscopy **67**, 813-828 (2013).
58. V. Charwat, K. Schutze, W. Holnthoner, A. Lavrentieva, R. Gangnus, P. Hofbauer, C. Hoffmann, B. Angres, and C. Kasper, "Potential and limitations of microscopy and Raman spectroscopy for live-cell analysis of 3D cell cultures," J Biotechnol **205**, 70-81 (2015).
59. A. F. Palonpon, M. Sodeoka, and K. Fujita, "Molecular imaging of live cells by Raman microscopy," Curr Opin Chem Biol **17**, 708-715 (2013).
60. C. Matthaus, B. Bird, M. Miljkovic, T. Chernenko, M. Romeo, and M. Diem, "Chapter 10: Infrared and Raman microscopy in cell biology," Methods Cell Biol **89**, 275-308 (2008).
61. M. D'Acunto, R. Gaeta, R. Capanna, and A. Franchi, "Contribution of Raman Spectroscopy to Diagnosis and Grading of Chondrogenic Tumors," Sci Rep **10**, 2155 (2020).
62. H. Abramczyk, B. Brozek-Pluska, A. Jarota, J. Surmacki, A. Imiela, and M. Kopec, "A look into the use of Raman spectroscopy for brain and breast cancer diagnostics: linear and non-linear optics in cancer research as a gateway to tumor cell identity," Expert Rev Mol Diagn **20**, 99-115 (2020).
63. D. L. Jeanmaire and R. P. Van Duyne, "Surface raman spectroelectrochemistry," Journal of Electroanalytical Chemistry and Interfacial Electrochemistry **84**, 1-20 (1977).
64. M. G. Albrecht and J. A. Creighton, "Anomalously Intense Raman-Spectra of Pyridine at a Silver Electrode," Journal of the American Chemical Society **99**, 5215-5217 (1977).
65. A. Pinczuk and E. Burstein, "Raman Scattering from InSb Surfaces at Photon Energies Near theE1Energy Gap," Physical Review Letters **21**, 1073-1075 (1968).
66. M. R. Philpott, "Effect of surface plasmons on transitions in molecules," The Journal of Chemical Physics **62**, 1812-1817 (1975).

67. M. Moskovits, "How the localized surface plasmon became linked with surface-enhanced Raman spectroscopy," Notes and Records of the Royal Society **66**, 195-203 (2012).
68. J. P. Su, Y. T. Lee, S. Y. Lu, and J. S. Lin, "Chemical mechanism of surface-enhanced Raman scattering spectrum of pyridine adsorbed on Ag cluster: ab initio molecular dynamics approach," J Comput Chem **34**, 2806-2815 (2013).
69. E. A. Stern and R. A. Ferrell, "Surface Plasma Oscillations of a Degenerate Electron Gas," Physical Review **120**, 130-136 (1960).
70. U. Kreibig and P. Zacharias, "Surface plasma resonances in small spherical silver and gold particles," Zeitschrift für Physik A Hadrons and nuclei **231**, 128-143 (1970).
71. M. Moskovits, "Surface-enhanced Raman spectroscopy: a brief retrospective," J Raman Spectrosc **36**, 485-496 (2005).
72. P. L. Stiles, J. A. Dieringer, N. C. Shah, and R. P. Van Duyne, "Surface-enhanced Raman spectroscopy," Annu Rev Anal Chem (Palo Alto Calif) **1**, 601-626 (2008).
73. J. F. Masson, "Portable and field-deployed surface plasmon resonance and plasmonic sensors," Analyst **145**, 3776-3800 (2020).
74. G. C. Schatz, M. A. Young, and R. P. Van Duyne, "Electromagnetic Mechanism of SERS," in *Surface-Enhanced Raman Scattering: Physics and Applications*, K. Kneipp, M. Moskovits, and H. Kneipp, eds. (Springer Berlin Heidelberg, Berlin, Heidelberg, 2006), pp. 19-45.
75. S. Y. Ding, E. M. You, Z. Q. Tian, and M. Moskovits, "Electromagnetic theories of surface-enhanced Raman spectroscopy," Chem Soc Rev **46**, 4042-4076 (2017).
76. J. Kneipp, H. Kneipp, and K. Kneipp, "SERS--a single-molecule and nanoscale tool for bioanalytics," Chem Soc Rev **37**, 1052-1060 (2008).
77. M. Kerker, O. Siiman, L. A. Bumm, and D. S. Wang, "Surface enhanced Raman scattering (SERS) of citrate ion adsorbed on colloidal silver," Appl Opt **19**, 3253-3255 (1980).
78. D. S. Wang and M. Kerker, "Enhanced Raman scattering by molecules adsorbed at the surface of colloidal spheroids," Physical Review B **24**, 1777-1790 (1981).
79. K. L. Kelly, E. Coronado, L. L. Zhao, and G. C. Schatz, "The Optical Properties of Metal Nanoparticles: The Influence of Size, Shape, and Dielectric Environment," The Journal of Physical Chemistry B **107**, 668-677 (2003).
80. A. Otto, "The 'chemical' (electronic) contribution to surface-enhanced Raman scattering," J Raman Spectrosc **36**, 497-509 (2005).
81. A. Campion and P. Kambhampati, "Surface-enhanced Raman scattering," Chemical Society Reviews **27**(1998).
82. M. Moskovits, "Persistent misconceptions regarding SERS," Phys Chem Chem Phys **15**, 5301-5311 (2013).
83. M. Fan, G. F. Andrade, and A. G. Brolo, "A review on the fabrication of substrates for surface enhanced Raman spectroscopy and their applications in analytical chemistry," Anal Chim Acta **693**, 7-25 (2011).
84. L. A. Lane, X. Qian, and S. Nie, "SERS Nanoparticles in Medicine: From Label-Free Detection to Spectroscopic Tagging," Chem Rev **115**, 10489-10529 (2015).
85. I. Bruzas, W. Lum, Z. Gorunmez, and L. Sagle, "Advances in surface-enhanced Raman spectroscopy (SERS) substrates for lipid and protein characterization: sensing and beyond," Analyst **143**, 3990-4008 (2018).
86. M. Kahraman, E. R. Mullen, A. Korkmaz, and S. Wachsmann-Hogiu, "Fundamentals and applications of SERS-based bioanalytical sensing," Nanophotonics **6**, 831-852 (2017).

87. A. I. Perez-Jimenez, D. Lyu, Z. X. Lu, G. K. Liu, and R. B. Ren, "Surface-enhanced Raman spectroscopy: benefits, trade-offs and future developments," Chemical Science **11**, 4563-4577 (2020).
88. M. J. Natan, "Surface enhanced Raman scattering," Faraday Discuss **132**, 321-328 (2006).
89. J. Turkevich, P. C. Stevenson, and J. Hillier, "The Formation of Colloidal Gold," The Journal of Physical Chemistry **57**, 670-673 (1953).
90. P. C. Lee and D. Meisel, "Adsorption and surface-enhanced Raman of dyes on silver and gold sols," The Journal of Physical Chemistry **86**, 3391-3395 (1982).
91. L. Liu, Y. Wu, N. Yin, H. Zhang, and H. Ma, "Silver nanocubes with high SERS performance," Journal of Quantitative Spectroscopy and Radiative Transfer **240**(2020).
92. Q. Wang, X. Bai, Y. Zhang, Z. Zhou, M. Guo, J. Zhang, C. Li, C. Wang, and S. Chen, "Layered Assembly of Silver Nanocubes/Polyelectrolyte/Gold Film as an Efficient Substrate for Surface-Enhanced Raman Scattering," ACS Applied Nano Materials **3**, 1934-1941 (2020).
93. F. Tian, F. Bonnier, A. Casey, A. E. Shanahan, and H. J. Byrne, "Surface enhanced Raman scattering with gold nanoparticles: effect of particle shape," Anal. Methods **6**, 9116-9123 (2014).
94. C. Kuttner, M. Mayer, M. Dulle, A. Moscoso, J. M. Lopez-Romero, S. Forster, A. Fery, J. Perez-Juste, and R. Contreras-Caceres, "Seeded Growth Synthesis of Gold Nanotriangles: Size Control, SAXS Analysis, and SERS Performance," ACS Appl Mater Interfaces **10**, 11152-11163 (2018).
95. C. J. Orendorff, A. Gole, T. K. Sau, and C. J. Murphy, "Surface-enhanced Raman spectroscopy of self-assembled monolayers: sandwich architecture and nanoparticle shape dependence," Anal Chem **77**, 3261-3266 (2005).
96. Y. Yokota, K. Ueno, and H. Misawa, "Highly controlled surface-enhanced Raman scattering chips using nanoengineered gold blocks," Small **7**, 252-258 (2011).
97. C. J. Orendorff, L. Gearheart, N. R. Jana, and C. J. Murphy, "Aspect ratio dependence on surface enhanced Raman scattering using silver and gold nanorod substrates," Phys Chem Chem Phys **8**, 165-170 (2006).
98. H. Guo, F. Ruan, L. Lu, J. Hu, J. Pan, Z. Yang, and B. Ren, "Correlating the Shape, Surface Plasmon Resonance, and Surface-Enhanced Raman Scattering of Gold Nanorods," The Journal of Physical Chemistry C **113**, 10459-10464 (2009).
99. C. G. Khoury and T. Vo-Dinh, "Gold Nanostars For Surface-Enhanced Raman Scattering: Synthesis, Characterization and Optimization," The journal of physical chemistry. C, Nanomaterials and interfaces **2008**, 18849-18859 (2008).
100. H. I. Khan, M. U. Khalid, A. Abdullah, A. Ali, A. S. Bhatti, S. U. Khan, and W. Ahmed, "Facile synthesis of gold nanostars over a wide size range and their excellent surface enhanced Raman scattering and fluorescence quenching properties," Journal of Vacuum Science & Technology B, Nanotechnology and Microelectronics: Materials, Processing, Measurement, and Phenomena **36**(2018).
101. C. Song, F. Li, X. Guo, W. Chen, C. Dong, J. Zhang, J. Zhang, and L. Wang, "Gold nanostars for cancer cell-targeted SERS-imaging and NIR light-triggered plasmonic photothermal therapy (PPTT) in the first and second biological windows," J Mater Chem B **7**, 2001-2008 (2019).
102. A. Y. F. Mahmoud, C. J. Rusin, and M. T. McDermott, "Gold nanostars as a colloidal substrate for in-solution SERS measurements using a handheld Raman spectrometer," Analyst **145**, 1396-1407 (2020).

103. J. Xie, Q. Zhang, J. Y. Lee, and D. I. Wang, "The synthesis of SERS-active gold nanoflower tags for in vivo applications," ACS Nano **2**, 2473-2480 (2008).
104. S. Roy, C. Muhammed Ajmal, S. Baik, and J. Kim, "Silver nanoflowers for single-particle SERS with 10 pM sensitivity," Nanotechnology **28**, 465705 (2017).
105. P. N. Njoki, I. I. S. Lim, D. Mott, H.-Y. Park, B. Khan, S. Mishra, R. Sujakumar, J. Luo, and C.-J. Zhong, "Size Correlation of Optical and Spectroscopic Properties for Gold Nanoparticles," The Journal of Physical Chemistry C **111**, 14664-14669 (2007).
106. R. G. Freeman, K. C. Grabar, K. J. Allison, R. M. Bright, J. A. Davis, A. P. Guthrie, M. B. Hommer, M. A. Jackson, P. C. Smith, D. G. Walter, and M. J. Natan, "Self-Assembled Metal Colloid Monolayers: An Approach to SERS Substrates," Science **267**, 1629-1632 (1995).
107. C. D. Keating, M. D. Musick, M. H. Keefe, and M. J. Natan, "Kinetics and Thermodynamics of Au Colloid Monolayer Self-Assembly: Undergraduate Experiments in Surface and Nanomaterials Chemistry," Journal of Chemical Education **76**(1999).
108. J. Y. Jung, Y. W. Kim, and J. Y. Yoo, "Behavior of particles in an evaporating didisperse colloid droplet on a hydrophilic surface," Anal Chem **81**, 8256-8259 (2009).
109. H. Dies, J. Raveendran, C. Escobedo, and A. Docoslis, "In situ assembly of active surface-enhanced Raman scattering substrates via electric field-guided growth of dendritic nanoparticle structures," Nanoscale **9**, 7847-7857 (2017).
110. J. P. Camden, J. A. Dieringer, J. Zhao, and R. P. Van Duyne, "Controlled plasmonic nanostructures for surface-enhanced spectroscopy and sensing," Acc Chem Res **41**, 1653-1661 (2008).
111. K. A. Willets and R. P. Van Duyne, "Localized surface plasmon resonance spectroscopy and sensing," Annu Rev Phys Chem **58**, 267-297 (2007).
112. A. Gopinath, S. V. Boriskina, W. R. Premasiri, L. Ziegler, B. M. Reinhard, and L. Dal Negro, "Plasmonic nanogalaxies: multiscale aperiodic arrays for surface-enhanced Raman sensing," Nano Lett **9**, 3922-3929 (2009).
113. M. A. De Jesus, K. S. Giesfeldt, J. M. Oran, N. A. Abu-Hatab, N. V. Lavrik, and M. J. Sepaniak, "Nanofabrication of densely packed metal-polymer arrays for surface-enhanced Raman spectrometry," Appl Spectrosc **59**, 1501-1508 (2005).
114. Q. Yu, P. Guan, D. Qin, G. Golden, and P. M. Wallace, "Inverted size-dependence of surface-enhanced Raman scattering on gold nanohole and nanodisk arrays," Nano Lett **8**, 1923-1928 (2008).
115. P. Zhang, S. Yang, L. Wang, J. Zhao, Z. Zhu, B. Liu, J. Zhong, and X. Sun, "Large-scale uniform Au nanodisk arrays fabricated via x-ray interference lithography for reproducible and sensitive SERS substrate," Nanotechnology **25**, 245301 (2014).
116. X. Wang, Y. Wu, X. Wen, J. Zhu, X. Bai, Y. Qi, and H. Yang, "Surface plasmons and SERS application of Au nanodisk array and Au thin film composite structure," Optical and Quantum Electronics **52**(2020).
117. K. Li, L. Clime, L. Tay, B. Cui, M. Geissler, and T. Veres, "Multiple surface plasmon resonances and near-infrared field enhancement of gold nanowells," Anal Chem **80**, 4945-4950 (2008).
118. J. Jiang, X. Wang, S. Li, F. Ding, N. Li, S. Meng, R. Li, J. Qi, Q. Liu, and G. L. Liu, "Plasmonic nano-arrays for ultrasensitive bio-sensing," Nanophotonics **7**, 1517-1531 (2018).

119. P. J. Schuck, D. P. Fromm, A. Sundaramurthy, G. S. Kino, and W. E. Moerner, "Improving the mismatch between light and nanoscale objects with gold bowtie nanoantennas," Phys Rev Lett **94**, 017402 (2005).
120. A. Gopinath, S. V. Boriskina, B. M. Reinhard, and L. Dal Negro, "Deterministic aperiodic arrays of metal nanoparticles for surface-enhanced Raman scattering (SERS)," Opt Express **17**, 3741-3753 (2009).
121. M. Kahl, E. Voges, S. Kostrewa, C. Viets, and W. Hill, "Periodically structured metallic substrates for SERS," Sensors and Actuators B: Chemical **51**, 285-291 (1998).
122. M. Altissimo, "E-beam lithography for micro-nanofabrication," Biomicrofluidics **4**(2010).
123. Y. Y. Lin, J. D. Liao, Y. H. Ju, C. W. Chang, and A. L. Shiau, "Focused ion beam-fabricated Au micro/nanostructures used as a surface enhanced Raman scattering-active substrate for trace detection of molecules and influenza virus," Nanotechnology **22**, 185308 (2011).
124. R. M. Langford, P. M. Nellen, J. Gierak, and Y. Fu, "Focused Ion Beam Micro- and Nanoengineering," MRS Bulletin **32**, 417-423 (2011).
125. R. P. Van Duyne, J. C. Hulteen, and D. A. Treichel, "Atomic force microscopy and surface-enhanced Raman spectroscopy. I. Ag island films and Ag film over polymer nanosphere surfaces supported on glass," The Journal of Chemical Physics **99**, 2101-2115 (1993).
126. A. Merlen, V. Gadenne, J. Romann, V. Chevallier, L. Patrone, and J. C. Valmalette, "Surface enhanced Raman spectroscopy of organic molecules deposited on gold sputtered substrates," Nanotechnology **20**, 215705 (2009).
127. K. Leosson, A. S. Ingason, B. Agnarsson, A. Kossoy, S. Olafsson, and M. C. Gather, "Ultra-thin gold films on transparent polymers," Nanophotonics **2**, 3-11 (2013).
128. R. S. Sennett and G. D. Scott, "The Structure of Evaporated Metal Films and Their Optical Properties," Journal of the Optical Society of America **40**(1950).
129. S. M. Novikov, C. Frydendahl, J. Beermann, V. A. Zenin, N. Stenger, V. Coello, N. A. Mortensen, and S. I. Bozhevolnyi, "White Light Generation and Anisotropic Damage in Gold Films near Percolation Threshold," ACS Photonics **4**, 1207-1215 (2017).
130. W. Li, X. Zhao, Z. Yi, A. M. Glushenkov, and L. Kong, "Plasmonic substrates for surface enhanced Raman scattering," Anal Chim Acta **984**, 19-41 (2017).
131. T. Kondo, A. Tomida, N. Morishita, and Y. Saito, "Vapor-deposited Au thin films modified by plasma etching for surface-enhanced Raman scattering active substrates," Journal of Applied Physics **127**(2020).
132. X. Sun and H. Li, "Gold nanoisland arrays by repeated deposition and post-deposition annealing for surface-enhanced Raman spectroscopy," Nanotechnology **24**, 355706 (2013).
133. M. Kang, S. G. Park, and K. H. Jeong, "Repeated Solid-state Dewetting of Thin Gold Films for Nanogap-rich Plasmonic Nanoislands," Sci Rep **5**, 14790 (2015).
134. Y. Bai, L. Yan, J. Wang, L. Su, N. Chen, and Z. Tan, "Highly reproducible and uniform SERS substrates based on Ag nanoparticles with optimized size and gap," Photonics and Nanostructures - Fundamentals and Applications **23**, 58-63 (2017).
135. D. Wang, W. Zhu, M. D. Best, J. P. Camden, and K. B. Crozier, "Wafer-scale metasurface for total power absorption, local field enhancement and single molecule Raman spectroscopy," Sci Rep **3**, 2867 (2013).

136. F. Benz, R. Chikkaraddy, A. Salmon, H. Ohadi, B. de Nijs, J. Mertens, C. Carnegie, R. W. Bowman, and J. J. Baumberg, "SERS of Individual Nanoparticles on a Mirror: Size Does Matter, but so Does Shape," J Phys Chem Lett **7**, 2264-2269 (2016).
137. Z.-M. Jin, W. Gu, X.-B. Shi, Z.-K. Wang, Z.-Q. Jiang, and L.-S. Liao, "A Novel Route to Surface-Enhanced Raman Scattering: Ag Nanoparticles Embedded in the Nanogaps of a Ag Substrate," Adv Opt Mater **2**, 588-596 (2014).
138. M. S. Schmidt, J. Hubner, and A. Boisen, "Large area fabrication of leaning silicon nanopillars for surface enhanced Raman spectroscopy," Adv Mater **24**, OP11-18 (2012).
139. Y. Sharma and A. Dhawan, "Plasmonic "nano-fingers on nanowires" as SERS substrates," Opt Lett **41**, 2085-2088 (2016).
140. P. Joshi and V. Santhanam, "Paper-based SERS active substrates on demand," RSC Adv. **6**, 68545-68552 (2016).
141. Y. Mu and X. Zhang, "A Paper-Fiber-Supported 3D SERS Substrate," Plasmonics **15**, 889-896 (2019).
142. X. S. Zheng, I. J. Jahn, K. Weber, D. Cialla-May, and J. Popp, "Label-free SERS in biological and biomedical applications: Recent progress, current challenges and opportunities," Spectrochim Acta A Mol Biomol Spectrosc **197**, 56-77 (2018).
143. J. Langer, D. Jimenez de Aberasturi, J. Aizpurua, R. A. Alvarez-Puebla, B. Auguie, J. J. Baumberg, G. C. Bazan, S. E. J. Bell, A. Boisen, A. G. Brolo, J. Choo, D. Cialla-May, V. Deckert, L. Fabris, K. Faulds, F. J. Garcia de Abajo, R. Goodacre, D. Graham, A. J. Haes, C. L. Haynes, C. Huck, T. Itoh, M. Kall, J. Kneipp, N. A. Kotov, H. Kuang, E. C. Le Ru, H. K. Lee, J. F. Li, X. Y. Ling, S. A. Maier, T. Mayerhofer, M. Moskovits, K. Murakoshi, J. M. Nam, S. Nie, Y. Ozaki, I. Pastoriza-Santos, J. Perez-Juste, J. Popp, A. Pucci, S. Reich, B. Ren, G. C. Schatz, T. Shegai, S. Schlucker, L. L. Tay, K. G. Thomas, Z. Q. Tian, R. P. Van Duyne, T. Vo-Dinh, Y. Wang, K. A. Willets, C. Xu, H. Xu, Y. Xu, Y. S. Yamamoto, B. Zhao, and L. M. Liz-Marzan, "Present and Future of Surface-Enhanced Raman Scattering," ACS Nano **14**, 28-117 (2020).
144. C. Zong, M. Xu, L. J. Xu, T. Wei, X. Ma, X. S. Zheng, R. Hu, and B. Ren, "Surface-Enhanced Raman Spectroscopy for Bioanalysis: Reliability and Challenges," Chem Rev **118**, 4946-4980 (2018).
145. P. Falagan-Lotsch, E. M. Grzincic, and C. J. Murphy, "One low-dose exposure of gold nanoparticles induces long-term changes in human cells," Proc Natl Acad Sci U S A **113**, 13318-13323 (2016).
146. B. Kang, M. A. Mackey, and M. A. El-Sayed, "Nuclear targeting of gold nanoparticles in cancer cells induces DNA damage, causing cytokinesis arrest and apoptosis," J Am Chem Soc **132**, 1517-1519 (2010).
147. Y.-J. Kim, S. I. Yang, and J.-C. Ryu, "Cytotoxicity and genotoxicity of nano-silver in mammalian cell lines," Molecular & Cellular Toxicology **6**, 119-125 (2010).
148. R. Foldbjerg, D. A. Dang, and H. Autrup, "Cytotoxicity and genotoxicity of silver nanoparticles in the human lung cancer cell line, A549," Arch Toxicol **85**, 743-750 (2011).
149. L. Fabris, "SERS Tags: The Next Promising Tool for Personalized Cancer Detection?," ChemNanoMat **2**, 249-258 (2016).
150. Y. Wang, B. Yan, and L. Chen, "SERS tags: novel optical nanoprobes for bioanalysis," Chem Rev **113**, 1391-1428 (2013).

151. J. Kneipp, H. Kneipp, W. L. Rice, and K. Kneipp, "Optical probes for biological applications based on surface-enhanced Raman scattering from indocyanine green on gold nanoparticles," Anal Chem **77**, 2381-2385 (2005).
152. A. E. Nel, L. Madler, D. Velegol, T. Xia, E. M. Hoek, P. Somasundaran, F. Klaessig, V. Castranova, and M. Thompson, "Understanding biophysicochemical interactions at the nano-bio interface," Nat Mater **8**, 543-557 (2009).
153. T. Cedervall, I. Lynch, S. Lindman, T. Berggard, E. Thulin, H. Nilsson, K. A. Dawson, and S. Linse, "Understanding the nanoparticle-protein corona using methods to quantify exchange rates and affinities of proteins for nanoparticles," Proc Natl Acad Sci U S A **104**, 2050-2055 (2007).
154. G. P. Szekeres and J. Kneipp, "SERS Probing of Proteins in Gold Nanoparticle Agglomerates," Front Chem **7**, 30 (2019).
155. N. Liu, M. Tang, and J. Ding, "The interaction between nanoparticles-protein corona complex and cells and its toxic effect on cells," Chemosphere **245**, 125624 (2020).
156. E. Dumont, C. De Bleye, G. Rademaker, L. Coic, J. Horne, P. Y. Sacre, O. Peulen, P. Hubert, and E. Ziemons, "Development of a prototype device for near real-time surface-enhanced Raman scattering monitoring of biological samples," Talanta **224**, 121866 (2021).
157. D. Cialla, S. Pollok, C. Steinbrücker, K. Weber, and J. Popp, "SERS-based detection of biomolecules," Nanophotonics **3**, 383-411 (2014).
158. D. Cialla-May, X. S. Zheng, K. Weber, and J. Popp, "Recent progress in surface-enhanced Raman spectroscopy for biological and biomedical applications: from cells to clinics," Chem Soc Rev **46**, 3945-3961 (2017).
159. A. I. Pérez-Jiménez, D. Lyu, Z. Lu, G. Liu, and B. Ren, "Surface-enhanced Raman spectroscopy: benefits, trade-offs and future developments," Chemical Science **11**, 4563-4577 (2020).
160. R. La Rocca, G. C. Messina, M. Dipalo, V. Shalabaeva, and F. De Angelis, "Out-of-Plane Plasmonic Antennas for Raman Analysis in Living Cells," Small **11**, 4632-4637 (2015).
161. V. Caprettini, J. A. Huang, F. Moia, A. Jacassi, C. A. Gonano, N. Maccaferri, R. Capozza, M. Dipalo, and F. De Angelis, "Enhanced Raman Investigation of Cell Membrane and Intracellular Compounds by 3D Plasmonic Nanoelectrode Arrays," Adv Sci **5**(2018).
162. J. Kneipp, "Interrogating Cells, Tissues, and Live Animals with New Generations of Surface-Enhanced Raman Scattering Probes and Labels," ACS Nano **11**, 1136-1141 (2017).
163. A. B. Veloso, J. P. F. Longo, L. A. Muehlmann, B. F. Tollstadius, P. E. N. Souza, R. B. Azevedo, P. C. Morais, and S. W. da Silva, "SERS Investigation of Cancer Cells Treated with PDT: Quantification of Cell Survival and Follow-up," Sci Rep **7**, 7175 (2017).
164. G. F. Stiufiuc, V. Toma, M. Buse, R. Marginean, G. Morar-Bolba, B. Culic, R. Tetean, N. Leopold, I. Pavel, C. M. Lucaciu, and R. I. Stiufiuc, "Solid Plasmonic Substrates for Breast Cancer Detection by Means of SERS Analysis of Blood Plasma," Nanomaterials (Basel) **10**(2020).
165. E. Gurian, A. Di Silvestre, E. Mitri, D. Pascut, C. Tiribelli, M. Giuffre, L. S. Croce, V. Sergo, and A. Bonifacio, "Repeated double cross-validation applied to the PCA-LDA classification of SERS spectra: a case study with serum samples from hepatocellular carcinoma patients," Anal Bioanal Chem **413**, 1303-1312 (2021).

166. S. Seifert, "Application of random forest based approaches to surface-enhanced Raman scattering data," Sci Rep **10**, 5436 (2020).
167. X. Cao, Y. Shan, L. Tan, X. Yu, M. Bao, W. Li, and H. Shi, "Hollow Au nanoflower substrates for identification and discrimination of the differentiation of bone marrow mesenchymal stem cells by surface-enhanced Raman spectroscopy," Journal of Materials Chemistry B **5**, 5983-5995 (2017).
168. D. Sun, W. Xu, C. Liang, W. Shi, and S. Xu, "Smart Surface-Enhanced Resonance Raman Scattering Nanoprobe for Monitoring Cellular Alkaline Phosphatase Activity during Osteogenic Differentiation," ACS Sens **5**, 1758-1767 (2020).
169. X. Cao, Z. Wang, L. Bi, C. Bi, and Q. Du, "Gold nanocage-based surface-enhanced Raman scattering probes for long-term monitoring of intracellular microRNA during bone marrow stem cell differentiation," Nanoscale **12**, 1513-1527 (2020).
170. G. S. Mandair and M. D. Morris, "Contributions of Raman spectroscopy to the understanding of bone strength," Bonekey Rep **4**, 620 (2015).
171. M. Khalid, T. Bora, A. A. Ghaithi, S. Thukral, and J. Dutta, "Raman Spectroscopy detects changes in Bone Mineral Quality and Collagen Cross-linkage in Staphylococcus Infected Human Bone," Sci Rep **8**, 9417 (2018).
172. A. Sharma, A. Goring, K. A. Staines, R. J. H. Emery, A. A. Pitsillides, R. O. C. Oreffo, S. Mahajan, and C. E. Clarkin, "Raman spectroscopy links differentiating osteoblast matrix signatures to pro-angiogenic potential," Matrix Biology Plus **5**(2020).
173. A. J. Friedenstein, K. V. Petrakova, A. I. Kurolesova, and G. P. Frolova, "Heterotopic of bone marrow. Analysis of precursor cells for osteogenic and hematopoietic tissues," Transplantation **6**, 230-247 (1968).
174. A. J. Friedenstein, U. F. Deriglasova, N. N. Kulagina, A. F. Panasuk, S. F. Rudakowa, E. A. Luria, and I. A. Rudakow, "Precursors for Fibroblasts in Different Populations of Hematopoietic Cells as Detected by Invitro Colony Assay Method," Experimental Hematology **2**, 83-92 (1974).
175. M. Owen and A. J. Friedenstein, "Stromal stem cells: marrow-derived osteogenic precursors," Ciba Found Symp **136**, 42-60 (1988).
176. A. I. Caplan, "Mesenchymal stem cells," J Orthop Res **9**, 641-650 (1991).
177. A. G. Via, A. Frizziero, and F. Oliva, "Biological properties of mesenchymal Stem Cells from different sources," Muscles Ligaments Tendons J **2**, 154-162 (2012).
178. A. Keating, "Mesenchymal stromal cells," Curr Opin Hematol **13**, 419-425 (2006).
179. P. Bianco, P. G. Robey, and P. J. Simmons, "Mesenchymal stem cells: revisiting history, concepts, and assays," Cell Stem Cell **2**, 313-319 (2008).
180. E. M. Horwitz, M. Andreef, and F. Frassoni, "Mesenchymal Stromal Cells," Biology of Blood and Marrow Transplantation **13**, 53-57 (2007).
181. P. Bianco, "Stem cells and bone: a historical perspective," Bone **70**, 2-9 (2015).
182. J. K. Biehl and B. Russell, "Introduction to stem cell therapy," J Cardiovasc Nurs **24**, 98-103; quiz 104-105 (2009).
183. M. Dominici, K. Le Blanc, I. Mueller, I. Slaper-Cortenbach, F. Marini, D. Krause, R. Deans, A. Keating, D. Prockop, and E. Horwitz, "Minimal criteria for defining multipotent mesenchymal stromal cells. The International Society for Cellular Therapy position statement," Cytotherapy **8**, 315-317 (2006).
184. A. I. Caplan, "Mesenchymal Stem Cells: Time to Change the Name!," Stem Cells Transl Med **6**, 1445-1451 (2017).

185. R. Berebichez-Fridman and P. R. Montero-Olvera, "Sources and Clinical Applications of Mesenchymal Stem Cells: State-of-the-art review," Sultan Qaboos Univ Med J **18**, e264-e277 (2018).
186. M. Pevsner-Fischer, S. Levin, and D. Zipori, "The origins of mesenchymal stromal cell heterogeneity," Stem Cell Rev Rep **7**, 560-568 (2011).
187. M. Strioga, S. Viswanathan, A. Darinskas, O. Slaby, and J. Michalek, "Same or not the same? Comparison of adipose tissue-derived versus bone marrow-derived mesenchymal stem and stromal cells," Stem Cells Dev **21**, 2724-2752 (2012).
188. H. S. Goodwin, A. R. Bicknese, S. N. Chien, B. D. Bogucki, C. O. Quinn, and D. A. Wall, "Multilineage differentiation activity by cells isolated from umbilical cord blood: expression of bone, fat, and neural markers," Biol Blood Marrow Transplant **7**, 581-588 (2001).
189. P. Mattar and K. Bieback, "Comparing the Immunomodulatory Properties of Bone Marrow, Adipose Tissue, and Birth-Associated Tissue Mesenchymal Stromal Cells," Front Immunol **6**, 560 (2015).
190. S. Kern, H. Eichler, J. Stoeve, H. Kluter, and K. Bieback, "Comparative analysis of mesenchymal stem cells from bone marrow, umbilical cord blood, or adipose tissue," Stem Cells **24**, 1294-1301 (2006).
191. D. G. Phinney, G. Kopen, W. Righter, S. Webster, N. Tremain, and D. J. Prockop, "Donor variation in the growth properties and osteogenic potential of human marrow stromal cells," Journal of Cellular Biochemistry **75**, 424-436 (1999).
192. T. Assis-Ribas, M. F. Forni, S. M. B. Winnischofer, M. C. Sogayar, and M. Trombetta-Lima, "Extracellular matrix dynamics during mesenchymal stem cells differentiation," Dev Biol **437**, 63-74 (2018).
193. F. Gattazzo, A. Urciuolo, and P. Bonaldo, "Extracellular matrix: a dynamic microenvironment for stem cell niche," Biochim Biophys Acta **1840**, 2506-2519 (2014).
194. T. Yin and L. Li, "The stem cell niches in bone," J Clin Invest **116**, 1195-1201 (2006).
195. J. L. Liesveld, N. Sharma, and O. S. Aljitawi, "Stem cell homing: From physiology to therapeutics," Stem Cells **38**, 1241-1253 (2020).
196. A. A. Khalili and M. R. Ahmad, "A Review of Cell Adhesion Studies for Biomedical and Biological Applications," Int J Mol Sci **16**, 18149-18184 (2015).
197. E. Novoseletskaya, O. Grigorieva, P. Nimiritsky, N. Basalova, R. Eremichev, I. Milovskaya, K. Kulebyakin, M. Kulebyakina, S. Rodionov, N. Omelyanenko, and A. Efimenko, "Mesenchymal Stromal Cell-Produced Components of Extracellular Matrix Potentiate Multipotent Stem Cell Response to Differentiation Stimuli," Front Cell Dev Biol **8**, 555378 (2020).
198. J. D. Humphrey, E. R. Dufresne, and M. A. Schwartz, "Mechanotransduction and extracellular matrix homeostasis," Nat Rev Mol Cell Biol **15**, 802-812 (2014).
199. M. N. Knight and K. D. Hankenson, "Mesenchymal Stem Cells in Bone Regeneration," Adv Wound Care (New Rochelle) **2**, 306-316 (2013).
200. A. Rutkovskiy, K. O. Stenslokken, and I. J. Vaage, "Osteoblast Differentiation at a Glance," Med Sci Monit Basic Res **22**, 95-106 (2016).
201. E. Birmingham, G. L. Niebur, P. E. McHugh, G. Shaw, F. P. Barry, and L. M. McNamara, "Osteogenic differentiation of mesenchymal stem cells is regulated by osteocyte and osteoblast cells in a simplified bone niche," Eur Cell Mater **23**, 13-27 (2012).

202. S. L. Cheng, J. W. Yang, L. Rifas, S. F. Zhang, and L. V. Avioli, "Differentiation of human bone marrow osteogenic stromal cells in vitro: induction of the osteoblast phenotype by dexamethasone," Endocrinology **134**, 277-286 (1994).
203. S.-L. Cheng, S.-F. Zhang, and L. V. Avioli, "Expression of bone matrix proteins during dexamethasone-induced mineralization of human bone marrow stromal cells," Journal of Cellular Biochemistry **61**, 182-193 (1996).
204. S. Takamizawa, Y. Maehata, K. Imai, H. Senoo, S. Sato, and R. Hata, "Effects of ascorbic acid and ascorbic acid 2-phosphate, a long-acting vitamin C derivative, on the proliferation and differentiation of human osteoblast-like cells," Cell Biol Int **28**, 255-265 (2004).
205. S. Scarfi, "Use of bone morphogenetic proteins in mesenchymal stem cell stimulation of cartilage and bone repair," World J Stem Cells **8**, 1-12 (2016).
206. J. Caetano-Lopes, H. Canhao, and J. E. Fonseca, "Osteoblasts and bone formation," Acta Reumatologica Portuguesa **32**, 103-110 (2007).
207. J. Frith and P. Genever, "Transcriptional control of mesenchymal stem cell differentiation," Transfus Med Hemother **35**, 216-227 (2008).
208. C. Graneli, A. Thorfve, U. Ruetschi, H. Brisby, P. Thomsen, A. Lindahl, and C. Karlsson, "Novel markers of osteogenic and adipogenic differentiation of human bone marrow stromal cells identified using a quantitative proteomics approach," Stem Cell Res **12**, 153-165 (2014).
209. W. Ostwald, "Studien über die Bildung und Umwandlung fester Körper," Zeitschrift für Physikalische Chemie **22U**(1897).
210. P. Sahu and B. L. Prasad, "Time and temperature effects on the digestive ripening of gold nanoparticles: is there a crossover from digestive ripening to Ostwald ripening?," Langmuir **30**, 10143-10150 (2014).
211. A. Milewska, V. Zivanovic, V. Merk, U. B. Arnalds, O. E. Sigurjonsson, J. Kneipp, and K. Leosson, "Gold nanoisland substrates for SERS characterization of cultured cells," Biomed Opt Express **10**, 6172-6188 (2019).
212. E. Palik, "Handbook of Optical Constants of Solids," Academic Press **1**(1985).
213. A. Kudelski, "Raman studies of rhodamine 6G and crystal violet sub-monolayers on electrochemically roughened silver substrates: Do dye molecules adsorb preferentially on highly SERS-active sites?," Chem Phys Lett **414**, 271-275 (2005).
214. M. Moskovits and B. Vlckova, "Adsorbate-induced silver nanoparticle aggregation kinetics," J Phys Chem B **109**, 14755-14758 (2005).
215. R. L. Olmon, B. Slovick, T. W. Johnson, D. Shelton, S.-H. Oh, G. D. Boreman, and M. B. Raschke, "Optical dielectric function of gold," Physical Review B **86**(2012).
216. A. Milewska, A. S. Ingason, O. E. Sigurjonsson, and K. Leosson, "Herding cats: managing gold atoms on common transparent dielectrics [Invited]," Optical Materials Express **9**, pp. 112-119 (2019) (2018).
217. J. Quan, J. Zhang, X. Qi, J. Li, N. Wang, and Y. Zhu, "A study on the correlation between the dewetting temperature of Ag film and SERS intensity," Sci Rep **7**, 14771 (2017).
218. S. Postaci, B. C. Yildiz, A. Bek, and M. E. Tasgin, "Silent enhancement of SERS signal without increasing hot spot intensities," Nanophotonics **7**, 1687-1695 (2018).
219. V. Joseph, A. Matschulat, J. Polte, S. Rolf, F. Emmerling, and J. Kneipp, "SERS enhancement of gold nanospheres of defined size," J Raman Spectrosc **42**, 1736-1742 (2011).
220. E. C. Le Ru and P. G. Etchegoin, "Quantifying SERS enhancements," MRS Bulletin **38**, 631-640 (2013).

221. G. J. Kovacs, R. O. Loutfy, P. S. Vincett, C. Jennings, and R. Aroca, "Distance dependence of SERS enhancement factor from Langmuir-Blodgett monolayers on metal island films: evidence for the electromagnetic mechanism," Langmuir **2**, 689-694 (2002).
222. A. Milewska, O. E. Sigurjonsson, and K. Leosson, "SERS Imaging of Mesenchymal Stromal Cell Differentiation," Acs Applied Bio Materials **4**, 4999-5007 (2021).
223. Z. Movasaghi, S. Rehman, and I. U. Rehman, "Raman Spectroscopy of Biological Tissues," Applied Spectroscopy Reviews **42**, 493-541 (2007).
224. A. C. S. Talari, Z. Movasaghi, S. Rehman, and I. u. Rehman, "Raman Spectroscopy of Biological Tissues," Applied Spectroscopy Reviews **50**, 46-111 (2014).
225. H. B. Lodish, A; Zipursky, S. L.; Matsudaira, P.; Baltimore, D.; Darnell, J., "Molecular Cell Biology, 4th edition," National Center for Biotechnology Information (US) (2000).
226. K. Simons, "Cell membranes: A subjective perspective," Biochim Biophys Acta **1858**, 2569-2572 (2016).
227. F. Draux, C. Gobinet, J. Sule-Suso, A. Trussardi, M. Manfait, P. Jeannesson, and G. D. Sockalingum, "Raman spectral imaging of single cancer cells: probing the impact of sample fixation methods," Anal Bioanal Chem **397**, 2727-2737 (2010).
228. A. D. Meade, C. Clarke, F. Draux, G. D. Sockalingum, M. Manfait, F. M. Lyng, and H. J. Byrne, "Studies of chemical fixation effects in human cell lines using Raman microspectroscopy," Anal Bioanal Chem **396**, 1781-1791 (2010).
229. A. Rygula, K. Majzner, K. M. Marzec, A. Kaczor, M. Pilarczyk, and M. Baranska, "Raman spectroscopy of proteins: a review," J Raman Spectrosc **44**, 1061-1076 (2013).
230. L. Mikoliunaite, R. D. Rodriguez, E. Sheremet, V. Kolchuzhin, J. Mehner, A. Ramanavicius, and D. R. Zahn, "The substrate matters in the Raman spectroscopy analysis of cells," Sci Rep **5**, 13150 (2015).
231. J. Kneipp, H. Kneipp, B. Wittig, and K. Kneipp, "Novel optical nanosensors for probing and imaging live cells," Nanomedicine **6**, 214-226 (2010).
232. B. Kann, H. L. Offerhaus, M. Windbergs, and C. Otto, "Raman microscopy for cellular investigations - From single cell imaging to drug carrier uptake visualization," Adv Drug Deliver Rev **89**, 71-90 (2015).
233. K. Czamara, K. Majzner, M. Z. Pacia, K. Kochan, A. Kaczor, and M. Baranska, "Raman spectroscopy of lipids: a review," J Raman Spectrosc **46**, 4-20 (2015).
234. V. Zivanovic, G. Semini, M. Laue, D. Drescher, T. Aebischer, and J. Kneipp, "Chemical Mapping of Leishmania Infection in Live Cells by SERS Microscopy," Anal Chem **90**, 8154-8161 (2018).
235. D. Borchman, D. Tang, and M. C. Yappert, "Lipid composition, membrane structure relationships in lens and muscle sarcoplasmic reticulum membranes," Biospectroscopy **5**, 151-167 (1999).
236. C. Krafft, L. Neudert, T. Simat, and R. Salzer, "Near infrared Raman spectra of human brain lipids," Spectrochim Acta A Mol Biomol Spectrosc **61**, 1529-1535 (2005).
237. C. Lee, R. P. Carney, S. Hazari, Z. J. Smith, A. Knudson, C. S. Robertson, K. S. Lam, and S. Wachsmann-Hogiu, "3D plasmonic nanobowl platform for the study of exosomes in solution," Nanoscale **7**, 9290-9297 (2015).
238. E. Sezgin, I. Levental, S. Mayor, and C. Eggeling, "The mystery of membrane organization: composition, regulation and roles of lipid rafts," Nat Rev Mol Cell Biol **18**, 361-374 (2017).

239. F. Wei, D. Zhang, N. J. Halas, and J. D. Hartgerink, "Aromatic amino acids providing characteristic motifs in the Raman and SERS spectroscopy of peptides," J Phys Chem B **112**, 9158-9164 (2008).
240. N. Ruiz, S. S. Chng, A. Hiniker, D. Kahne, and T. J. Silhavy, "Nonconsecutive disulfide bond formation in an essential integral outer membrane protein," Proc Natl Acad Sci U S A **107**, 12245-12250 (2010).
241. A. J. de Jesus and T. W. Allen, "The role of tryptophan side chains in membrane protein anchoring and hydrophobic mismatch," Biochim Biophys Acta **1828**, 864-876 (2013).
242. R. P. Berger, M. Dookwah, R. Steet, and S. Dalton, "Glycosylation and stem cells: Regulatory roles and application of iPSCs in the study of glycosylation-related disorders," Bioessays **38**, 1255-1265 (2016).
243. G. S. Mandair, P. Steenhuis, M. A. Ignelzi, and M. D. Morris, "Bone quality assessment of osteogenic cell cultures by Raman microscopy," J Raman Spectrosc **50**, 360-370 (2018).
244. H. Wu, J. V. Volponi, A. E. Oliver, A. N. Parikh, B. A. Simmons, and S. Singh, "In vivo lipidomics using single-cell Raman spectroscopy," Proc Natl Acad Sci U S A **108**, 3809-3814 (2011).
245. P. J. Marie and O. Fromigue, "Osteogenic differentiation of human marrow-derived mesenchymal stem cells," Regen Med **1**, 539-548 (2006).
246. R. E. Wuthier, "Effect of phospholipids on the transformation of amorphous calcium phosphate to hydroxapatite in vitro," Calcif Tissue Res **19**, 197-210 (1975).
247. C. L. Raggio, B. D. Boyan, and A. L. Boskey, "In vivo hydroxyapatite formation induced by lipids," J Bone Miner Res **1**, 409-415 (1986).
248. A. L. Boskey, W. Ullrich, L. Spevak, and H. Gilder, "Persistence of complexed acidic phospholipids in rapidly mineralizing tissues is due to affinity for mineral and resistance to hydrolytic attack: in vitro data," Calcif Tissue Int **58**, 45-51 (1996).
249. E. J. Fernandez-Perez, F. J. Sepulveda, C. Peters, D. Bascunan, N. O. Riffo-Lepe, J. Gonzalez-Sanmiguel, S. A. Sanchez, R. W. Peoples, B. Vicente, and L. G. Aguayo, "Effect of Cholesterol on Membrane Fluidity and Association of Abeta Oligomers and Subsequent Neuronal Damage: A Double-Edged Sword," Front Aging Neurosci **10**, 226 (2018).
250. C. Bonnans, J. Chou, and Z. Werb, "Remodelling the extracellular matrix in development and disease," Nat Rev Mol Cell Biol **15**, 786-801 (2014).
251. K. Sonomoto, K. Yamaoka, H. Kaneko, K. Yamagata, K. Sakata, X. Zhang, M. Kondo, Y. Zenke, K. Sabanai, S. Nakayamada, A. Sakai, and Y. Tanaka, "Spontaneous Differentiation of Human Mesenchymal Stem Cells on Poly-Lactic-Co-Glycolic Acid Nano-Fiber Scaffold," PLoS One **11**, e0153231 (2016).
252. C. De Bleye, M. Fontaine, E. Dumont, P. Y. Sacre, P. Hubert, N. Theys, and E. Ziemons, "Raman imaging as a new analytical tool for the quality control of the monitoring of osteogenic differentiation in forming 3D bone tissue," J Pharm Biomed Anal **186**, 113319 (2020).
253. V. Zivanovic, S. Seifert, D. Drescher, P. Schrade, S. Werner, P. Guttmann, G. P. Szekeres, S. Bachmann, G. Schneider, C. Arenz, and J. Kneipp, "Optical Nanosensing of Lipid Accumulation due to Enzyme Inhibition in Live Cells," ACS Nano **13**, 9363-9375 (2019).
254. A. Ruhle, A. Thomsen, R. Saffrich, M. Voglstatter, B. Bieber, T. Sprave, P. Wuchter, P. Vaupel, P. E. Huber, A. L. Grosu, and N. H. Nicolay, "Multipotent mesenchymal

stromal cells are sensitive to thermic stress - potential implications for therapeutic hyperthermia," Int J Hyperthermia **37**, 430-441 (2020).
255. M. F. Chen, C. T. Lin, W. C. Chen, C. T. Yang, C. C. Chen, S. K. Liao, J. M. Liu, C. H. Lu, and K. D. Lee, "The sensitivity of human mesenchymal stem cells to ionizing radiation," Int J Radiat Oncol Biol Phys **66**, 244-253 (2006).
256. J. Kim, S. H. Nam, D. K. Lim, and Y. D. Suh, "SERS-based particle tracking and molecular imaging in live cells: toward the monitoring of intracellular dynamics," Nanoscale **11**, 21724-21727 (2019).
257. S. Sloan-Dennison, M. R. Bevins, B. T. Scarpitti, V. K. Sauve, and Z. D. Schultz, "Protein corona-resistant SERS tags for live cell detection of integrin receptors," Analyst **144**, 5538-5546 (2019).
258. Y. Zhang, D. Jimenez de Aberasturi, M. Henriksen-Lacey, J. Langer, and L. M. Liz-Marzan, "Live-Cell Surface-Enhanced Raman Spectroscopy Imaging of Intracellular pH: From Two Dimensions to Three Dimensions," ACS Sens **5**, 3194-3206 (2020).
259. R. Manoharan, J. J. Baraga, M. S. Feld, and R. P. Rava, "Quantitative histochemical analysis of human artery using Raman spectroscopy," Journal of Photochemistry and Photobiology B: Biology **16**, 211-233 (1992).
260. V. Živanović, A. Milewska, K. Leosson, and J. Kneipp, "Molecular Structure and Interactions of Lipids in the Outer Membrane of Living Cells Based on Surface-Enhanced Raman Scattering and Liposome Models," Analytical Chemistry **93**, 10106-10113 (2021).